DARK ASPECTS OF COSMOLOGY

A Dissertation

Presented to the Faculty of the Graduate School

of Cornell University

in Partial Fulfillment of the Requirements for the Degree of

Doctor of Philosophy

by

Naresh Kumar

August 2012

DARK ASPECTS OF COSMOLOGY

Naresh Kumar, Ph.D.

Cornell University 2012

This thesis investigates aspects of dark matter and dark energy and constraints that can be imposed on them from current and future observations. Specifically, we first study the idea that the observed acceleration of the Universe could be due to the gravitational backreaction of perturbations on super-horizon scales. We show that this does not work for the case of a cosmological model containing baryonic matter, cold dark matter and a scalar field. Next, assuming the presence of dark energy and dark matter, we study the gravitational lensing effects of large scale structures on luminosity distances of sources. Standard candle sources such as supernovae have been used to measure the dark energy content of the Universe, and gravitational lensing is a source of systematic error in these measurements. We investigate the effects of large scale structures like voids and smaller halos using Monte Carlo simulations.

BIOGRAPHICAL SKETCH

Originally from a small town in Southern India called Tirupur, I have lived in Ahmedabad in Gujarat state in India; I spent all my schooling years at the wonderfully aptly named institution, The Indian School, in the Kingdom of Bahrain; I pursued my undergraduate education in Mathematics and Physics at Columbia University in New York City before I moved to Ithaca as a graduate student in Physics at Cornell University.

I'd like to think that my interests lie far and wide and I have always believed that one's goal in life is to pursue as many of these as possible. A small selection of my most beloved interests include cricket, association football, racquet sports, the works of P. G. Wodehouse, R. K. Narayan and traveling. I spent a major portion of my childhood watching the BBC which has been instrumental in shaping me in nearly all aspects of my life.

To my family and friends.

ACKNOWLEDGEMENTS

I would like to first and foremost thank my supervisor, Eanna Flanagan, for his encouragement and guidance has made this thesis possible. I would also like to thank my collaborators Ira Wasserman and R. Ali Vanderveld for their help and insight which has enabled me to become a better scientist.

Next, I would like to thank my numerous friends and officemates who have shared this ride along with me and made my time at Cornell thoroughly fun and inspiring. Finally, I would like to thank the Graduate School and all the staff at the Physics department for their help and for being always patient and wonderful in accomodating all my requirements.

This research was supported at Cornell by NSF grants PHY-0757735, PHY-0555216, PHY-0968820, PHY-0968820 and PHY-1068541 and by NASA grants NNX 08AH27G andNNX11AI95G, and from the Kavli Institute for Cosmological Physics at the University of Chicago through grants NSF PHY-0114422 and NSF PHY-0551142 and an endowment from the Kavli Foundation and its founder Fred Kavli.

TABLE OF CONTENTS

LIST OF TABLES

LIST OF FIGURES

CHAPTER 1

INTRODUCTION

The last two decades have been an exciting time for cosmology. Experiments have been successful in revealing the various constituents of the Universe and their distribution in space. We have also made great advances in collecting data that has helped us study the evolution of galaxies and large scale structures and are also tantalizingly close to proving the existence of black holes.

The two discoveries relevant to this work are the confirmation of the existence of a new type of matter called dark matter and the discovery of a new antigravitating effect called dark energy.

1.1 Evidence for Dark Matter

Most of the visible universe that we know and love is made of something called baryonic matter. All the elements, all the chemical compounds we find on the earth, everything we make with them, stars, planets, moons etc. are made of baryonic matter. Dark matter, however, is postulated to be 10 times more prevalent than baryonic matter. Unfortunately, dark matter has been fairly elusive because, as far as we know through experiments and everyday experience, this matter interacts only weakly with baryonic matter. It does not interact electromagnetically in any way that we have been able to detect. The only way we can detect the presence of dark matter is through its gravitational interaction. Like ordinary baryonic matter, dark matter has mass and so we can detect the presence of dark matter in galaxies and galaxy clusters by studying the motion of objects in its gravitational field.

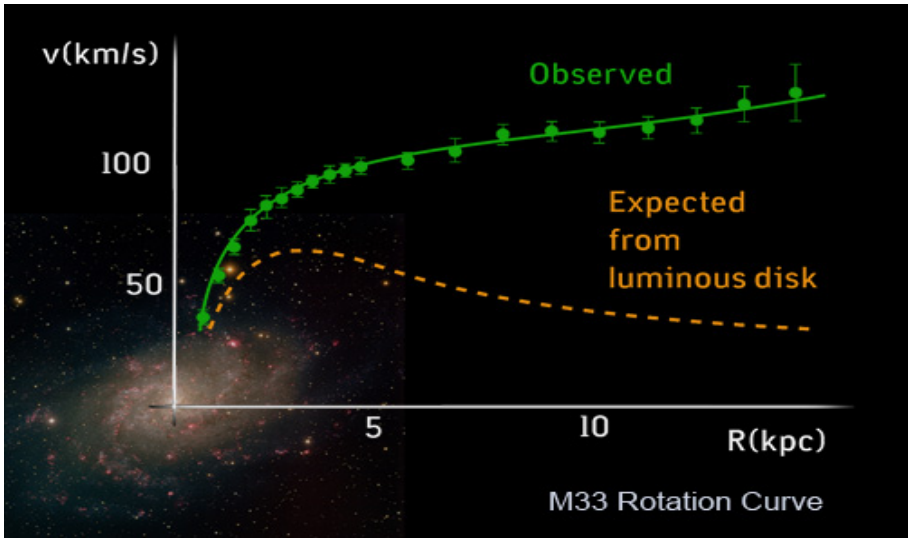

Figure 1.1: An example of galactic rotation curve for M33 Galaxy deviating severely from the Keplerian prediction [1].

Even though a direct detection has not been made in the lab, the existence of this new type of matter is thought to be necessary to explain astrophysical observations. The first such observation is the relationship between the distance of stars from the centers of galaxies and the velocities with which they move around these centers. For millennia, we have studied and counted the number of stars in the sky. However, in the last 100 years or so, we have discovered

many other objects in addition to stars. We have observed galaxies formed of billions of stars and we have discovered dozens of galaxies held gravitationally in clusters. Since we roughly know the amount and distribution of baryonic matter in galaxies in the form of gas and stars, we can derive the Keplerian velocities of stars. The resulting predicted velocities are smaller than those observed. In fact, it was observed that galactic rotation curves (plots of the velocity of stars versus the distance from the center of the galaxy) flatten out and become constant at distances much greater than the the baryonic radius of galaxies [1]. We know the baryonic radius of galaxies from direct optical and radio observations.

Figure 1.1 shows as an example the observed and predicted rotation curves for the galaxy M33. One explanation for the significantly different velocities is the presence of a spherical distribution of dark matter (called a halo) which is much bigger than the galaxy but which surrounds the galaxy with a roughly uniform distribution. The dark matter halo affects the graviational potential of the system and hence the velocities of stars in the outer regions of the galaxy.

Another technique that has been used to infer the presence of dark matter is gravitational lensing - the distortion of images of galaxies and galaxy clusters due to light bending by matter along the line of sight. When light rays from background galaxies pass close to a foreground galaxy cluster, they bend and shear in a manner determined by the distribution of mass in the cluster. By examining the deformation of background galaxy images, one can infer the distribution of the total mass density (dark plus baryonic), which is dominated by dark matter. An example of lensing by a galaxy is shown in Figure 1.2 [7]. The dark matter density inferred from lensing observations agrees well with the

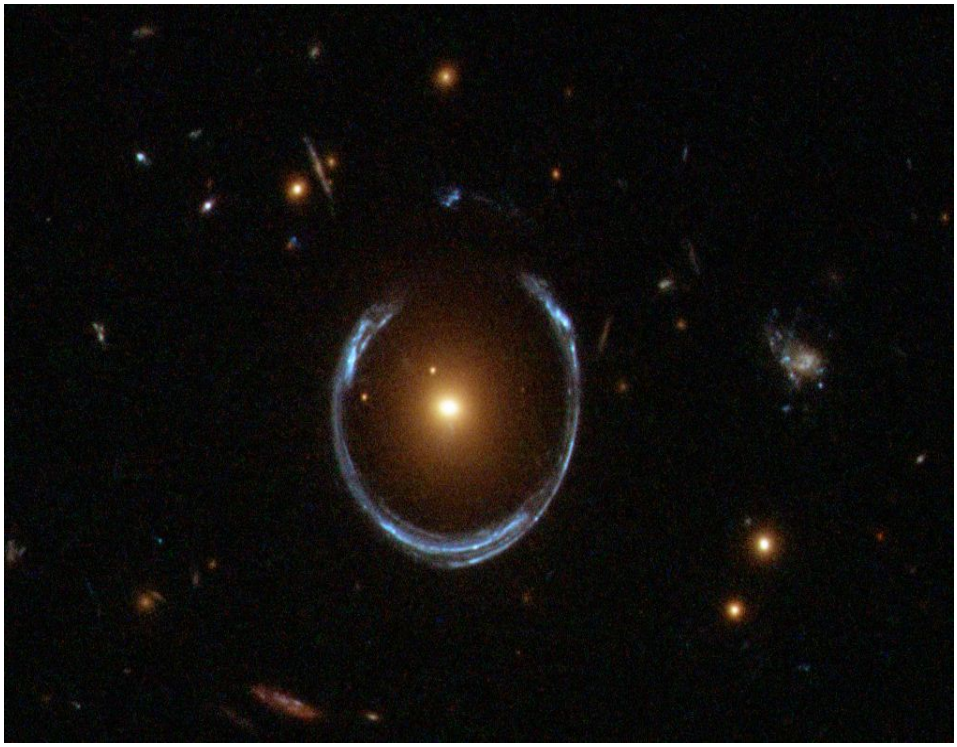

Figure 1.2: LRG 3-757, the luminous galaxy in the foreground distorts the image of a blue galaxy that lies behind it [7].

density inferred from X-ray observation of galaxies clusters that probe the depth of the gravitational potential.

Striking evidence for dark matter comes from the Bullet Cluster (Figure 1.3), which is a system where a collision of two galaxy clusters, at redshift 0.3, has left behind a distinct baryonic part which is detected by X-ray emissions and a dark matter component which was detected by its gravitational lensing effects on background galaxies [2].

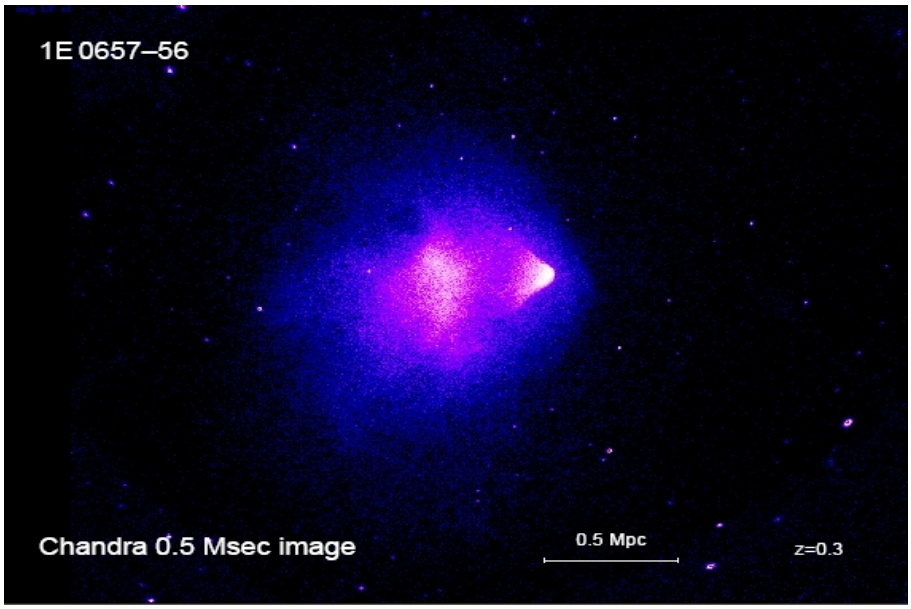

Figure 1.3: The Bullet Cluster, X-ray photo by Chandra X-ray Observatory [2].

Finally, a third observation indicating the necessity of dark matter is the anisotropy of the Cosmic Microwave Background (CMB). CMB experiments measure small fluctuations in the CMB temperature in different directions (Figure 1.4). The spectrum of these fluctuations can be calculated, assuming a Universe consisting of baryonic matter, dark matter and radiation. It is found that the dark matter is necessary for the predicted spectrum to be consistent with the

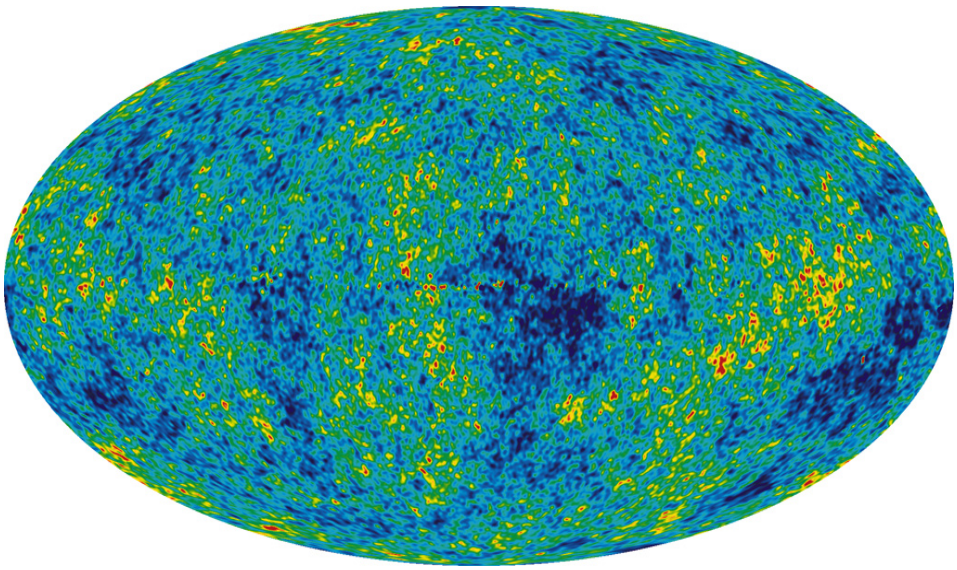

Figure 1.4: Temperature anisotropies in WMAP's 5-year data. These fluctuations, shown as color differences, are produced by the primordial density perturbations that grew to become galaxies and other large scale structures. The temperature range here is 200 microKelvin [3].

CMB observations. Figure 1.5 shows the angular spectrum of the fluctuations measured by the Wilkinson Microwave Anisotropy Probe (WMAP) [4]. It is a measure of the relative brightness of the spots in Figure 1.4 versus the angular size of the spots. Combining information from the first three peaks gives us information about the dark matter density [8].

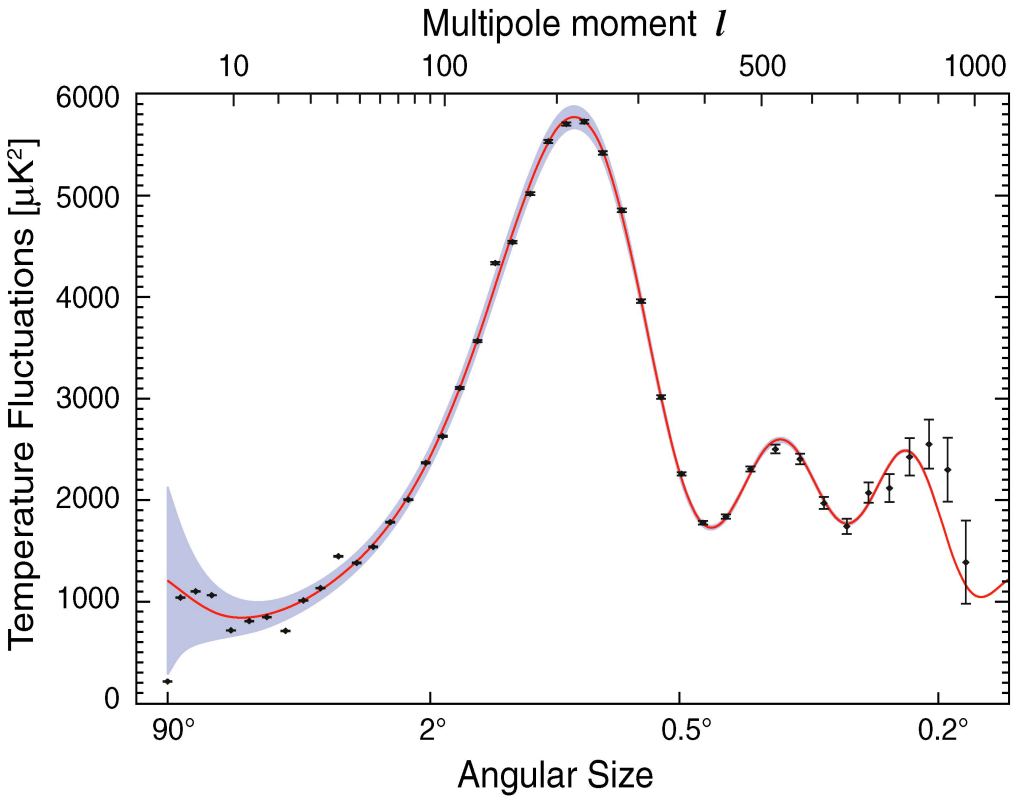

Figure 1.5: The angular power spectrum of CMB fluctuations measured by WMAP, which measures the relative brightness of spots in the map versus the angular size of the spots [4].

1.2 Dark Energy

Ever since Hubble observed that the Universe is expanding and that objects farther away from us move ever faster away from us, a lot of effort has been devoted to accurately measuring the expansion rate. The development of more and more sophisticated ways to measure the rate of expansion led to a major discovery in the late 1990s. This was the observation that the expansion of the

Universe is accelerating. After this discovery, a major debate about the explanation of this phenomenon broke out.

A simple explanation for this is achieved by inserting a cosmological constant in Einsteins field equation. However, there is no natural way for this to arise in our theories and it has to be fine tuned to fit the observed acceleration. The simplest models offering a solution to the fine tuning problem are quintessence models [20], where a scalar field dynamically generates dark energy effects. Cosmic acceleration can also in principle be explained by modifying general relativity at large distance scales. However, the naturalness problem persists in most of these dynamical models.

It has also been suggested that the acceleration of the Universe can be explained by a purely general relativistic effect involving no new physics, the backreaction of perturbations [34, 35, 36, 37, 38]. By taking a spatial average of Einsteins equations in a particular gauge, one can obtain an effective spatially averaged scale factor with extra driving terms coming from backreaction. These extra driving terms can in principle drive an acceleration. Although the conventional viewpoint is that the effect of backreaction is small, some have argued that it can be large enough to account for cosmic acceleration.

There are two variants of the backreaction explanation. The first is that cosmic acceleration is caused by the backreaction of primodial large scale (superhorizon) gravitational perturbations. In particular Kolb et al [34, 35] looked at primordial perturbations and claimed that at second order one could obtain a negative deceleration parameter. This claim was disproved in Refs. [49, 50, 51]. The second variant of the backreaction explanation is that the backreaction of primordial small scale (subhorizon) gravitational perturbations can explain cos-

mic acceleration. This has been ruled out by [9] and [10].

For a Universe dominated by cold dark matter (CDM), it is known that the backreaction of superhorizon perturbations cannot drive acceleration [41]. In Chapter 2 of this work, we extend this result to models with cold dark matter together with another entity called a scalar field that could act as the generator for this acceleration. We develop a method to compute the acceleration from this model and show that the computed acceleration is very much smaller than required to explain observations.

More specifically, we focus on the backreaction of superhorizon perturbations in the present day Universe. We show that for a Universe with cold dark matter and a scalar field (as in standard quintessence models), achieving the required value of the deceleration parameter requires a non-zero potential. We compute luminosity distance as a function of redshift using Taylor series expansions, in an arbitrary Universe containing cold dark matter and a scalar field. By angle averaging we then infer the observed value of the deceleration parameter. We show that if such a Universe is accelerating, the acceleration must be primarily driven by the standard mechanism of a cosmological constant term in the scalar fields potential. If the potential is absent, the backreaction of superhorizon perturbation of the scalar field cannot drive acceleration. In particular, second order perturbations are not sufficient to explain cosmic acceleration. This rules out some models which have been proposed in the literature [34, 35].

For the remainder of this thesis, we assume the presence of a cosmological constant to describe the effects of dark energy.

1.3 Standard Candles

One method of observationally probing the properties of dark energy is to accurately measure the redshifts and luminosity distances of distant sources. Many existing and planned surveys have targeted type Ia supermovae, which act as standard candles. A standard candle is an object, such as a supernova or a variable star, whose intrinsic luminosity is known. For a standard candle, by comparing the measured apparent luminosity to the known intrinsic luminosity, one can calculate its distance.

Type Ia supernovae are good standard candles. They are produced by explosions of white dwarf stars in binary star systems. A companion red giant star ejects its material and deposits it on the white dwarf until the smaller star reaches a characteristic mass limit, the Chandrasekhar mass, at which point the white dwarf becomes unstable and explosively burns its nuclear fuel. These explosions have been well studied for nearby Type Ia supernovae where it is found that the peak brightness can be inferred from the decay time of the light curve. The method of inferring intrinsic luminosity has been accurately calibrated using measurements of nearby supernavae. Exampls of light curves for several different nearby supernovae are shown in Figure 1.6.

1.4 Uncertainty in luminosity distance measurements

It has long been recognized that perturbations to luminosity distances from weak gravitational lensing will be a source of error for cosmological studies, both statistical and systematic. An analogy is the light observed from the sun.

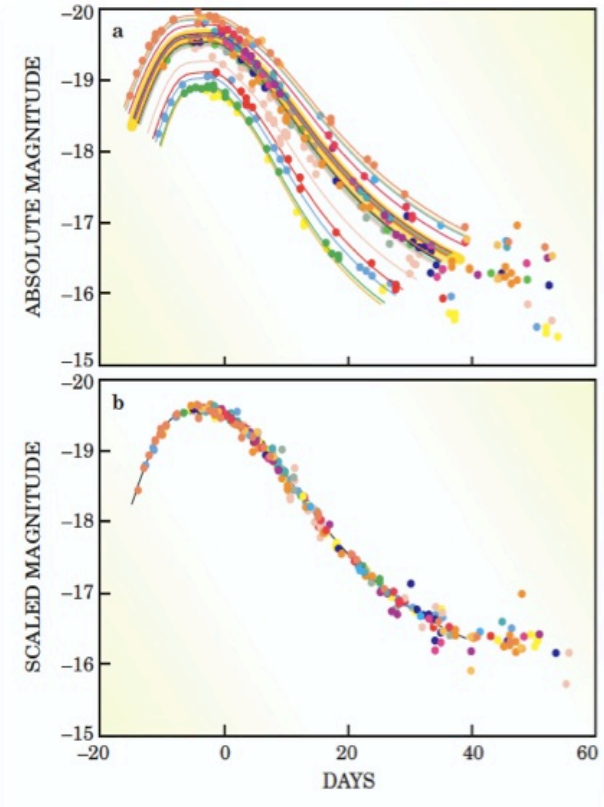

Figure 1.6: The first plot is the absolute magnitude of various Type Ia supernovae explosions as a function of time. The second plot shows that all the curves coincide after rescaling both the time and luminosity [5].

When light from the sun passes through clouds, there is a significant decrease in the number of photons collected on the surface of the earth. Hence uncertainties can creep into the measurement of luminosity of sunlight from the surface of the earth.

We study similar uncertainties in luminosities of distant sources due to gravitational lensing, caused by galaxies and dark matter halos and also due to large

scale structures like voids. Voids are roughly 1000 times the size of galaxies. Most of the mass in the Universe is observed to be concentrated on the edges of these voids, usually in the form of filamentary and wall-like structures which themselves are composed of galaxy clusters. The graviational lensing due to matter structures on these two scales is different and we study various qualitative and quantitative differences. These results will be useful for separating out lensing errors from future cosmological surveys.

One approach to studying lensing effects is to use simplified analytical models of the distribution of matter that allow rapid computation of the full probability distribution of magnifications. In our work in Chapter 3, we follow this approach. We develop an idealized "Swiss cheese" model of large scale structure to study the effect of density inhomogeneities on luminosity distances. In this model the hollow regions of the Swiss cheese represent voids which are large scale structures on whose surfaces most of the matter is located. The smooth cheese regions represent the background cosmology. In our models we consider a Friedman-Robertson-Walker background containing dark energy, nonrelativistic baryonic matter and nonrelativisitic dark matter.

As a bundle of light rays from a standard candle passes through this Swiss cheese Universe, three things can happen. For simplicity, assume that the source located in an FRW background region. First, if the bundle of rays passes through cheese-like FRW regions, the area of the bundle remains unchanged. Second, if the bundle passes through a region that is denser than FRW, the rays will get gravitationally lensed and will be focused, decreasing the area of the bundle. Finally, if the bundle passes through an area that is underdense compared to FRW, the rays will diverge and hence the area will increase. This increase or

decrease in area happens multiple times as the rays travel from the source to an observer's telescope on the earth resulting in an overall net magnification or demagnification. Thus an uncertainty in the area implies an uncertainty in the inferred distance to the source.

1.5 Lensing degradation of luminosity distance measurements

In Chapter 4, we extend the studies of Chapter 3 to include the effect of the clustering of matter on galaxy scales. Our model seeks to capture the property that most of the matter is concentrated in galaxy halos on the outer edges of voids while the void interiors are relatively sparse. Our first model is an extension of our previous work where we idealize the interior of a spherical void as a uniform underdense region and the outer shell is a randomized distribution of galaxy halos with so-called Navarro–Frenk–White (NFW) profiles.

Our second model retains the randomly distributed galaxy halos on the surface of the void and replaces the interior uniform density with randomly distributed galaxy halos with NFW profiles. Even though neither of these models represent realistic matter distributions within a void, we expect that they capture the main qualitative features of lensing and that the results quantitatively represent the limits of lensing.

The standard deviation due to voids and halos is a factor ~ 4 larger than that due to voids alone which we studied in our previous work with a small finite shell thickness. The distributions of magnifications are bimodal with a peak at positive magnification due to intersections with halos, and a peak at negative magnification due to rays passing through the underdense void interiors.

We find that the mode of the distributions is dominated by rays that don't hit any halos. We also study the effect of removing the voids and just from halos, and find that it does not significantly change the variance but does significantly change the demagnification tail. The scale of voids is unimportant, the only relevant thing is the fraction of the volume that is in the Friedman-Robertson-Walker background. The only discernable effect of voids is seen when the void interior is smoothly distributed matter.

Our model is complementary to many of the existing models in that we focus on lensing produced by structures at the largest scales, voids and sheets, rather than that produced by individual galaxies and halos, the focus of many existing models.

CHAPTER 2

BACKREACTION OF SUPERHORIZON PERTURBATIONS IN SCALAR FIELD COSMOLOGIES

2.1 Introduction and Summary

The nature of dark energy is one of the most important outstanding problems in cosmology. A simple explanation is achieved by inserting a cosmological constant in Einstein's field equation. However, there are well known naturalness and fine tuning problems associated with a cosmological constant [11]. The simplest models offering a solution to the fine tuning problem are quintessence models [12]. Cosmic acceleration can also in principle be explained by modifying general relativity at large distance scales. Examples include f(R) theories [13, 14, 14, 15, 16, 17] and the Dvali-Gabadadze-Porrati model [18, 19, 20, 21, 22, 23, 24]. For a description of more models see the review [25] and references within. The naturalness problem persists in most of these dynamical models.

It has also been suggested that the acceleration of the Universe can be explained by a purely general relativistic effect involving no new physics, the backreaction of perturbations [26, 27, 28, 29, 30]. See Refs. [27, 28, 31, 32, 33, 34] for a review of the backreaction idea. By taking a spatial average of Einstein's equations in a particular gauge, one can obtain Friedmann equations for an effective spatially averaged scale factor $a(t)$ with extra driving terms coming from backreaction [35, 36, 37, 38, 39]. These extra driving terms can in principle drive an acceleration. Although the conventional viewpoint is that the effect of backreaction is small, some have argued that it can be large enough to account for

cosmic acceleration.

A problem with this theoretical approach is that the spatially averaged scale factor is not related in any simple way to quantities we observe, which average over our past light cone. See Refs. [32, 40] for a discussion of this issue.

There are two variants of the backreaction explanation. The first is that cosmic acceleration is caused by the backreaction of *superhorizon* perturbations. In particular Kolb et al [26, 27] looked at inflation-generated perturbations to a Friedmann-Robertson-Walker (FRW) universe, and claimed that at second order one could obtain a negative deceleration parameter. This claim was disproved in Refs. [41, 42, 43] [1].

The second variant of the backreaction explanation is that the backreaction of *subhorizon* perturbations can explain cosmic acceleration [28, 45, 46, 47, 48]. This seems unlikely but the issue has not yet been settled. We will not discuss the subhorizon backreaction issue here.

In this chapter we focus on the backreaction of superhorizon perturbations in the present day Universe [2]. In particular we show that for a Universe with cold dark matter and a scalar field (as in standard quintessence models), achieving a value $q_0 \simeq -0.5$ of the deceleration parameter requires a non-zero potential. Our method of analysis is as follows [41, 42]. We compute luminosity distance as a function of redshift using Taylor series expansions, in an arbitrary Universe containing cold dark matter and a scalar field. By angle averaging we then infer the observed value of the deceleration parameter q_0. Our result shows that if

[1] We also point to Ref. [44] for other arguments against cosmic acceleration caused by backreaction

[2] We note that there is also a considerable literature on superhorizon backreaction during the inflationary era, which does have a local physical effect in two scalar field inflation models [49, 50, 51, 52, 53, 54, 55, 56, 57, 58, 59].

such a Universe is accelerating, that acceleration must be primarily driven by the standard mechanism of a cosmological constant term in the scalar field's potential. If the potential is absent, the backreaction of superhorizon perturbation of the scalar field can not drive acceleration. In particular, second order perturbations are not sufficient to explain cosmic acceleration.

Our analysis was motivated in part by a claim by Martineau and Brandenberger [60] that the acceleration could be caused by the backreaction of superhorizon perturbations of a scalar field. These authors consider a model in which a single scalar field both drives inflation and is also present today. Modeling the scalar field perturbations using an effective energy momentum tensor, they argue that the effect of those perturbations can be of the right magnitude and character to cause acceleration. Our result shows that this model cannot be correct. We discuss further in Sec. III below a possible reason for our differing results.

2.2 Computation of Deceleration Parameter

We start by describing our theoretical framework and assumptions, which are a slightly modified version of those used in Ref. [41]. We consider the Universe in the matter dominated era, described by general relativity coupled to a pressureless fluid describing cold dark matter (we neglect baryons and radiation), together with a light scalar field. Our starting point is the assumption that backreaction is dominated by the effect of superhorizon perturbations. If this is true, then backreaction should also be present in a hypothetical, gedanken Universe in which all the perturbation modes which are subhorizon today are set

to zero at early times. Generic solutions to the field equations for this gedanken Universe can be described using local Taylor series expansions rather than via perturbations of Friedmann-Robertson-Walker models, since all the fields vary on length scales or time scales of order the Hubble time or larger. This greatly simplifies the analysis.

The three equations which describe the dynamics of the gedanken universe are the following:

$$G_{\alpha\beta} = 8\pi\Big[(\rho + p)\, u_\alpha u_\beta + p g_{\alpha\beta} + \nabla_\alpha\phi\nabla_\beta\phi$$

$$-\frac{1}{2} g_{\alpha\beta}\,(\nabla\phi)^2 - V(\phi)\, g_{\alpha\beta}\Big], \tag{2.1}$$

$$\Box\phi - V^{'}(\phi) = 0, \tag{2.2}$$

and

$$\nabla_\alpha\left[(\rho + p)\, u^\alpha u^\beta + p g^{\alpha\beta}\right] = 0. \tag{2.3}$$

Here ρ, p and u_α are the density, pressure and four velocity of matter, ϕ is the scalar field and $V(\phi)$ is its potential. Later we will specialize to cold dark matter for which $p = 0$.

Next we define the specific deceleration parameter q_0 that we use. As discussed in Ref. [43], there are several different possible definitions for non-FRW cosmological models. The definition we choose matches closely with how q_0 is actually measured.

Let us start by fixing a comoving observer at point O in spacetime. We label null geodesics on $O's$ past null cone in terms of the spherical polar angles (θ,ϕ) of a local Lorentz frame at O that is comoving with the cosmological fluid. We parameterize each null geodesic in terms of an affine parameter λ and corresponding 4-momentum $\vec{k} = d/d\lambda$. For a given source S on such a null geodesic at affine parameter λ, we define the redshift as

$$1 + z\,(\theta,\phi,\lambda) = \frac{\vec{k}.\vec{u}|_S}{\vec{k}.\vec{u}|_O}. \tag{2.4}$$

The luminosity distance $\mathcal{D}_{\mathcal{L}}\,(\theta,\phi,\lambda)$ of the source S is defined in the usual way in terms of the luminosity $(dE/dt)_S$ of an assumed comoving isotropic source at S and the energy per unit area per unit time $(dE/dtdA)_O$ measured at O:

$$\left(\frac{dE}{dtdA}\right)_O = \frac{1}{4\pi\mathcal{D}_{\mathcal{L}}{}^2}\left(\frac{dE}{dt}\right)_S. \tag{2.5}$$

Assuming that the wavelength of the radiation from S is much smaller than the radius of curvature of spacetime, we can use geometric optics to compute the observed energy flux in Eq. (2.5) and thus the luminosity distance $\mathcal{D}_{\mathcal{L}}$; see, for example Ref. [61]. Finally, we can eliminate the affine parameter λ between Eqs. (2.4) and (2.5) and compute the luminosity distance as a function of spherical coordinates and redshift to obtain $\mathcal{D}_{\mathcal{L}} = \mathcal{D}_{\mathcal{L}}\,(\theta,\phi,z)$.

Next, to define the deceleration parameter q_0, we expand the luminosity distance in powers of redshift. The result is

$$\mathcal{D}_{\mathcal{L}}\,(\theta,\phi,z) = A\,(\theta,\phi)\,z + B\,(\theta,\phi)\,z^2 + O\left(z^3\right), \tag{2.6}$$

where $A\,(\theta,\phi)$ and $B\,(\theta,\phi)$ are functions that only have angular dependences. We

then define the Hubble parameter H_0 and the deceleration parameter q_0 in terms of angular averages of the above functions. The standard FRW relation is

$$\mathcal{D}_{\mathcal{L}}(\theta,\phi,z) = H_0^{-1} z + H_0^{-1}(1-q_0)\frac{z^2}{2} + O\left(z^3\right). \tag{2.7}$$

Comparing the expansions (2.6) and (2.7) motivates the following definitions of H_0 and q_0:

$$H_0 \equiv \left\langle A^{-1}\right\rangle, \qquad q_0 \equiv 1 - 2H_0^{-2}\left\langle A^{-3}B\right\rangle, \tag{2.8}$$

where $\langle ... \rangle$ denotes an average over the angles θ and ϕ. Note that there is some ambiguity in these definitions. For example one could take $q_0 = 1 - 2\left\langle A^{-1}B\right\rangle$ instead. We choose the form (2.8) for computational convenience, and we will argue below that the differences are unimportant.

We next explicitly evaluate the expressions (2.8) for H_0 and q_0. We consider generic solutions to the equations (2.1) - (2.3), described by local Taylor series expansions [62] about the observer O. The expressions for the functions A and B were computed in Ref. [41], and are

$$A(\theta,\phi) = \frac{1}{(\nabla^\alpha u^\beta)\,k_\alpha k_\beta}, \tag{2.9}$$

$$B(\theta,\phi) = \frac{2}{(\nabla^\alpha u^\beta)\,k_\alpha k_\beta} + \frac{\left(\nabla^\alpha\nabla^\beta u^\gamma\right)k_\alpha k_\beta k_\gamma}{2\left[(\nabla^\alpha u^\beta)\,k_\alpha k_\beta\right]^3}, \tag{2.10}$$

where all quantities on the right hand sides are evaluated at O. By inserting the expression for $A(\theta,\phi)$ into the definition (2.8) of H_0 and evaluating the angular average, we obtain

$$H_0 = \frac{1}{3}\Theta, \tag{2.11}$$

where

$$\Theta = \nabla_\alpha u^\alpha \tag{2.12}$$

is the expansion of the cosmological fluid. This is the same result as was obtained in Ref. [41].

Next, we insert the expressions (2.9) and (2.10) for $A(\theta,\phi)$ and $B(\theta,\phi)$ into (2.8) to obtain

$$\frac{1}{2}H_0^2(1-q_0) = 2\left\langle\left[\left(\nabla^\alpha u^\beta\right)k_\alpha k_\beta\right]^2\right\rangle$$

$$+\frac{1}{2}\left\langle\left(\nabla^\alpha\nabla^\beta u^\gamma\right)k_\alpha k_\beta k_\gamma\right\rangle. \tag{2.13}$$

We now evaluate these angular averages using the same techniques as in Ref. [41]. The only difference from the computation of Ref. [41] arises when we eliminate a factor of the Ricci tensor $R_{\alpha\beta}$ using the field equations. Here that elimination generates extra terms involving the scalar field, from the equation of motion (2.1). The final result is

$$q_0 = \frac{4\pi}{3H_0^2}\left[\rho + 3p - V(\phi) + 2\nabla_\alpha\phi\nabla_\beta\phi u^\alpha u^\beta\right]\Big|_O$$

$$+\frac{1}{3H_0^2}\left(a_\alpha a^\alpha + \frac{7}{5}\sigma_{\alpha\beta}\sigma^{\alpha\beta} - w_{\alpha\beta}w^{\alpha\beta} - 2\nabla_\alpha a^\alpha\right)\Big|_O. \tag{2.14}$$

Here $\sigma^{\alpha\beta}$, $w^{\alpha\beta}$ and a^{α} are the shear, vorticity and 4-acceleration of the fluid, defined by

$$\nabla_{\alpha} u_{\beta} = \frac{1}{3}\Theta g_{\alpha\beta} + \sigma_{\alpha\beta} + w_{\alpha\beta} - a_{\beta} u_{\alpha}, \tag{2.15}$$

with

$$\sigma_{\alpha\beta} = \sigma_{\beta\alpha} \text{ and } w_{\alpha\beta} = -w_{\beta\alpha}. \tag{2.16}$$

2.3 Discussion

We now specialize our result (2.14) to a pressureless fluid. The 4-acceleration then vanishes and we have

$$q_0 = \frac{4\pi G}{3H_0^2}\left[\rho - V(\phi) + 2\nabla_{\alpha}\phi\nabla_{\beta}\phi u^{\alpha}u^{\beta}\right]\Big|_O$$

$$+\frac{1}{3H_0^2}\left(\frac{7}{5}\sigma_{\alpha\beta}\sigma^{\alpha\beta} - w_{\alpha\beta}w^{\alpha\beta}\right)\Big|_O. \tag{2.17}$$

We now argue that the only way to achieve $q_0 \approx -0.5$, as required by observations, is to have $V(\phi_0)$ be large and positive, where ϕ_0 is the value of ϕ evaluated at the observer.

We can estimate the terms $\sigma_{\alpha\beta}\sigma^{\alpha\beta}$ and $w_{\alpha\beta}w^{\alpha\beta}$ in Eq. (2.17) to be $\sim (\delta v)^2 / l^2$, where δv is the typical scale of peculiar velocity perturbations, and l is the scale over which the velocity varies. Since we have assumed that subhorizon perturbations are absent we have $l \gtrsim H_0^{-1}$. This implies that the contributions from

these terms are of order $\delta q_0 \sim (\delta v)^2 \simeq 10^{-4}$. Since the measured value of q_0 is $q_0 \sim -0.5$, these terms cannot contribute significantly to the deceleration parameter.

In the first term in Eq. (2.17), the quantities ρ and $2\nabla_\alpha\phi\nabla_\beta\phi u^\alpha u^\beta$ are always positive (the second term is the square of $\sqrt{2}\nabla\phi_\alpha u^\alpha$). This means that the potential term has to be larger than the sum of these two terms to get negative deceleration. Thus, a large negative deceleration must come primarily from the potential.

We note that this result differs from that obtained by Martineau and Brandenberger in Ref. [60], who found that the backreaction of superhorizon perturbations *could* drive cosmic acceleration via a mechanism not involving the potential. A possible reason for the difference is the fact that different measures of cosmic acceleration are used in the two different analyses. The authors of Ref. [60] use a measure that is based on averages over a spatial slice at a given instant of time (which is inherently gauge dependent). We use a different measure which is essentially an average over the past light cone of the observer, and is gauge independent. Moreover, our measure corresponds more closely to the actual deceleration parameter that has been measured.

Finally, we note that the specific choices of angle averaging prescriptions in the definitions (2.8) of the Hubble parameter and deceleration parameter are not unique. However, as was argued in Ref. [41], the change that results from adopting other definitions is negligible. For example, one could consider the alternative definition

$$q_0 \equiv 1 - 2H_0 \langle B \rangle \tag{2.18}$$

of the deceleration parameter. In Ref. [41] it was shown that this alters the final result (2.17) in three ways: (i) Changing the numerical coefficients of the shear squared and vorticity squared terms by an amount of order unity, which does not affect our conclusions; (ii) The addition of new terms that are comparable to the shear squared and vorticity squared terms; and (iii) The addition of new terms that are suppressed compared to the shear squared and vorticity squared terms by one or more powers of the dimensionless ratio (non-isotropic part of $\nabla_\alpha u_\beta$)/(isotropic part of $\nabla_\alpha u_\beta$). This dimensionless ratio is constrained observationally to be small compared to unity, since peculiar velocities on Hubble scales today are small. The same arguments continue to apply in the present context, since the scalar field dependent terms in (2.17) are unchanged by the change in definition of q_0.

2.4 Conclusion

The backreaction of perturbations is sometimes considered to be a candidate for explaining cosmic acceleration [63]. Many techniques have been developed to explore the effects of backreaction. In this chapter, we computed the deceleration parameter measured by comoving observers in a hypothetical universe with all perturbation modes which are subhorizon today set to zero at early times. We considered a universe containing cold dark matter and a minimally coupled scalar field. We showed that one can obtain a large negative value of the deceleration parameter in this context only if the deceleration is primarily produced by the scalar field's potential.

CHAPTER 3

LUMINOSITY DISTANCE IN SWISS CHEESE COSMOLOGY WITH RANDOMIZED VOIDS.

3.1 Introduction

3.1.1 Background and Motivation

A number of surveys are being planned to determine luminosity distances to various different astronomical sources, and to use them to constrain properties of the dark energy or modifications to gravity that drive the cosmic acceleration. It has long been recognized that perturbations to luminosity distances from weak gravitational lensing will be a source of error for these studies, both statistical and systematic [64, 65, 66, 67, 68]. For supernovae the lensing noise becomes significant only at high redshifts [69], but for gravitational wave sources the lensing noise dominates over the intrinsic luminosity scatter [70, 71]. Theoretical predictions for the magnification probability distribution can be folded into the data analysis of surveys to improve the results [72], and in particular it is possible to exploit the known non-Gaussian nature of this distribution [73]. In addition, it is possible to treat the "lensing noise" in luminosity distances as a signal in its own right, which provides useful information [74]. (A tentative detection of this signal in supernovae data has been claimed in Ref. [75].) For these reasons, it is useful to have a detailed understanding of the magnification probability distribution.

There are a number of methods that have been used to study the effects of

weak lensing on luminosity distances:

- Weak lensing theory can be used to predict the variance of the magnification distribution from the matter power spectrum [76]. However, the accuracy of this approach is limited and in particular it does not allow one to probe the non-Gaussian tails of the distribution[1].
- One can use numerical ray tracing using the results of cosmological simulations of large scale structure, such as the Millennium simulation [78] and the Coyote Universe project [79], see, eg. Ref. [80]. This approach is highly accurate and is based on a realistic density distribution. However it requires substantial computational power and is also limited in some other respects. The largest simulations to date are are confined to a cube of comoving size $z \sim 0.16$, so only a limited range of source redshifts can be considered. Although the calculations evolve large scale structure nonlinearly, it is impractical to get a continuous description of the evolution, which is needed for computing the perturbations to light ray paths; only snapshots of the density distribution are available. Finally, because the calculations required to evolve the matter distribution are formidable, it can be difficult to comprehensively survey the space of the underlying parameters of the model, such as the primordial perturbation spectrum.
- A third approach is to use simplified analytical models of the distribution of matter that allow rapid computation of the full probability distribution of magnifications, see, eg., Refs. [65, 67, 81, 82].

In this chapter we follow the third approach. We develop an idealized

[1]We note however that there is a proposal for an approximate "universal probability distribution" for magnifications that takes as input only the variance of the distribution as predicted by weak lensing theory, and which would allow prediction of the non-Gaussian tails [77].

"Swiss cheese" model [83, 65, 84, 85, 86] of large scale structure to study the effect of density inhomogeneities on luminosity distances. Our model is complementary to many of the existing models in that we focus on lensing produced by structures at the largest scales, voids and sheets, rather than that produced by individual galaxies and halos, the focus of many existing models.

3.1.2 Our void model

In "Swiss cheese" models [83, 65, 84, 85, 86], the Universe contains a network of spherical, non-overlapping, mass-compensated voids. The voids are chosen to be mass compensated so that the potential perturbation vanishes outside each void. We idealize these models even further by assuming that each void consists of a central, uniformly underdense region surrounded by a zero thickness shell. Mass flows outward from the evacuated interior and is then trapped on the wall. Although it would be more realistic to consider voids with smooth density profiles, this very simplified model should capture the essence of the effect of large scale density inhomogeneities on luminosity distances. Since voids in the observable Universe tend to be surrounded by shells that are relatively thin compared to the size of their evacuated interiors, the idealization of zero thickness may not be a severe simplification, particularly because we expect that the main effect of inhomogeneities on the luminosity distance depends only on the integral of the density contrast along the line of sight from the source to the observer. A key feature of our idealized models is that they can be evolved in time continuously and very simply.

Within the context of this highly idealized class of models, we study the dis-

tribution of magnitude shifts relative to what would be found in a smooth cold dark matter (CDM) model of the Universe with a cosmological constant, Λ, for different void sizes and present day interior underdensities, and for a range of different source redshifts. Moreover, although we shall use a Newtonian description that is valid as long as the void radii are small enough compared with the Hubble length H_0^{-1}, the calculations can be made fully relativistic if desired. (We discuss some corrections that are higher order in H_0R, where R is the void radius.)

This is a follow-up to our earlier work [83] (henceforth VFW08), in which we considered the effect of a randomized set of voids with a single and rather large comoving radius, 350 Mpc, using a particular model for a smooth underdense interior inside a mass compensated shell. That study found that for a source with redshift $z_s = 1.8$, the mean magnitude shift relative to smooth flat, CDM for an ensemble of realizations of large scale voids was unimportant (-0.003), but the distribution of magnitude shifts was fairly broad, with a standard deviation of about 0.1. Here, we consider a wider range of redshifts and void sizes, and compute magnitude shifts relative to a more realistic ΛCDM background with matter density today $\Omega_M = 0.3$ and dark energy density today $\Omega_\Lambda = 0.7$.

3.1.3 Predictions for lensing noise

Our results for the standard deviation σ_m of the magnitude shifts are summarized by the approximate fitting formula

$$\sigma_m \approx (0.027 \pm 0.0007)\left(\frac{R}{35\,\mathrm{Mpc}}\right)^{\alpha}\left(\frac{f_0}{0.9}\right)^{\beta}\left(\frac{z_s}{1.0}\right)^{\gamma}. \tag{3.1}$$

Here R is the comoving radius of the voids, z_s is the source redshift, and

f_0 is the fraction of the total void mass in its shell today. The exponents are $\alpha = 0.51 \pm 0.03$, $\beta = 1.07 \pm 0.04$, $\gamma = 1.34 \pm 0.05$. This fit is accurate to $\sim 20\%$ for $35\,\mathrm{Mpc} \leq R \leq 350\,\mathrm{Mpc}$, $0.01 \leq f_0 \leq 0.9$, and $0.5 \leq z_s \leq 2.1$. The mean magnitude shift is again unimportant, roughly a factor of ten smaller than the standard deviation (3.1).

Our result (3.1) is computed in the limit of zero shell thickness. This idealization is not very realistic, since as we discuss in Sec. 3.3 below there is a logarithmic divergence in the variance of the lensing convergence in the zero thickness limit. This divergence arises from rays that pass very near to the void walls. The variance in the magnitude shift, however, is finite because of the nonlinear dependence of magnitude shift on lensing convergence; the divergence is cut off at lensing convergences of order unity. (The divergence can also get regulated by finite sampling effects; see Sec. 3.3). To address this issue we also consider a more realistic model with void walls of some finite thickness Δr. We estimate in Sec. 3.3.4 that for $f_0 = 0.9$, $R = 35$ Mpc, and $z_s = 1.0$, the standard deviation in magnitude shift is

$$\sigma_m \approx 0.013 \sqrt{1 + 0.23 \ln\left(\frac{1\,\mathrm{Mpc}}{\Delta r}\right)}, \tag{3.2}$$

a factor of ~ 2 smaller than the thin-shell limit (3.1) for $\Delta r = 1$ Mpc.

The rms magnitude shift (3.2) due to voids is a factor of ~ 3 smaller than that computed from individual galaxies and halos [67], in accord with expectations from weak lensing theory using the power spectrum of density perturbations (see Ref. [68] and Appendix 3.7). Thus lensing due to voids is subdominant but not negligible.

We also use our model to estimate the sizes of various nonlinear effects that

go beyond linear, weak-lensing theory. We estimate that for $R = 35$ Mpc voids, the dispersion σ_m is altered by $\sim 4\%$ by lens-lens coupling, by $\sim 3\%$ by shear. There are also large nonlinearities ($\sim 30\% - 40\%$) in our model that arise from the nonlinearity of void evolution. These results are qualitatively in agreement with some previous studies of nonlinear deviations from weak lensing theory [87, 88, 89].

We also study the source-lens clustering effect [90], the fact sources are more likely to be located in high density regions, which enhances the probability of a lens being located near the source. We estimate that the corresponding bias in the distribution of magnifications is negligible in our model.

3.1.4 Organization of this chapter

This chapter is organized as follows. Section 3.2 reviews our Swiss cheese void model. We discuss how the voids evolve in an FRW background and describe the model parameters. Next, we describe how our void locations are randomized, by choosing impact parameters randomly as light rays exit one void and enter the next. Finally, we describe our method of computing the magnification. Section 3.3 describes our simple analytical model which reproduces the results of the simulations to within $\sim 30\%$. It also describes a modification of our void model in which the shell walls are given a finite thickness, and gives the corresponding analytical results. Section 3.4 gives the results of our Monte Carlo simulations for the the probability distributions of magnifications, and discusses the dependence of the variance on the parameters of the model. In Section 3.5, we study the source-lens clustering effect and the associated bias. Section 3.6

summarizes our results and their implications. In Appendix 3.7 we discuss the power spectrum of our void model and the corresponding weak lensing prediction. Appendix 3.8 reviews the derivation of the method we use to compute the magnification distribution. Finally, Appendix 3.9 is a comparison of our results with other recent studies of lensing due to voids [91, 81, 82, 92, 93, 94]. Our results are broadly consistent with these previous studies but our model is simpler in several respects.

3.2 Simple Model of Lensing due to Voids

In this section we describe our simplified Swiss cheese model of large scale voids, and explain how we compute the distribution of magnifications in the model.

3.2.1 Newtonian model of a single void

As discussed in the introduction, we will consider void radii R ranging from 35 Mpc to 350 Mpc, which are small compared to the Hubble length. Therefore we can use Newtonian gravity to describe each void; the corresponding error is of order $(H_0 R)^2 \ll 1$ which we ignore.

We choose the background cosmology in which we place our voids to be an FRW Universe with matter fraction Ω_M and cosmological constant fraction $1 - \Omega_M$. We denote by $a_{\rm ex}(t)$ the corresponding scale factor, which is normalized

so that $a_{\rm ex}(t) = 1$ today. It satisfies the Friedman equation

$$\left(\frac{\dot{a}_{\rm ex}}{a_{\rm ex}}\right)^2 = H_0^2\left(\frac{\Omega_M}{a_{\rm ex}^3} + 1 - \Omega_M\right), \tag{3.3}$$

where H_0 is the Hubble parameter, which has the solution

$$\frac{3H_0 t\sqrt{1-\Omega_M}}{2} = \sinh^{-1}\left(\frac{a_{\rm ex}^{3/2}}{a_\Lambda^{3/2}}\right). \tag{3.4}$$

Here $a_\Lambda = (\Omega_M/(1-\Omega_M))^{\frac{1}{3}}$ is the scale factor at which the cosmological constant starts to dominate.

Our void model consists of a spherical region of constant comoving radius R, with a uniform density interior surrounded by a thin shell. We assume that the void is mass compensated, so the total mass enclosed is the same as what it would be in FRW, namely

$$M = \frac{H_0^2\Omega_M R^3}{2G}. \tag{3.5}$$

We denote by $f(t)$ the fraction of this mass in the thin shell, so that the mass in the interior is $[1 - f(t)]M$. The fractional density perturbation in comoving coordinates $\delta_{\rm m}(\mathbf{x}, t) = \delta\rho(\mathbf{x}, t)/\rho$ is therefore

$$\delta_{\rm m}(\mathbf{x}, t) = -f(t)\Theta(R - r) + \frac{1}{3}f(t)R\delta(r - R), \tag{3.6}$$

where $\Theta(x)$ is the function defined by $\Theta(x) = 1$ for $x > 0$ and $\Theta(x) = 0$ for $x < 0$.

The corresponding potential perturbation ϕ, in a Newtonian gauge in which the metric has the form

$$ds^2 = -(1 + 2\phi)\,dt^2 + a_{\rm ex}^2(t)\,(1 - 2\phi)\,d\mathbf{x}^2, \tag{3.7}$$

is given by solving the Poisson equation $\nabla^2\phi = 3H_0^2\Omega_M\delta_{\rm m}(\mathbf{x}, t)/(2a_{\rm ex})$. This gives

$$\phi(\mathbf{x}, t) = \frac{H_0^2\Omega_M f(t)}{4a_{\rm ex}(t)}\left(R^2 - r^2\right)\Theta(R - r). \tag{3.8}$$

The corresponding radial acceleration is

$$a_r = -\frac{H_0^2 \Omega_M f(t)}{2 a_{\rm ex}(t)^2} r \Theta(R - r).$$

For each void, the potential will take the form (3.8) in a spherical polar coordinate system centered on that void, and the total potential is given by summing over the voids. The potential vanishes in between the voids.

We next discuss how to compute the time evolution of the fraction $f(t)$ of the void mass in the thin shell. We will work to leading, Newtonian order in $(H_0 R)^2$, and we will also neglect the surface pressure that would arise in a relativistic calculation. The uniform interior behaves like a positive energy FRW cosmology. It has negative curvature, $k < 0$, and a scale factor $a_{\rm in}(t)$ that obeys the equation

$$\left(\frac{\dot{a}_{\rm in}}{a_{\rm in}}\right)^2 = H_0^2 \left(\frac{\Omega_M}{a_{\rm in}^3} + 1 - \Omega_M - \frac{k}{a_{\rm in}^2 H_0^2}\right), \tag{3.9}$$

since the cosmological constant is the same inside and outside the void but the matter density is not. We define the positive constant $a_0 = -\Omega_M H_0^2/k$, the inverse of which is proportional to the density contrast at early times. The solution to Eq. (3.9) is

$$\frac{3 H_0 t \sqrt{1 - \Omega_M}}{2} = \int_0^{\left(\frac{a_{\rm in}}{a_\Lambda}\right)^{\frac{3}{2}}} \frac{dx}{\sqrt{1 + x^2 + x^{\frac{2}{3}} \frac{a_\Lambda}{a_0}}}. \tag{3.10}$$

This solution assumes that $a_{\rm in} = a_{\rm ex} = 0$ at $t = 0$, so that the interior and the exterior regions started expanding at the same time. Otherwise the deviations from FRW are large at early times. Eliminating t between Eqs. (3.4) and (3.10) gives the relationship between $a_{\rm in}$ and $a_{\rm ex}$, which is

$$\sinh^{-1}\left(\frac{a_{\rm ex}^{3/2}}{a_\Lambda^{3/2}}\right) = \int_0^{\left(\frac{a_{\rm in}}{a_\Lambda}\right)^{\frac{3}{2}}} \frac{dx}{\sqrt{1 + x^2 + x^{\frac{2}{3}} \frac{a_\Lambda}{a_0}}}. \tag{3.11}$$

Note that the above equations imply that $a_{\rm in} > a_{\rm ex}$, as $k < 0$. The density of the interior is equal to the mean FRW density times $(a_{\rm ex}/a_{\rm in})^3 < 1$, and so the fraction of mass in the shell is

$$f(t) = 1 - \left(\frac{a_{\rm ex}}{a_{\rm in}}\right)^3 . \tag{3.12}$$

We numerically solve Eq. (3.11) to obtain $a_{\rm ex}/a_{\rm in}$ as a function of $a_{\rm ex}/a_\Lambda$, Ω_M and a_0. In the remainder of the chapter, we will parameterize our void models in terms of the value today $f_0 = f(t_0)$ of the mass fraction $f(t)$ in the shell. We will usually pick $f_0 = 0.9$. The parameter a_0 can be computed from f_0 and Ω_M.

3.2.2 Algorithm for randomization of void placement

We now discuss how we choose the number and locations of voids in our model. In some previous studies [95, 96, 97], the centers of all the voids encountered by a given ray were chosen to be collinear, so that the ray passed through the centers of all the voids. In these studies the lensing demagnification was large enough to successfully mimic the effects of dark energy. However, as discussed in VFW08, the large demagnification was an artifact of the non-randomness of the void locations, which is not in accord with observations of the distribution of voids [98, 99, 100, 101]. In this chapter, we use a more realistic void distribution, which we compute according to the following procedure:

1. Fix the comoving void size R.
2. Fix the redshift of the source z_s.
3. Place voids all along the ray from the source to the observer, lined up so that they are just touching. The source and the observer are placed in

FRW regions. The distance from the source to the shell of the adjacent void is chosen to be a fixed small parameter, and the distance between the observer and the shell of the adjacent void then depends on the number of voids that can fit between the source and observer.

4. Randomize impact parameters by shifting each void in a random direction perpendicular to the direction of the light ray, so that the square b^2 of the impact parameter is uniformly distributed between 0 and R^2.

Note that with this algorithm, each ray spends some time in FRW regions between each pair of voids. An alternative procedure would that used by Holz & Wald [65], in which after exiting a void, a ray immediately enters another void without traversing an FRW region. In this model the effective packing fraction of voids would be a factor ~ 2 or so higher than in our model, and the rms magnifications and demagnification would be correspondingly enhanced.

3.2.3 Method of computing magnification along a ray

We now turn to a description of the method we use to compute the magnification for a ray propagating through a Universe filled with randomly placed voids, as described in the last subsection. Our method is essentially a modification of the method introduced by Holz & Wald [65], and goes beyond weak-lensing theory. In this section we describe the computational procedure; a derivation is given in Appendix 3.8.

Starting from the perturbed FRW metric (3.7), we consider an observer at $t = t_0$ (today) and $\mathbf{x} = 0$, or equivalently at $\eta = \eta_0$, where $\eta = \int dt/a_{\rm ex}(t)$ is

conformal time. We consider a source at $\mathbf{x} = \mathbf{x}_s = x_s\mathbf{n}$, where $\mathbf{n}$ is a unit vector. The geodesic joining the source and observer in the background FRW geometry is

$$x^\alpha(x) = (\eta_0 - x,\ \mathbf{n}x), \tag{3.13}$$

for $0 \le x \le x_s$, where x is the comoving distance (or affine parameter with respect to the flat metric $d\bar{s}^2 = a_{\rm ex}(t)^{-2} ds^2 = -d\eta^2 + d\mathbf{x}^2$). We denote by $\vec{k} = d/dx = -\partial_\eta + n^i\partial_i$ the past directed tangent vector to the ray. We also introduce a pair of spatial basis vectors $\vec{e}_A$, $A = 1, 2$, so that $\vec{e}_A$ and $\mathbf{n}$ are orthonormal with respect to $d\bar{s}^2$. We define the projected Riemann tensor

$$\mathcal{R}_{AB} = \bar{R}_{\alpha\gamma\beta\delta} k^\gamma k^\delta e_A^\alpha e_B^\beta, \tag{3.14}$$

for $A, B = 1, 2$ where $\bar{R}_{\alpha\gamma\beta\delta}$ is the Riemann tensor of the perturbed FRW metric without the $a_{\rm ex}(t)^2$ factor:

$$ds^2 = -(1 + 2\phi)\, d\eta^2 + (1 - 2\phi)\, d\mathbf{x}^2. \tag{3.15}$$

Next we consider the differential equation along the ray

$$\frac{d^2}{dx^2}\mathcal{A}^A{}_B(x) = -\mathcal{R}^A{}_C(x)\,\mathcal{A}^C{}_B(x), \tag{3.16}$$

where $\mathcal{R}^A{}_C(x)$ means the projected Riemann tensor evaluated at $x^\alpha = x^\alpha(x)$, and capital Roman indices are raised and lowered with δ_{AB}. We solve the differential equation (3.16) subject to the initial conditions at the observer

$$\mathcal{A}^A{}_B(0) = 0, \qquad \frac{d\mathcal{A}^A{}_B}{dx}(0) = \delta^A{}_B. \tag{3.17}$$

Finally the magnification along the ray, relative to the background FRW metric,

is[2]

$$\mu = \frac{x_s^2}{|\det \mathcal{A}(x_s)|}, \tag{3.18}$$

where the right hand side is evaluated at the location $x = x_s$ of the source.

The matrix $\mathcal{A}(x_s)/x_s$ can be expressed as a product of an orthogonal matrix and a symmetric matrix with two real eigenvalues $1 - \kappa \pm \gamma$, where κ is called the lensing convergence and γ the shear. The magnification is therefore

$$\mu = |(1 - \kappa)^2 - \gamma^2|^{-1}. \tag{3.19}$$

This computational procedure is essentially the same as that used by Holz & Wald [65], except that Holz & Wald work in the physical spacetime rather than the conformally transformed spacetime, and at the end of the computation they compute the ratio between the quantity $x_s^2/(\det\mathcal{A})$ evaluated in the perturbed spacetime and in the background spacetime.

In ourapproach we do not need to compute a ratio, and furthermore the source term in the differential equation (3.16) vanishes in FRW regions between the voids, which simplifies the computation. See Appendix 3.8 for more details on the relation between the two approaches.

We now turn to a discussion of the method we use to compute approximate solutions to the differential equation (3.16). Consider a small segment of ray, from $x = x_1$ to $x = x_2$ say. Since the differential equation is linear, we have

[2] In our Monte Carlo simulations we discard all cases where the determinant is negative, and so the absolute value sign in Eq. (3.18) can be dropped. As explained in Ref. [65], this prescription yields the distribution of magnifications of primary images; it is not possible using the geodesic deviation equation method to compute the distribution of total luminosity of all the images of a source.

$$\begin{bmatrix} \mathcal{A}^A{}_B(x_2) \\ \dot{\mathcal{A}}^A{}_B(x_2) \end{bmatrix} = \begin{bmatrix} J^A{}_C(x_2,\ x_1) & K^A{}_C(x_2,\ x_1) \\ L^A{}_C(x_2,\ x_1) & M^A{}_C(x_2,\ x_1) \end{bmatrix} \times \begin{bmatrix} \mathcal{A}^C{}_B(x_1) \\ \dot{\mathcal{A}}^C{}_B(x_1) \end{bmatrix}. \tag{3.20}$$

for some 2×2 matrices $J,\ K,\ L,\ M$ which together form a 4×4 matrix. To linear order in $\mathcal{R}_{AB}$ we have[3]

$$J^A{}_C = \delta^A{}_C - \int_{x_1}^{x_2} dx\,(x_2 - x)\,\mathcal{R}^A{}_C(x)\,, \tag{3.21}$$

$$K^A{}_C = (x_2 - x_1)\,\delta^A{}_C - \int_{x_1}^{x_2} dx \int_{x_1}^{x} d\bar{x}\,(\bar{x} - x_1)\,\mathcal{R}^A{}_C(\bar{x})\,, \tag{3.22}$$

$$L^A{}_C = -\int_{x_1}^{x_2} dx \mathcal{R}^A{}_C(x)\,, \tag{3.23}$$

$$M^A{}_C = \delta^A{}_C - \int_{x_1}^{x_2} dx\,(x - x_1)\,\mathcal{R}^A{}_C(x)\,. \tag{3.24}$$

We evaluate these matrices for a transition through a single void, using the potential (3.8), the metric (3.15) and the definition (3.14) of $\mathcal{R}_{AB}$. We neglect the time evolution of the potential during passage through the void; the corresponding corrections are suppressed by $(H_0 R)^2$. This gives

$$J^A{}_C = \delta^A{}_C + c^2 \mathcal{P}(z) \begin{pmatrix} 1 & 4 \\ 4 & 1 \end{pmatrix}, \tag{3.25}$$

$$K^A{}_C = (x_2 - x_1)\delta^A{}_C + \frac{2}{3} c^3 \mathcal{P}(z) \begin{pmatrix} 1 & 2 \\ 2 & 1 \end{pmatrix}, \tag{3.26}$$

$$L^A{}_C = 2c\mathcal{P}(z) \begin{pmatrix} 1 - \frac{R^2}{3c^2} & 4 \\ 4 & 1 - \frac{R^2}{3c^2} \end{pmatrix}, \tag{3.27}$$

[3] Holz & Wald [65] drop all of the integrals over the projected Riemann tensor in Eqs. (3.2.3) except the one in the formula for $L^A{}_B$. This is valid to leading order in $(H_0 R)^2$. We keep the extra terms in Eqs. (3.2.3) even though our formalism neglects other effects that also give fractional corrections of order $(H_0 R)^2$. The extra terms change σ_m by a few percent.

$$M^A{}_C = \delta^A{}_C + 2c^2\mathcal{P}(z)\begin{pmatrix} 1+\frac{R^2}{3c^2} & 2 \\ 2 & 1+\frac{R^2}{3c^2} \end{pmatrix}. \tag{3.28}$$

Here b is the impact parameter, $c = \sqrt{R^2 - b^2}$,

$$\mathcal{P}(z) = \frac{3}{2}H_0^2\Omega_M \frac{x(x_s - x)}{x_s}\frac{f(z)}{a_{\rm ex}(z)}, \tag{3.29}$$

and $f(z)$ is defined by Eq. (3.12). In these equations x and z are evaluated at the center of the void.

Our computational procedure can now be summarized as follows:

1. Pick some source redshift z_s, void radius R, and fraction of void mass on the shell today f_0.
2. Choose void locations according to the prescription described in Sec.3.2.2.
3. For each void, compute the 4×4 matrix that is formed by the matrices $\mathbf{J}, \mathbf{K}, \mathbf{L}$ and $\mathbf{M}$ from Eqs. (3.2.3).
4. Perform a similarity transformation $\mathbf{J} \to \mathbf{U}^{-1} \cdot \mathbf{J} \cdot \mathbf{U}$ on each of the matrices $\mathbf{J}, \mathbf{K}, \mathbf{L}, \mathbf{M}$ for some randomly chosen $SO(2)$ matrix $\mathbf{U}$, to randomize the direction of the vectorial impact parameter.
5. Multiply together all the 4×4 matrices, and multiply by the initial conditions (3.17), to evaluate $\mathcal{A}^A{}_B(x_s)$.
6. Compute the magnification μ relative to FRW from Eq. (3.18), and then distance modulus shift Δm from

$$\Delta m = -\frac{5}{2}\log_{10}(\mu) \tag{3.30}$$

$$= \frac{5}{2\ln 10}\ln|(1-\kappa)^2 - \gamma^2|. \tag{3.31}$$

7. Repeat steps 2 to 6 a large number of times to generate the distribution $p(\Delta m; z_s)$ of distance modulus shifts Δm for sources at redshift z_s, for a randomly chosen direction from the observer.

8. Finally, we correct this distribution to obtain the observationally relevant quantity, the probability distribution of magnitude shifts for a source chosen randomly on a sphere at a distance corresponding to redshift z_s. The corrected distribution is [65]

$$\begin{aligned} \mathcal{P}(\Delta m; z_s) &= \mathcal{N} p(\Delta m; z_s)/\mu \\ &= \mathcal{N} p(\Delta m; z_s) 10^{2\Delta m/5}, \end{aligned} \tag{3.32}$$

   where $\mathcal{N}$ is a normalization constant.

3.2.4 Relation to weak lensing theory

In weak lensing theory the matrix $\mathcal{A}(x_s)/x_s$ that describes the deflections of the rays is presumed to be always very close to the unit matrix, so the total integrated effect of the inhomogeneities on a given ray can be treated linearly. The solution to Eq. (3.16) in this approximation is given by Eq. (3.22) with $x_1 = 0$, $x_2 = x_s$,

$$\frac{\mathcal{A}^A{}_B(x_s)}{x_s} = \delta^A{}_B - \int_0^{x_s} dx \, \frac{x(x_s - x)}{x_s} \mathcal{R}^A{}_B(x). \tag{3.33}$$

Taking the determinant and linearizing again, the contribution from shear vanishes and the magnification is $\mu = 1 + 2\kappa$ where the lensing convergence κ is given by the standard formula

$$\kappa = \frac{3}{2} H_0^2 \Omega_M \int_0^{x_s} dx \frac{x\,(x_s - x)}{x_s a_{\rm ex}\,(z)} \delta_{\rm m}(x). \tag{3.34}$$

Here $\delta_{\rm m}(x)$ is the fractional over density, x is the comoving distance, x_s is comoving distance to the source, and $a_{\rm ex}(z)$ is the scale factor. Evaluating this for our void model gives

$$\kappa = \sum_i \kappa_i, \tag{3.35}$$

where the sum is over the voids and

$$\kappa_i = -3H_0^2\Omega_M \frac{x_i(x_s - x_i)}{x_s a_{\rm ex}(z_i)} f(z_i) c_i \left[1 - \frac{R^2}{3c_i^2}\right] \tag{3.36}$$

is the lensing convergence from the ith void. Here z_i and x_i are the redshift and comoving distance to the center of the ith void, $c_i = \sqrt{R^2 - b_i^2}$ and b_i is the ith impact parameter. Our model goes beyond the weak lensing result (3.35) as it includes lens-lens couplings and shear.

3.3 Approximate Analytical Computation of magnification dispersion

3.3.1 Overview

In the previous section, we described a Monte Carlo procedure for computing the probability distribution $\mathcal{P}(\Delta m; z_s)$ of magnitude shifts Δm for sources at redshift z_s, for our Swiss cheese model of voids. We will be particularly interested in the mean

$$\langle \Delta m \rangle = \int d\Delta m \, \Delta m \mathcal{P}(\Delta m; z_s) \tag{3.37}$$

and variance

$$\sigma_m^2 = \int d\Delta m \, (\Delta m - \langle \Delta m \rangle)^2 \, \mathcal{P}(\Delta m; z_s) \tag{3.38}$$

of this distribution. In subsequent sections of the chapter we will describe the results of our Monte Carlo simulations and their implications. In this section, however, we will take a detour and describe a simple, approximate, analytic computation of the variance. The approximation consists of using the weak lensing approximation to compute the total lensing convergence κ (accurate to a few percent, see Sec. 3.4.2), and then using an approximate cutoff procedure to incorporate the effect of the nonlinear relation (3.31) between κ and the magnitude shift Δm. We will see in Sec. 3.4 below that this analytic approximation agrees with our Monte Carlo simulations to within $\sim 30\%$.

Neglecting shear, the relation (3.31) reduces to

$$\Delta m = \frac{5}{\ln 10} \ln |1 - \kappa| \tag{3.39}$$

where κ is given by Eqs. (3.35) and (3.36). We will see shortly that the the variance of κ diverges. This divergence is an artifact of our use of a distributional density profile for each void, with a δ-function on the void's surface, and can be removed by endowing each shell with some small finite thickness Δr (see Sec. 3.3.4 below). The variance of Δm, on the other hand, is finite, because of the nonlinear relation (3.39). We shall proceed by using the linearized version

$$\Delta m = -\frac{5}{\ln 10} \left[\kappa + O(\kappa^2) \right] \tag{3.40}$$

of Eq. (3.39), and by simply cutting off the divergent integrals that arise, at $\kappa \sim 1$, the regime where the nonlinearity of the relation (3.39) becomes important.

3.3.2 Variance of magnitude shifts

From Eq. (3.40) we find for the mean and variance of the magnitude shift

$$\begin{aligned} \langle \Delta m \rangle &= -\frac{5}{\ln 10}\left[\langle \kappa \rangle + O(\kappa^2)\right], \\ \sigma_m^2 &= \left(\frac{5}{\ln 10}\right)^2 \left[\langle \kappa^2 \rangle - \langle \kappa \rangle^2 + O(\kappa^3)\right]. \end{aligned} \tag{3.41}$$

The averages are over the set of impact parameters $\{b_i : i \in [1, j(x_s)]\}$ in Eq. (3.36), where $j(x_s)$ is the number of voids out to the source at x_s. In computing the averages, it will prove convenient to define

$$q_i = 1 - b_i^2/R^2, \tag{3.42}$$

so that each q_i is distributed uniformly between zero and one, since impact parameters arbitrarily close to the void boundary are permitted. In fact, a shortcoming of our model is the vanishing thickness of the void wall. We therefore introduce lower cutoffs C_i for each void[4], that is, we restrict q_i to lie in the range $C_i \le q_i \le 1$. We will discuss below the origin and appropriate values of these cutoffs.

With this assumption we obtain for the mean of the lensing convergence (3.36) of the ith void

$$\begin{aligned} \langle \kappa_i \rangle &= -H_0^2 \Omega_M x_s R w_i \int_{C_i}^1 dq_i \left[3\sqrt{q_i} - \frac{1}{\sqrt{q_i}}\right] \\ &= -2H_0^2 \Omega_M x_s R w_i \sqrt{C_i}(1 - C_i) \end{aligned} \tag{3.43}$$

where

$$w_i = \frac{x_i(x_s - x_i) f(z_i)(1 + z_i)}{x_s^2}. \tag{3.44}$$

[4]These cutoffs will be used only for construction of our analytical model in this section; they are not used in Monte Carlo simulations in the remainder of the chapter.

The mean lensing convergence (4.56) is always negative, since $C_i < 1$; introducing the cutoff leads to a bias toward de-magnification. This is a shortcoming of the model, since for any mass-compensated perturbation $\langle \kappa_i \rangle = 0$ [5]. Below, we shall ignore small corrections that are powers of C_i, and will take $\langle \kappa_i \rangle = 0$ for all i.

By contrast the second moment $\langle \kappa_i^2 \rangle$ diverges logarithmically in the limit $C_i \to 0$:

$$\langle \kappa_i^2 \rangle = \left(H_0^2 \Omega_M x_s R w_i \right)^2 \int_{C_i}^1 dq_i \left(3\sqrt{q_i} - \frac{1}{\sqrt{q_i}} \right)^2 \tag{3.45}$$

$$= \left(H_0^2 \Omega_M x_s R w_i \right)^2 \left[-\ln C_i - \frac{3}{2} + O(C_i) \right]. \tag{3.46}$$

This divergence is caused by rays that just graze the δ function shell of the void.

Because κ is a sum of κ_i, its mean is the sum of the individual means, but

$$\langle \kappa^2 \rangle = \sum_i \langle \kappa_i^2 \rangle - \sum_{i \neq j} \langle \kappa_i \rangle \langle \kappa_j \rangle \tag{3.47}$$

and therefore

$$\sigma_\kappa^2 = \langle \kappa^2 \rangle - \langle \kappa \rangle^2 = \sum_i (\langle \kappa_i^2 \rangle - \langle \kappa_i \rangle^2) \, . \tag{3.48}$$

Combining this with Eqs. (3.40) and (3.46) and dropping terms linear in C_i gives for the variance in magnitude shift

$$\sigma_m^2 = \sigma_0^2 \sum_i w_i^2 \left(-\ln C_i - \frac{3}{2} \right), \tag{3.49}$$

where we have defined

$$\sigma_0 = \frac{5 H_0^2 \Omega_M x_s R}{\ln 10}. \tag{3.50}$$

[5] To restore this feature we could either scale the contribution from the underdense core downward by a factor of $S_i = 1 + \sqrt{C_i} + C_i$ or scale the contribution from the overdense shell upward by the same factor S_i.

We choose the cutoffs C_i to correspond to $\kappa_i \sim 1$, as discussed above; from Eqs. (3.36) and (3.44) this gives

$$C_i = (H_0^2 \Omega_M R x_s w_i)^2. \tag{3.51}$$

The approximate analytic result given by Eqs. (3.44) and (3.49) – (3.51) is plotted in Fig. 3.10 in Sec. 3.4.2 below. It agrees with our Monte Carlo simulations to within $\sim 30\%$, which is reasonable given the crudeness of our analytic cutoff procedure.

3.3.3 Finite sampling effects

In addition to computing the width σ_m^2 of the distribution of magnitude shifts Δm, we now compute a different quantity $\sigma_{m,\mathrm{med}}^2(N)$ which is, roughly speaking, the estimate of the width that one would obtain with N samples Δm_α, $1 \leq \alpha \neq N$, drawn from the distribution. More precisely, this quantity is defined as follows. From the N samples we construct the estimator

$$\hat{\sigma}_m^2 \equiv \frac{1}{N-1} \sum_{\alpha=1}^{N} \Delta m_\alpha^2 - \frac{1}{N(N-1)} \left(\sum_{\alpha=1}^{N} \Delta m_\alpha \right)^2. \tag{3.52}$$

This quantity is itself a random variable with expected value $\left\langle \hat{\sigma}_m^2 \right\rangle = \sigma_m^2$. However for finite N the median value of the distribution of $\hat{\sigma}_m^2$ can be significantly different from σ_m^2. We denote this median value by $\sigma_{m,\mathrm{med}}^2(N)$. In the limit $N \to \infty$ we have $\sigma_{m,\mathrm{med}}(N) \to \sigma_m$. We note that realistic supernovae surveys will have no more than $\sim 10^4$ supernovae.

To estimate this median value, we use the fact that for each void i, finite sampling imposes a minimum value on q_i of $q_i \sim 1/N$ on average, which acts like a statistical cutoff in the integral (3.46). This is in addition to the physical

cutoff (3.51) discussed above, which we will denote by $q_{i,c}$ from now on. For N samples $q_{i,\alpha}$, $1 \leq \alpha \leq N$, the probability that all N samples are larger than a value C_i which is larger than $q_{i,c}$ is

$$P_0(< C_i) = \left(\frac{1 - C_i}{1 - q_{i,c}}\right)^N . \tag{3.53}$$

Differentiating once we find that the probability distribution of C_i is

$$P(C_i) = \left|\frac{dP_0(< C_i)}{dC_i}\right| = \frac{N(1 - C_i)^{N-1}}{(1 - q_{i,c})^N} . \tag{3.54}$$

For very large values of N and small $q_{i,c}$ an adequate approximation is

$$P(C_i) \approx N \exp[-N(C_i - q_{i,c})], \tag{3.55}$$

which is properly normalized for $C_i \geq q_{i,c}$ if we extend the range of C_i to infinity, thereby incurring an error $\sim \exp(-N)$.

We now average the expression (3.49) for the width σ_m^2, using the distribution (3.55) to average over the cutoffs C_i. The result is

$$\begin{aligned} \sigma^2_{m,\mathrm{med}} &\approx \sigma_0^2 \sum_i w_i^2 \\ &\quad \times \left[\ln N - \frac{3}{2} - \int_0^\infty dx e^{-x} \ln(x + Nq_{i,c})\right]. \end{aligned} \tag{3.56}$$

If we define

$$\begin{aligned} S(f_0, z_s) &= \sum_i w_i^2, \\ \gamma(Nq_{i,c}) &= -\int_0^\infty dx e^{-x} \ln(x + Nq_{i,c}), \end{aligned} \tag{3.57}$$

then Eq. (3.56) becomes

$$\sigma^2_{m,\mathrm{med}} \approx \sigma_0^2 \left[S(f_0, z_s)\left(\ln N - \frac{3}{2}\right) + \sum_i w_i^2 \gamma(Nq_{i,c})\right]. \tag{3.58}$$

The result (3.58) was obtained by averaging over the cutoffs $\{C_i\}$ using the probability distribution (3.55), and is an estimate of the median of the distribution of $\hat{\sigma}_m^2$. Of course the actual value of $\hat{\sigma}_m^2$ computed from a Monte Carlo realization of N lines of sight, or obtained from N observations of magnifications, may differ from the result (3.58). We would like to also estimate the spread in values of $\hat{\sigma}_m^2$. From Eq. (3.49), and taking the variance with respect to the distribution of cutoffs C_i, we find

$$\left(\frac{\Delta\sigma^2_{m,\rm med}}{\sigma^2_{m,\rm med}}\right)^2 = \frac{\sum_i w_i^4 {\rm Var}(Nq_{i,c})}{\left[\sum_i w_i^2(\overline{\ln C_i} + 3/2)\right]^2}, \tag{3.59}$$

where

$$\begin{aligned} {\rm Var}(Nq_{i,c}) &= \overline{(\ln C_i)^2} - \left(\overline{\ln C_i}\right)^2 \\ &= \int_0^\infty dx e^{-x} [\ln(x + Nq_{i,c})]^2 - [\gamma(Nq_{i,c})]^2 \end{aligned} \tag{3.60}$$

Here the overbars denote an expectation value with respect to the probability distribution (3.55). The quantity (3.59) is a measure in the fractional spread in our estimate of the median, and should give a lower bound on the fractional spread in values of $\hat{\sigma}_m^2$.

Two limits of Eqs. (3.58) and (3.59) are especially simple. First, for $Nq_{i,c} \ll 1$, we have $\gamma(Nq_{i,c}) \approx \gamma_E = 0.5772\ldots$, the Euler-Mascheroni constant, and also ${\rm Var}(Nq_{i,c}) \approx 1.645$ and $-\overline{\ln C_i} \approx \ln N + \gamma_E$. This gives

$$\sigma^2_{m,\rm med} \approx \sigma_0^2 S(f_0, z_s)\left(\ln N - \frac{3}{2} + \gamma_E\right), \tag{3.61}$$

$$\frac{\Delta\sigma^2_{m,\rm med}}{\sigma^2_{m,\rm med}} \approx \sqrt{\frac{1.645}{N_{\rm void}(\ln N + \gamma_E - 3/2)}}, \tag{3.62}$$

where $N_{\rm void} = x_s/(2R)$ is the number of voids and we have used the crude approximation w_i = constant in the second equation. Second, for $Nq_{i,c} \gg 1$, we

have $\gamma(Nq_{i,c}) \approx -\ln Nq_{i,c}$, $\mathrm{Var}(Nq_{i,c}) \approx 1/(Nq_{i,c})^2$, and $\overline{\ln C_i} \approx \ln q_{i,c}$, and so we obtain

$$\sigma^2_{m,\mathrm{med}} \approx \sigma_0^2 \left[-\frac{3}{2} S(f_0, z_s) - \sum_i w_i^2 \ln q_{i,c} \right] \tag{3.63}$$

$$\frac{\Delta\sigma^2_{m,\mathrm{med}}}{\sigma^2_{m,\mathrm{med}}} \propto \frac{1}{N}. \tag{3.64}$$

The second case (3.63) coincides with the N-independent width (3.49) – (3.51) computed earlier. We see that the results are dictated by a competition between statistical and physical cutoffs via the dimensionless parameter $Nq_{i,c}$.

As discussed above, our simulations are effectively cut off at $\kappa_i \sim 1$; this implies a physical cutoff

$$\begin{aligned} q_{i,c} &\sim (H_0^2 \Omega_M R x_s w_i)^2 \\ &\approx 2.2 \times 10^{-7} \left(\frac{H_0 \Omega_M x_s}{0.23} \right)^2 \left(\frac{h_{0.7} R}{35\mathrm{Mpc}} \right)^2 (4w_i)^2. \end{aligned} \tag{3.65}$$

Here we have scaled the factor $\Omega_M H_0 x_s$ to its value at $\Omega_M = 0.3$, $z_s = 1.0$, the quantity $h_{0.7}$ is given by $H_0 = 70 h_{0.7}\,\mathrm{km\,s^{-1}Mpc^{-1}}$, and we note that $4w_i \leq f(z_i)(1 + z_i)$. From the estimate (3.65) we expect the $Nq_{i,c} \ll 1$ limit to apply for $N \lesssim 10^6$. In this case the cutoff is purely statistical and the physical cutoff is unimportant. The prediction (3.61) for $\sigma_{m,\mathrm{med}}$ for $N = 10^4$ and $z_s = 1$ is shown in Fig. 3.1, together with results from our Monte Carlo simulations, which are described in Sec. 3.4 below. The plot shows good agreement between the model and the simulations.

For this case, a lower bound on the fractional spread in the values of $\hat{\sigma}^2_m$ around its median value is given by Eq. (3.62). That is, in any given simulation or observational survey with N light sources, the scatter of values about the expected will be at least this large. For example, with $N = 10^4$, $z_s = 1$ and $R = 35$

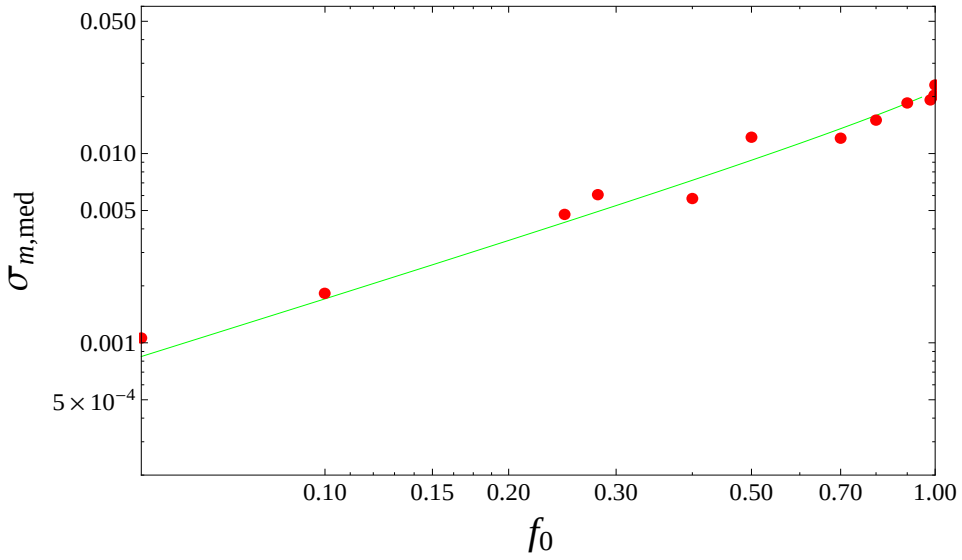

Figure 3.1: The green line is our analytic model (3.61) of the median width of the distribution of magnitude shifts Δm, for $N = 10^4$ samples, source redshift $z_s = 1.0$ and void radius $R = 35$ Mpc, as a function of the fraction of mass f_0 on the void shells today. The data points are from our Monte Carlo simulations with the same parameter values, described in Sec. 3.4 below.

Mpc, the implied spread is 6%. In this regime where the cutoff is primarily statistical, the range of likely values of $\hat{\sigma}_m$ is substantial, and only decreases logarithmically with increasing N.

When $N \gtrsim 10^6$, we move into the $Nq_{i,c} \gg 1$ regime where Eqs. (3.3.3) apply. The results in this regime were discussed in Sec. 3.3.2 above, and are plotted in Fig. 3.10 in Sec. 3.4.2 below. Equation (3.64) indicates that the spread scales as $1/N$ in this regime. However this estimate is only a lower bound for the spread in values of $\hat{\sigma}_m^2$, as discussed above. In fact, from Eq. (3.52) the standard deviation of $\hat{\sigma}_m^2$ can be computed in terms of N and of the second and fourth moments of Δm; it scales like $1/\sqrt{N}$ as $N \to \infty$. In any case, the spread decreases more rapidly as N increases after the transition to the large N regime. We will

see in Sec. 3.4 below that this prediction agrees well with our Monte Carlo simulations.

3.3.4 Extension of void model to incorporate finite shell thickness

In this subsection we consider a modification of our void model, in which the void wall is given a finite comoving thickness Δr_i that acts as a physical cutoff in the divergent integral (3.45). The corresponding value of the cutoff parameter $q_{i,c}$ is $q_{i,c} = 2\Delta r_i/R$, from Eq. (3.42). The value of wall thickness that corresponds to the cutoff (3.65) is thus $\Delta r_i \sim 3\,\mathrm{pc}(R/35\,\mathrm{Mpc})^3$, which is much smaller than the expected void wall thicknesses $\sim$ Mpc in large scale structure. Thus, our thin-shell void model is somewhat unrealistic; the results are modified (albeit only logarithmically) once the wall thickness exceeds $\sim$ pc scales. This motivates modifying the model to incorporate a finite wall thickness.

Consider next how the wall thickness evolves with redshift. At very early times, when the perturbation is in the linear regime, it maintains its shape in comoving coordinates, so the cutoff scale is some fixed fraction of R. Once the perturbation becomes nonlinear, the shell thickness should freeze out in physical extent, implying a comoving size $\propto 1/a$. Thus, a suitable model for the redshift dependence of the cutoff would be

$$q_c(a) = \epsilon_0 W(a/a_0), \tag{3.66}$$

where $W(x)$ is a function with $W(x) \to 1$ for $x \ll 1$ and $W(x) \to K_0/x$ for $x \gg 1$. Here $a_0(f_0)$ is the scale factor when the perturbation ceases to be linear, and

K and ϵ_0 are constants that may also depend on f_0. Very roughly, we expect $q_c(a) \sim 0.1$ so $Nq_{i,c} \gg 1$ as long as $N \gtrsim 10$, so that Eq. (3.3.3) will apply.

Suppose now that for a restricted range of source redshifts it suffices to take the fractional shell wall thickness $\epsilon_s = \Delta r_i/R$ in comoving coordinates to be the same for all shells. Then from Eq. (3.49) we get[6]

$$\sigma_m^2 = \sigma_0^2 S(f_0, z_s)\left[-\ln\epsilon_s + \ln(2) + O(\epsilon_s \ln\epsilon_s)\right]. \tag{3.68}$$

Equation (3.68) has the same form as Eq. (3.61), but since $N\epsilon_s \gg 1$, the implied σ_m is smaller. For example, evaluating this expression for $f_0 = 0.9$, $z_s = 1.0$ and $R = 35$ Mpc gives

$$\sigma_m \approx 0.013\sqrt{1 + 0.23\ln\left(\frac{1\,\mathrm{Mpc}}{\Delta r}\right)}. \tag{3.69}$$

where $\Delta r = \epsilon_s R$ is the wall thickness.

The logarithmic divergence of σ_m^2 will also be regulated by treating the shell as composed of fragments that represent local density enhancements such as galaxy clusters and superclusters for purposes of computing the magnification of passing light beams. We shall examine this further refinement of our model elsewhere.

[6]Eq. (3.68) differs from Eq. (3.49) in that the $-3/2$ has been replaced by $\ln 2$. This slightly more accurate version of the equation is derived as follows. Instead of using the cutoff procedure embodied in Eq. (3.45), we use a regulated density profile of the form $\delta_{\rm m}(r) = -f\Theta(R_1 - r) + \alpha\Theta(R - r)\Theta(r - R_1)$ where $R_1 = R(1 - \epsilon_s)$ and $\alpha = f[(1 - \epsilon_s)^{-3} - 1]^{-1}$. The variance in the lensing convergence can then be computed from

$$\begin{aligned}\left\langle\kappa_i^2\right\rangle &= 9H_0^4\Omega_M^2\frac{x_i^2(x_s - x_i)^2}{x_s^2 a_{\rm ex}(x_i)^2R^2}\int_0^R dr\int_0^R d\bar{r}\,\delta_{\rm m}(r)\delta_{\rm m}(\bar{r}) \\ &\quad\times r\bar{r}\ln\left|\frac{r+\bar{r}}{r-\bar{r}}\right|,\end{aligned} \tag{3.67}$$

from Eq. (3.34).

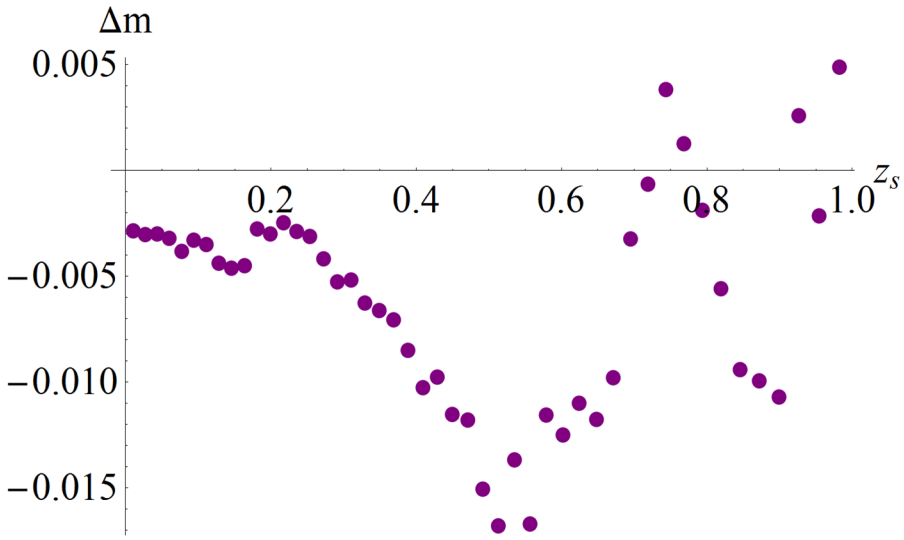

Figure 3.2: The magnitude shift Δm as a function of source redshift z_s for a single run, for voids of radius $R = 35$ Mpc, fraction of mass on the shell today $f_0 = 0.9$, in a ΛCDM cosmology with $\Omega_M = 0.3$.

3.4 Results of Monte Carlo Simulations for Magnification Distributions

We now turn to describing the results of our Monte Carlo simulations based on the algorithm described in Sec. 3.2. In the remainder of this chapter, unless otherwise specified, we will adopt the fiducial parameter values of matter fraction $\Omega_M = 0.3$, source redshift $z_s = 1.0$, void size $R = 35$ Mpc, and fraction of void mass on shell today $f_0 = 0.9$. Our choice of void size is motivated by the fact that observed void sizes [98, 99, 100, 101, 102, 103, 104, 105, 106] range from a typical size of ~ 10 Mpc to an upper limit of ~ 100 Mpc. For this fiducial case, we show in Fig. 3.2 the distance modulus shift Δm as a function of redshift z_s for a single realization of the void distribution. The values jump discontinuously after each void, and illustrate the stochastic nature of the lensing process.

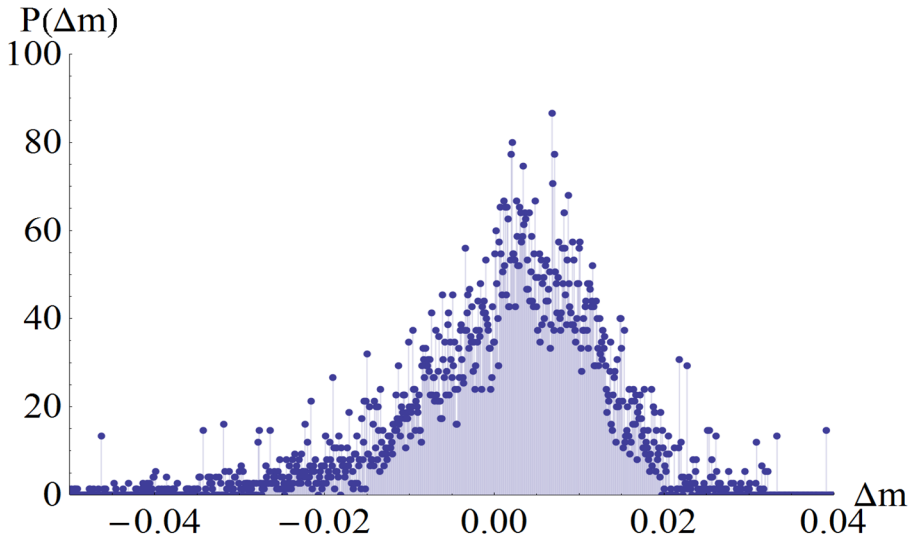

Figure 3.3: The probability distribution of magnitude shifts Δm for a simulation in a ΛCDM cosmology with $\Omega_M = 0.3$, with sources at redshift $z_s = 1$, comoving voids radius $R = 35$ Mpc, and fraction of void mass on the shell today $f_0 = 0.9$.

Next, we repeat this computation some large number N of times in order to generate the distribution of modulus shifts Δm. In the rest of the chapter we will focus in particular on the mean $\langle \Delta m \rangle$ and standard deviation σ_m of this distribution, and also on the estimator $\hat{\sigma}_m(N)$ of the standard deviation that one obtains at finite N, given by Eq. (3.52), which satisfies $\hat{\sigma}_m(N) \to \sigma_m$ as $N \to \infty$.

The distribution for the fiducial case for $N = 2 \times 10^6$ is shown in Fig. 3.3. For this case the standard deviation is $\sigma_m = 0.03135 \pm 0.0003$ and the mean is $\langle \Delta m \rangle = 0.004 \pm 0.001$ (where the error is estimated based on dividing the data into 200 groups of 10000 runs). Our result for the standard deviation agrees to within $\sim 30\%$ with that of a different Swiss cheese void model by Brouzakis, Tetradis and Tzavara [92]; see Fig. 5 of that paper which applies to $R = 40$ Mpc voids at $z_s = 1$. It also agrees to within a factor ~ 2 with the predictions of weak

lensing theory using an approximate power spectrum for our void model, as discussed in Appendix 3.7.

Figure 3.4 shows how our estimated standard deviation $\hat{\sigma}_m(N)$ varies with number of runs N. The quantity plotted is $\log_{10}|\hat{\sigma}_m/\sigma_m - 1|$, where $\sigma_m = 0.03135$ is an estimate of the $N \to \infty$ limit, here taken from our largest run with $N = 10^6$. This plot exhibits several interesting features that are in good agreement with the analytical model described in Sec. 3.3. First, in the low N regime at say $N \sim 10^4$, the values of $\hat{\sigma}_m(N)$ differ systematically from the asymptotic value by a few tens of percent, reflecting the difference between $\sigma_{m,\mathrm{med}}$ and σ_m. Second, there is a somewhat smaller scatter in this regime, of $\sim 5\%$, in agreement with the prediction (3.62). Third, there is a transition to a different behavior at $N \sim 3\times10^5$, after which both the scatter and systematic deviation from the asymptotic value are much smaller.

In the rest of this chapter, we will use the value $N = 10^6$ unless otherwise specified. From Fig. 3.4 this corresponds to an accuracy of ~ 1 percent.

We show in Fig. 3.5 the mean $\langle \Delta m \rangle$ of the distribution as a function of source redshift z_s, for $R = 35$ Mpc and $N = 2 \times 10^6$. The errors shown are estimated by dividing the data into 200 groups of 10000 runs. The effect of the nonzero mean on cosmological studies cannot be reduced by using a large number of supernovae, unlike the effect of the dispersion σ_m. However, the mean $\langle \Delta m \rangle \sim 0.003$ magnitudes shown in Fig. 3.5 is too small to impact cosmological studies in the foreseeable future.

In Figs. 3.6, 3.7, and 3.8 we show the probability distributions of magnitude shifts Δm for some other cases: source redshifts of $z_s = 1.1, 1.6$ and 2.1, and void

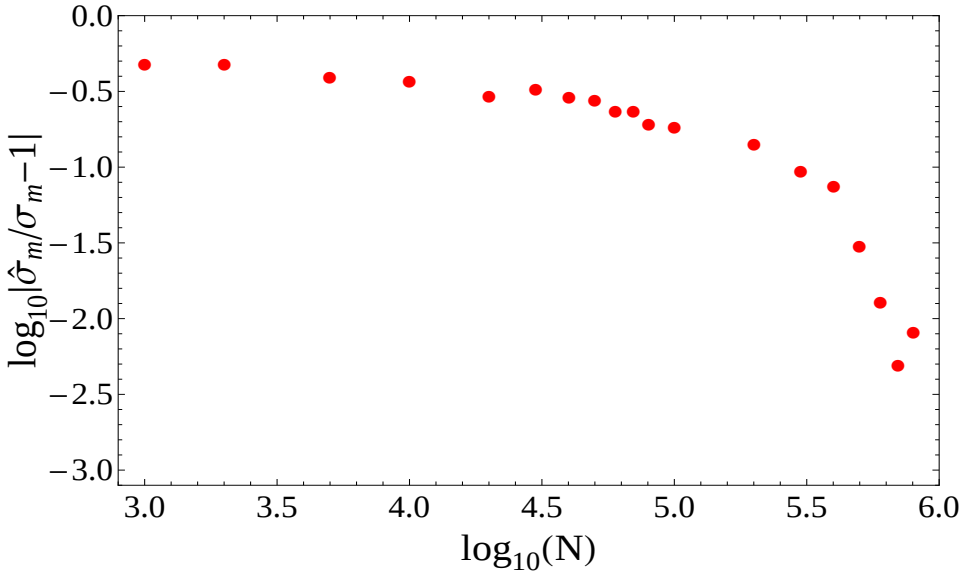

Figure 3.4: The estimator $\hat{\sigma}_m$ of the standard deviation of the distribution of magnitude shifts Δm, as a function of number N of runs, for sources at redshift $z_s = 1$, comoving voids radius $R = 35$ Mpc, and fraction of void mass on the shell today $f_0 = 0.9$. The plotted quantity is $\log_{10}|\hat{\sigma}_m/\sigma_m - 1|$, where $\sigma_m = 0.03135$ is an estimate of the $N \to \infty$ limit, here taken from our largest run with $N = 10^6$.

radii of $R = 35$ Mpc, 100 Mpc, and 350 Mpc. We now turn to a discussion of the dependence of our results on these parameters, as well as on the fraction of mass in the shell today f_0.

3.4.1 Dependence on void size

In Fig. 3.9 we show the standard deviation σ_m of the magnitude shift as a function of void size R, for three different redshifts, $z_s = 1.1, 1.6, 2.1$. To a good approximation the standard deviation grows as the square root of the void size, $\sigma_m \propto \sqrt{R}$. We can understand this scaling by making some order of magnitude

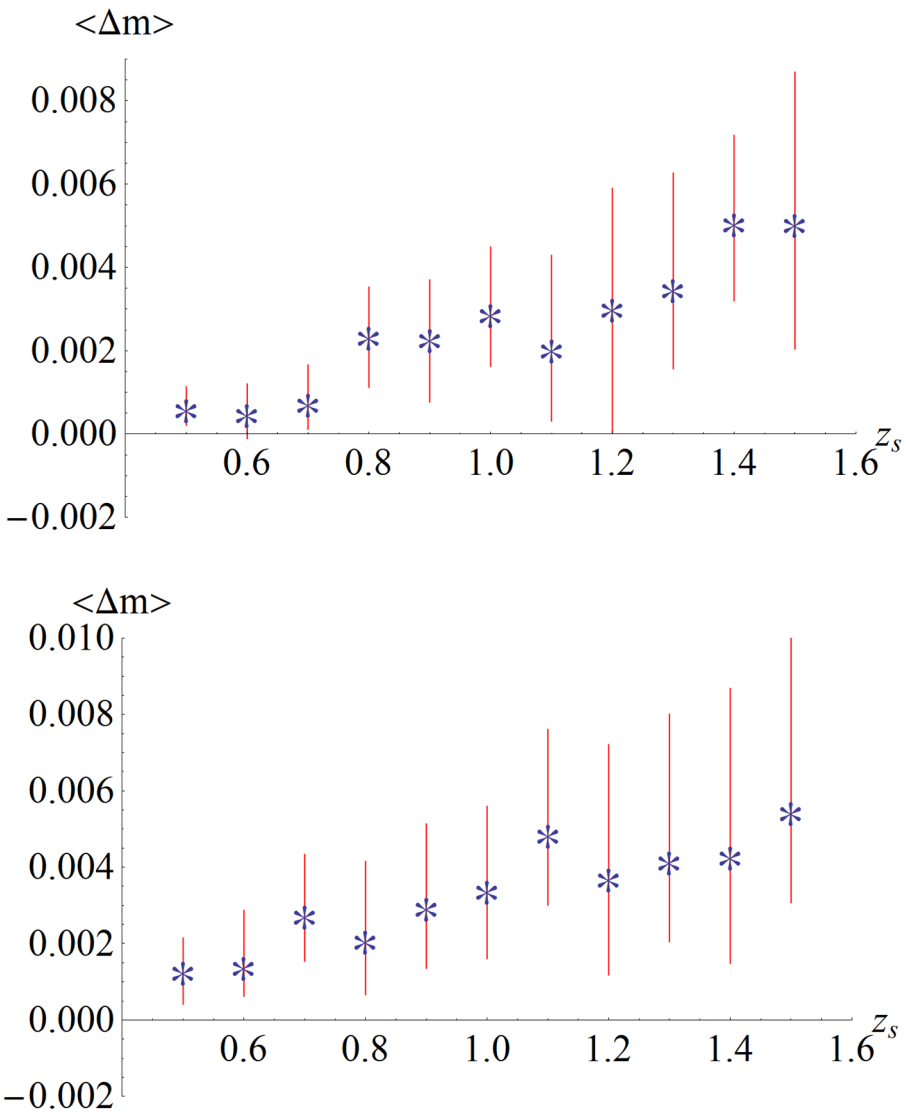

Figure 3.5: [Top] The mean $\langle \Delta m \rangle$ of the distribution of magnitude shifts Δm as a function of source redshift z_s, for voids of radius $R = 35$ Mpc with fraction of mass on the shell today $f_0 = 0.9$, for $N = 10^6$ samples. [Bottom] The same for $R = 100$ Mpc.

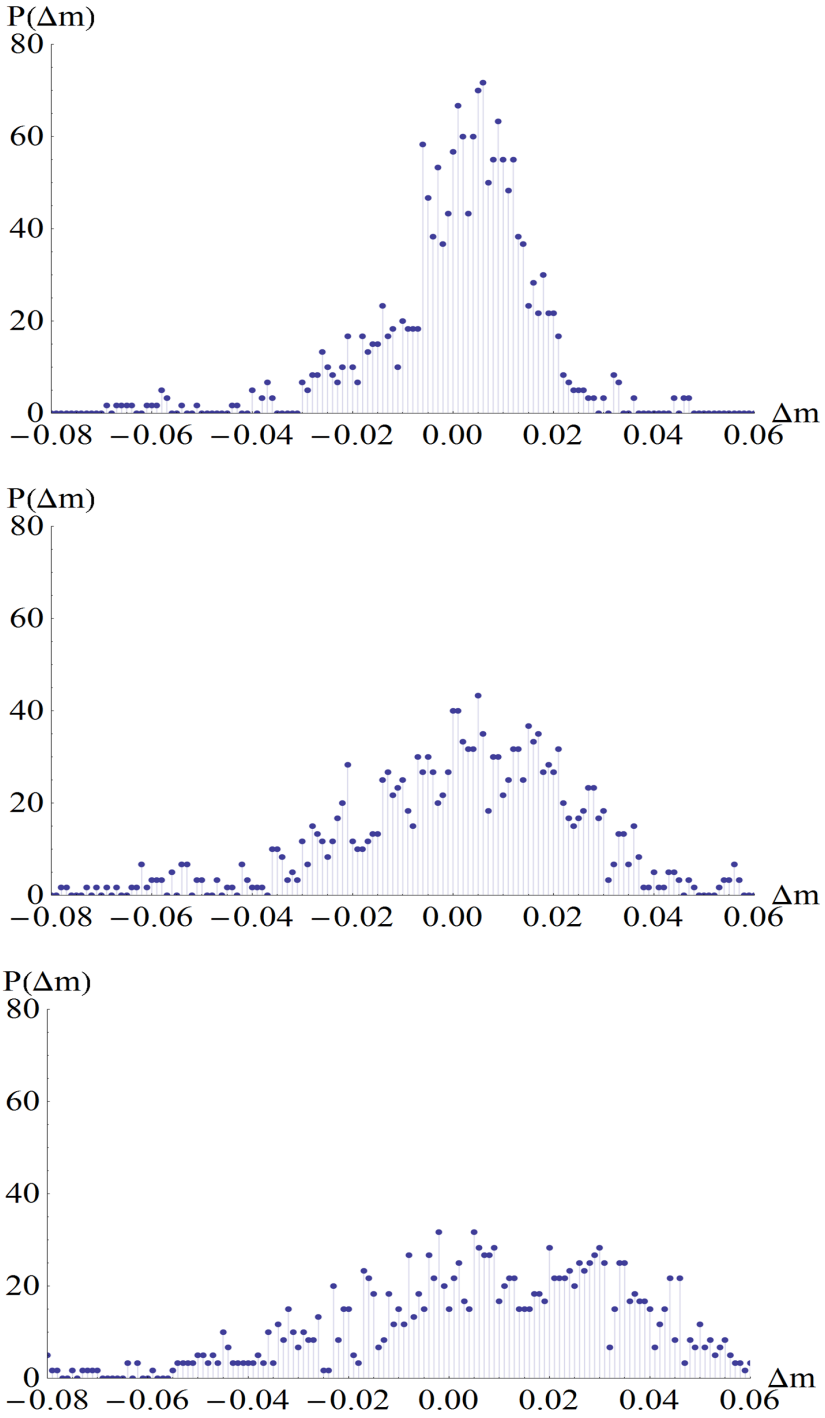

Figure 3.6: The probability distributions of magnitude shifts Δm for simulations with sources at redshifts of $z_s = 1.1$ (top), $z_s = 1.6$ (middle) and $z_s = 2.1$ (bottom), for comoving voids of radius R =35 Mpc with 90% of the void mass on the shell today.

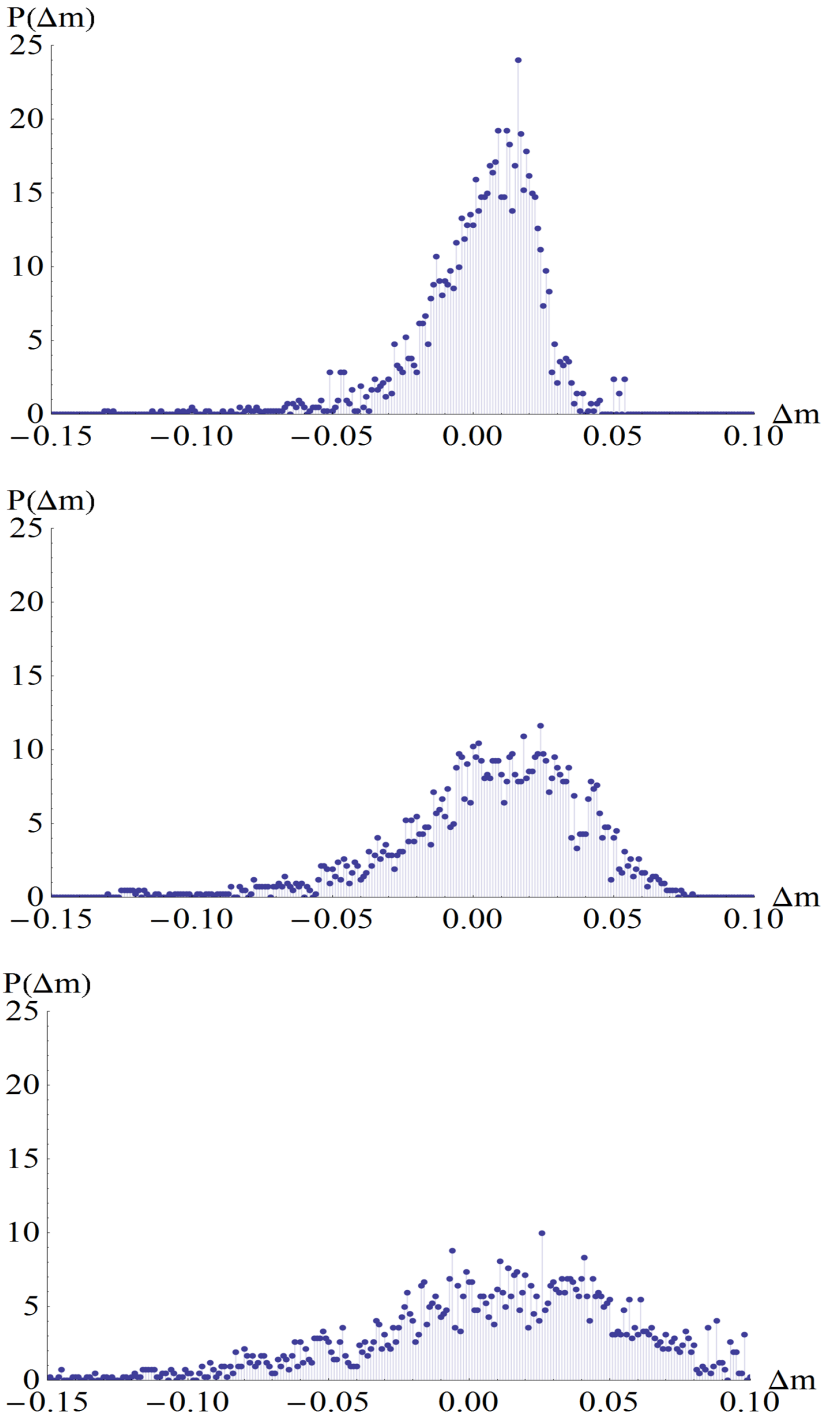

Figure 3.7: The probability distributions of magnitude shifts Δm, at source redshifts z_s of 1.1 (top), 1.6 (middle) and 2.1 (bottom), as in Fig. 3.6 except with comoving void radius of R = 100 Mpc.

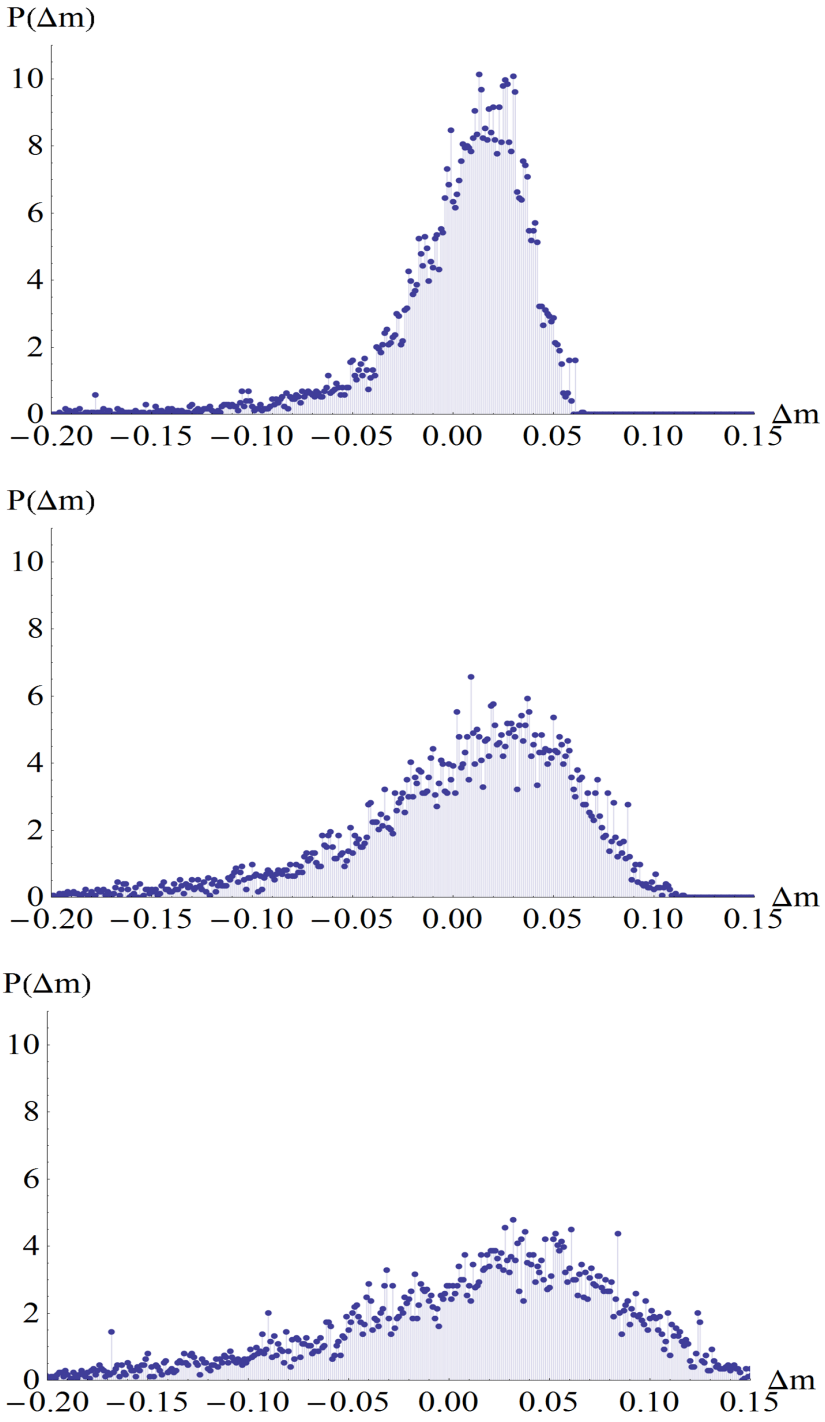

Figure 3.8: The probability distributions of magnitude shifts Δm, at source redshifts z_s of 1.1 (top), 1.6 (middle) and 2.1 (bottom), as in Fig. 3.6 except with comoving void radius of R = 350 Mpc.

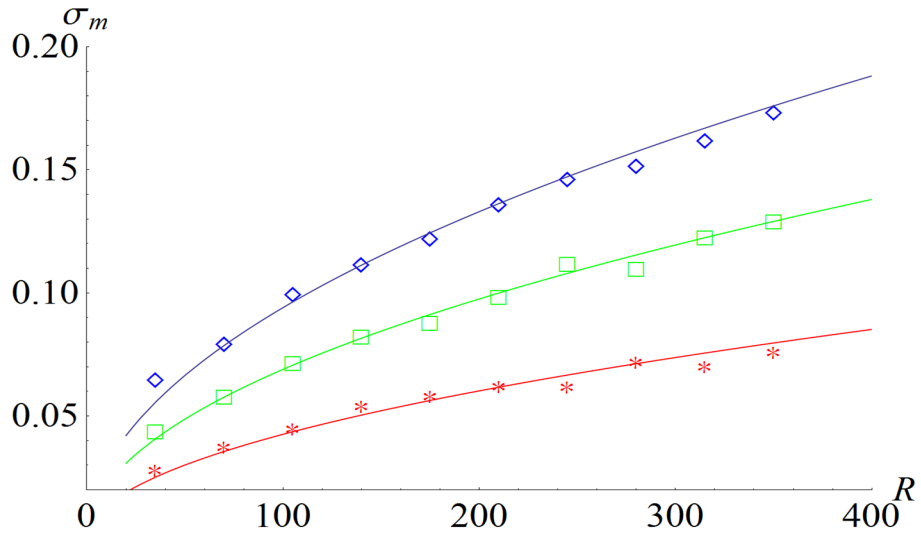

Figure 3.9: The standard deviation σ_m of the distribution of distance modulus shifts Δm as a function of void radius R, computed using $N = 10^6$ runs for each point. The bottom line (stars) is for sources at $z_s = 1.1$, the middle line (squares) is $z_s = 1.6$, and the top line (diamonds) is $z_s = 2.1$. Void radii range from 35 to 350 Mpc and the fraction of void mass on the shell today is $f_0 = 0.9$. The lines are fits of the form $\sigma_m \propto \sqrt{R}$.

estimates.

In making these estimates, we consider two different classes of rays. Consider first rays that never come very close to the shell of any of the voids, i.e. we exclude the case $b - R \ll R$, where b is the impact parameter. The potential perturbation $\Delta\phi$ for passage through a void is of order $\Delta\phi \sim fR^2H_0^2$, where f is the fraction of void mass in the shell (or equivalently the fractional density perturbation in the void interior). The contribution to the lensing convergence from this void is then of order $\kappa \sim \Delta\phi/(H_0R) \sim fH_0R$. Next, the trajectory of rays is a random walk, so the net lensing convergence is the rms convergence for a single void multiplied by the square root of the number $\sim 1/(H_0R)$ of voids.

Thus the contribution to the rms magnitude shift from this class of rays is of order

$$\sigma_m \sim f\sqrt{H_0 R}. \tag{3.70}$$

Consider next rays which just graze the shell of at least one of the voids. These grazing rays are subject to large deflections, because of the δ-function in density on the surface of the void. The large deflections cause cause the second moment $\left\langle \kappa^2 \right\rangle$ of the lensing convergence to diverge, as discussed in Sec. 3.3.2. However, the standard deviation of the magnitude shift Δm is still finite, because of the logarithmic relation (3.39) between Δm and κ.

For estimating the effect of these grazing rays, we neglect shear. The convergence κ of the grazed void will be of order unity or larger if the impact parameter b is $b = R(1-\varepsilon)$, where $\varepsilon \sim f^2 R^2 H_0^2$, from Eq. (3.36). This will occur with probability $\sim \varepsilon$. The contribution of these rays to $\left\langle (\Delta m)^2 \right\rangle \propto \left\langle [\ln(1-\kappa)]^2 \right\rangle$ will be of order ε times the number $\sim 1/(H_0 R)$ of voids, or $\sigma_m \sim f\sqrt{H_0 R}$, the same as the result (3.70) for the non-grazing rays.

These considerations show that both the underdense void and the mass-compensating shell make substantial, comparably large contributions to σ_m. This suggests that it may be important to refine the shell model to include its fragmentation into localized overdensities representing galaxy clusters and galaxies, as discussed in Sec. 3.3.4 above.

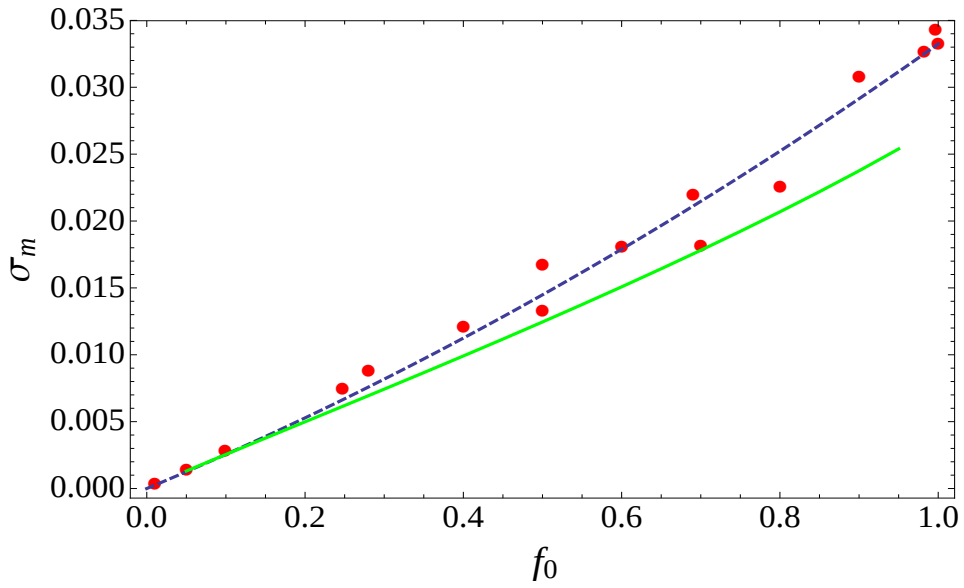

Figure 3.10: The standard deviation σ_m as a function of the fraction f_0 of the void mass on the shell today, for void radii of $R = 35$ Mpc and source redshift of $z_s = 1$, computed using $N = 10^6$ runs for each point. The dashed blue curve is a fit of the form $\sigma_m = \alpha f_0 + \beta f_0^2$. This plot shows that there are nonlinearities present at the level of $\sim 30 - 40\%$. The solid green curve is the analytic model (3.49) – (3.51), which is accurate to $\sim 30\%$.

3.4.2 Dependence on fraction of void mass on the shell

In this subsection we discuss the dependence of the magnification distribution on the fraction f_0 of void mass on the shell today, or, equivalently, on the fractional overdensity $\delta\rho/\rho$, cf. Eq. (3.6) above. Figure 3.10 shows the results of our simulations for σ_m as a function of f_0 for $N = 10^6$, together with a fit of the form (3.71)

$$\sigma_m(f_0) = \alpha f_0 + \beta f_0^2 \tag{3.71}$$

for some constants α and β. We find that $\alpha = 0.025 \pm 0.006$ and $\beta = 0.0085 \pm 0.0064$. Thus, the data show a statistically significant deviation from linear behavior, of the order of $\sim 30 - 40\%$.

We now discuss the various sources of nonlinearity that arise in the computation. We will consider three different types of effects.

First, in weak lensing theory, the magnification is a linear function of the density perturbation. Our computation includes some nonlinear effects that go beyond weak lensing theory, specifically lens-lens coupling (the fact that the deflection due to one lens modifies the deflection caused by subsequent lenses) and shear (the effect of the non-trace components of the matrices $\mathcal{R}^A{}_B$ and $\mathcal{A}^A{}_B$). To explore the magnitude of these effects, we performed Monte Carlo simulations where we compute the lensing convergence for each void and add these to obtain the total lensing convergence (3.35), and then compute Δm from κ using the exact nonlinear relation (3.31) for zero shear. The resulting value of σ_m for $f_0 = 0.9$, $z_s = 1$, $R = 35$ Mpc, $N = 10^6$ is $\sigma_m = 0.0292$, about 7% smaller than the value $\sigma_m = 0.0314$ obtained by multiplying the 4×4 matrices. Thus, there is a $\sim 7\%$ change from lens-lens coupling and shear. For $R = 100$ Mpc, the change due to lens-lens coupling and shear is $\sim 10\%$. We also performed simulations where we kept just the trace part of the matrix $\mathcal{R}_{AB}$, in order to exclude the effects of shear, but included lens-lens couplings by computing 4×4 matrices for each void and multiplying all these matrices. In this case the deviations of σ_m from the full simulations are $\sim 3\%$ for $f_0 = 0.9$, $z_s = 1$, $R = 35$ Mpc and $\sim 6\%$ for $R = 100$ Mpc. Thus, corrections due to shear are of this order.

These nonlinearities due to lens-lens coupling and shear are significantly smaller than the nonlinearity shown in Fig. 3.10. Thus other sources of nonlinearity must dominate. For the remainder of this subsection we will neglect lens-lens coupling and shear, to simplify the discussion.

A second type of nonlinearity present in our computations is the fact that the

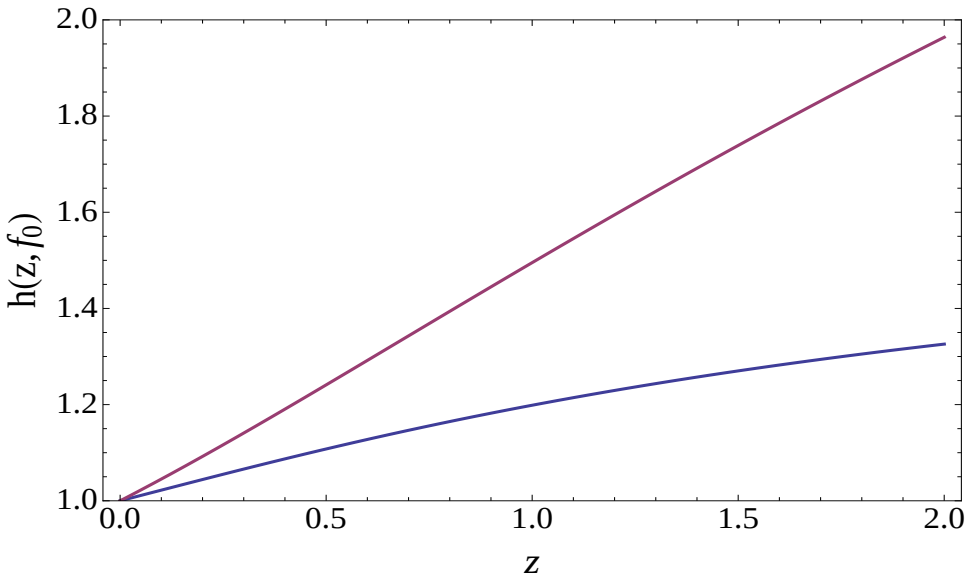

Figure 3.11: The factor $h(z, f_0)$ by which nonlinear evolution corrects the growth function $D_+(z)$ of linear perturbation theory, for our void model. The upper curve is for $f_0 = 0.9$ and the lower curve is for $f_0 = 0.5$.

void mass fraction $f(z)$ at some redshift z depends nonlinearly on its value $f_0 = f(0)$ today, due to nonlinearity in the void evolution. Therefore, even if we make the weak-lensing approximation of a linear dependence of the magnification on the density perturbation $f(z)$, the magnification will still be a nonlinear function of f_0. We can parameterize this nonlinear evolution effect by writing

$$f(z; f_0) = f_0 D_+(z) h(z, f_0), \tag{3.72}$$

where $D_+(z)$ is the growth function of linear perturbation theory, normalized so that $D_+(0) = 1$, and the function $h(z, f_0)$ incorporates the nonlinearity. This function satisfies $h(z, f_0) \to 1$ as $f_0 \to 0$ and also as $z \to 0$, and can be computed using the results of Sec. 3.2.1 above. Figure 3.11 plots this function for $f_0 = 0.5$ and $f_0 = 0.9$, and shows that the nonlinearities in the evolution are significant.

This nonlinear evolution effect is the dominant source of nonlinearity in our

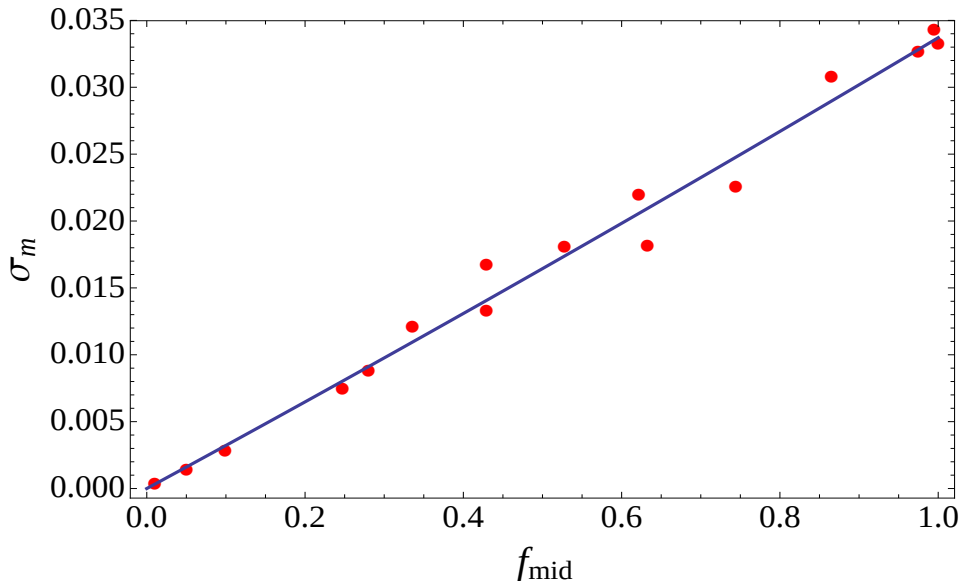

Figure 3.12: The standard deviation σ_m as a function of the fraction $f_{\rm mid}$ of the void mass on the shell for voids halfway to the source, for void radii of $R = 35$ Mpc and source redshift of $z_s = 1$. The solid line is a fit of the form $\sigma_m = \alpha f_{\rm mid} + \beta f_{\rm mid}^2$. For this choice of parameterization there is no statistically significant nonlinearity detectable in the data.

simulations. To illustrate this, we define, for a given source redshift z_s, the parameter

$$f_{\rm mid} \equiv f(z_s/2, f_0). \tag{3.73}$$

In other words, $f_{\rm mid}$ is the fraction of void mass on the shell for voids halfway to the source, the distance where most of the lensing occurs. We can use $f_{\rm mid}$ instead of f_0 as a parameter to describe our voids. With this choice of parameterization, the nonlinear evolution effect is significantly reduced. This is illustrated in Fig. 3.12, which shows the same data as in Fig. 3.10, but as a function of $f_{\rm mid}$ rather than f_0. The best fit parameters in the quadratic fit $\sigma_m = \alpha f_{\rm mid} + \beta f_{\rm mid}^2$ are now $\alpha = 0.032 \pm 0.005, \beta = 0.0016 \pm 0.0057$, showing that there is no statistically significant nonlinearity.

A third type of nonlinearity in our simulations arises from the nonlinear relation between the lensing convergence κ and the magnitude shift Δm. This effect should be present in our data but is quite small. If we neglect lens-lens coupling, shear, and the nonlinear evolution effect, then we expect logarithmic terms in the relation between σ_m and f_0, of the form

$$\sigma_m^2 \sim \alpha f_0^2 + \beta f_0^2 \ln f_0 + \ldots, \tag{3.74}$$

where α and β are constants which are independent of f_0. This follows from the analysis of Sec. 3.3.2 above, where the logarithmic divergence in the variance is cutoff at $\kappa \sim 1$; see Eqs. (3.49) and (3.51). However our data show that the logarithmic terms in Eq. (3.74) are quite small.

Next, we discuss the effects of allowing a distribution of values of void mass fraction on the shell f_0 in our simulations, rather than having a fixed value. We performed simulations where we pick a value of f for for each void crossing according to the following prescription. We choose a random values for $1/a_0$ from a Gaussian distribution with a mean of 8 and a variance of 30, truncated to lie in the range that corresponds to $0 \leq f \leq 1$. Figure 3.13 compares the probability distributions for magnitude shifts with and without variations in f. Treating f as a random variable increases the standard deviation σ_m by $\sim 3\%$.

3.4.3 Dependence on source redshift

Figure 3.14 shows the standard deviation σ_m of the magnitude shift distribution as a function of source redshift z_s, for three different void sizes. The standard deviation increases with redshift faster than z_s. This increase is due in part to the increasing number of voids but there are additional factors.

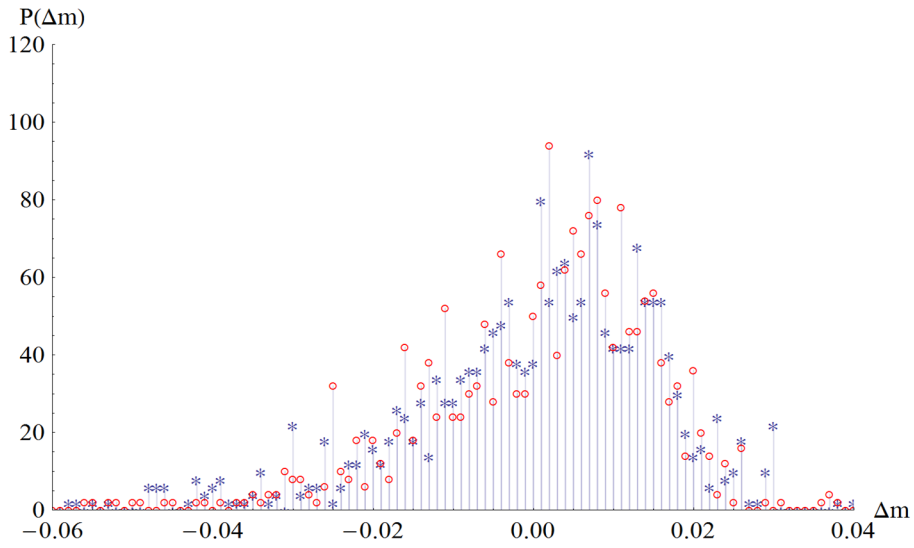

Figure 3.13: A comparison of the probability distributions of magnitude shifts Δm in two different cases: fraction of mass on the shell today fixed at $f_0 = 0.9$ (circles), and f_0 drawn from a distribution as described in the text (stars). In both cases void radius is $R = 35$ and source redshift is $z_s = 1.0$. The spread in the shell surface densities gives rise to a wider distribution of magnitude shifts, by about $\sim 3\%$.

To understand the redshift dependence analytically we use the expression for the dispersion in lensing convergence from weak lensing theory, given by Eq. (3.82) in Appendix 3.7. The matter power spectrum $\Delta(k,z)^2$ for our void model is proportional to $f(z)^2$, so we obtain that

$$\left\langle \kappa^2 \right\rangle \propto \int_0^{x_s} dx w(x,x_s)^2 f(z)^2, \tag{3.75}$$

where $w(x,x_s) = (1+z)H_0 x(x_s - x)/x_s$ and $f(z)$ is defined by Eq. (3.12). In the range of redshifts $0.5 \leq z_s \leq 1.5$ this redshift dependence is approximately a power law, proportional to $z_s^{1.35}$, to within $\sim 5\%$ percent[7]. This redshift dependence agrees with the results of our simulations shown in Fig. 3.14 to within $\sim 10\%$.

[7]The asymptotic behavior at large z_s is that the expression (3.75) increases linearly in z_s.

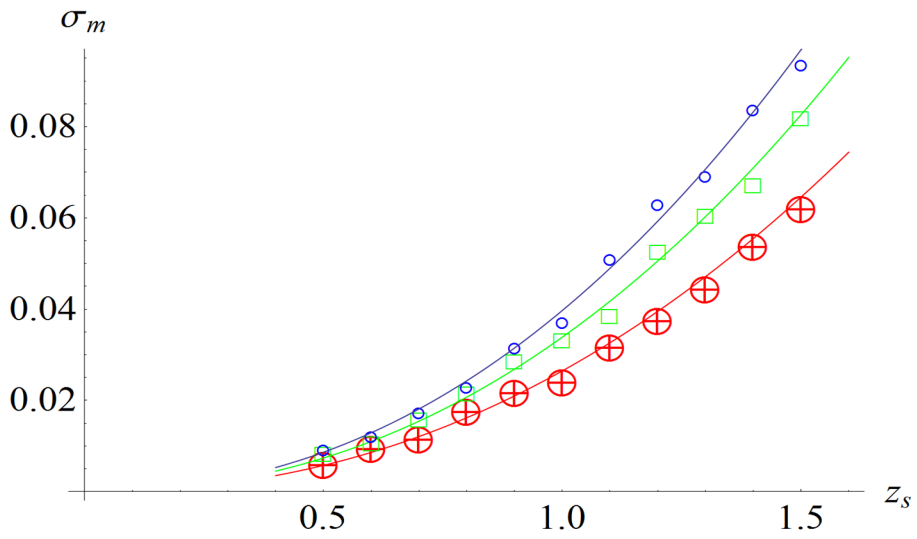

Figure 3.14: The standard deviation σ_m as a function of source redshift z_s, computed using $N = 10^6$ runs, for voids of radii $R = 35$ Mpc (red, crossed circles), 70 Mpc (green, squares), and 105 Mpc (blue, circles). The lines are fits proportional to the analytic estimate (3.75).

3.4.4 Numerical fit to parameter dependence

We complete this part of the analysis by giving a three parameter fit for the standard deviation σ_m as a function of void radius R, fraction of void mass on the shell today f_0, and source redshift z_s. The result is

$$\sigma_m \approx (0.027 \pm 0.0007)\left(\frac{R}{35\,\text{Mpc}}\right)^{\alpha}\left(\frac{f_0}{0.9}\right)^{\beta}\left(\frac{z_s}{1.0}\right)^{\gamma}, \tag{3.76}$$

where the parameters are $\alpha = 0.51 \pm 0.03$, $\beta = 1.07 \pm 0.04$, $\gamma = 1.34 \pm 0.05$. This fit is accurate to $\sim 20\%$ for $35\,\text{Mpc} \leq R \leq 350\,\text{Mpc}$, $0.01 \leq f_0 \leq 0.9$, $0.5 \leq z_s \leq 2.1$.

3.5 Bias due to sources occurring preferentially in high density regions

For sources which are randomly distributed in space, it is known that the total expected apparent luminosity of a source, including all primary and secondary images, must agree with that of the background FRW model [65]. Hence, in situations where the probability of caustics can be neglected, the probability distribution (3.32) of magnifications μ must be *unbiased*. Biases arise in our computations because of caustic effects, and also because we study the probability distribution of the magnitude shift Δm, which is a nonlinear function of μ, cf. Eq. (3.30).

However, there is an additional fundamental source of bias which arises from the fact that sources are *not* randomly distributed in space, and instead preferentially occur in high density regions, where they are more likely to be close to a lens. This is the source-lens clustering effect [90]. In this section, we make an analytical estimate of the bias δm of the distribution of magnitude shifts that is due to source-lens clustering in our void model.

In our computations so far in this chapter, we have placed the source outside the voids, in the FRW regions. However, in reality most matter is concentrated on the edges of voids, and so sources are more likely to be on the void edges. If we demand that sources always be located on void edges, then the mean of the distribution is shifted by an amount (see derivation below)

$$\delta m = \frac{1}{3\ln(10)}(1+z_s)\,H_0^2 R^2 \Omega_M f_s. \tag{3.77}$$

Here z_s is the redshift of the source and $f_s = f(z_s)$ is the fraction of mass on the shell for voids at the source redshift. Evaluating this estimate for $\Omega_M = 0.3$, $z_s =$

1.0, $R = 35$ Mpc, $f_0 = 0.9$ gives $\delta m \sim 5 \times 10^{-6}$, and $\delta m \sim 5 \times 10^{-4}$ for $R = 350\,\text{Mpc}$. These biases are below the accuracy of upcoming cosmology surveys.

Turn now to the derivation of the formula (3.77). We start from the standard formula (3.34) for the lensing convergence in weak lensing theory. We consider just the contribution to κ from the last void. In the integral, over this void, we approximate the factors x and $1/a_{\text{ex}}(z)$ as constants. Writing $\eta = x_s - x$ we obtain

$$\kappa_{\text{last void}} = \frac{3}{2} H_0^2 (1 + z_s)\, \Omega_M \int_{\text{last void}} \eta \delta_{\text{m}}(\mathbf{x}, t) d\eta. \tag{3.78}$$

We also neglect the time dependence of $\delta_{\text{m}}(\mathbf{x}, t)$ for integrating over the last void.

We now consider two different models for randomizing the relative displacement between the center of the last void and the source. We denote by b the transverse displacement of the void center from the line of sight, as before, and denote by η_v the distance from the void center to the plane through the source perpendicular to the line of sight.

In our first model, we assume b and η_v are randomly distributed, proportional to $b d\eta_v db$, with $0 \le \eta_v \le R$ and $0 \le b \le R$. Computing the integral (3.78) for our void model (3.6) gives

$$\begin{aligned} \kappa_{\text{last void}} \;&=\; \frac{3}{2} H_0^2 \Omega_M (1 + z_s) \\ &\times \begin{cases} -2 f_s \eta_v \alpha + \frac{2 f R^2 \eta_v}{3\alpha} & \eta_v > \alpha \\ -\frac{1}{2} f (\eta_v + \alpha)^2 + \frac{f R^2}{3\alpha} (\eta_v + \alpha) & \eta_v < \alpha \end{cases} \end{aligned} \tag{3.79}$$

where $\alpha = \sqrt{R^2 - b^2}$. Now averaging over b and η_v gives the expected value of $\langle \kappa_{\text{last void}} \rangle = (1 + z_s) H_0^2 R^2 \Omega_M f_s / 15$.

In the second model, we assume that b and η_v are correlated so that the source is always on the surface of the void. The average of $\kappa_{\text{last void}}(b,\, \eta_v)$ in this

model is

$$\langle \kappa_{\text{last void}} \rangle = \int_0^{\pi/2} \sin\theta \, \kappa\left(R\sin\theta,\ R\cos\theta\right) d\theta, \tag{3.80}$$

which using the formula (3.79) gives zero. Subtracting the means of the two models gives an estimate of the bias, and multiplying the result by $5/\ln 10$ to convert from $\delta\kappa$ to δm gives the formula (3.77).

3.6 Conclusions

In this chapter, we presented a simple model to study the effects of voids on distance modulus shifts due to gravitational lensing. A number of future surveys will gather data on luminosity distances to various different astronomical sources, to use them to constrain properties of the source of cosmic acceleration. The accuracy of the resulting constraints will be degraded somewhat by lensing due to nonlinear large scale structures. We studied this effect by considering a ΛCDM Swiss cheese cosmology with mass compensating, randomly located voids with uniform interiors surrounded by thin shells.

We used an algorithm to compute the probability distributions of distance modulus shifts similar to that of Holz & Wald [65]. The rms magnitude shift due to gravitational lensing of voids is fairly small; the dispersion σ_m due to 35 Mpc voids for sources at $z_s = 1$ is $\sigma_m = 0.031$, which is $\sim 2-3$ times smaller than that due to galaxy clusters (see Appendix 3.7 below). Also the mean magnitude shift due to voids is of order $\delta m \sim 0.003 \pm 0.001$. We also studied the bias that arises from the source-lens clustering effect, and estimated that the contribution from voids to this bias is quite small, of order $\delta m \sim 5 \times 10^{-6}$. Refining our model by giving each void shell a finite thickness of $\sim$ 1 Mpc reduces the dispersion

σ_m by a factor ~ 2.

We used our model to estimate the sizes of various nonlinear effects that go beyond linear, weak-lensing theory. We estimate that for $R = 35$ Mpc the dispersion σ_m is altered by $\sim 4\%$ by lens-lens coupling, by $\sim 3\%$ by shear. For 100 Mpc voids these numbers become 3% and 6% respectively.

Our simple and easily tunable model for void lensing can be used as a starting point to study more complicated effects. For example, one can use various algorithms to generate realizations of distributions of non-overlapping spheres in three dimensional space. Given such a realization one could use the algorithm of this chapter to study correlations between magnifications along rays with small angular separations, which would be relevant to future pencil beam surveys [107]. Finally, our model is complementary to other simplified lensing models in the literature that focus on lensing due to halos but neglect larger scale structures, for example the model of Refs. [81, 82].

3.7 Appendix A: Comparison with weak lensing theory

In this appendix we show that our results agree moderately well with the predictions of weak lensing theory, by computing an approximate matter power spectrum for our void model. We also obtain an independent estimate of the lensing due to voids by using the power spectrum of the Millennium simulation[78].

It is somewhat complicated to compute an exact power spectrum for our distribution of voids. As a simple model, we choose a two-void probability distri-

bution function for which the locations of the two voids are independently and uniformly distributed inside some large finite volume, except that the probability is set to zero when the distance between the void centers is less than $2R$. For this model, using the void density profile (3.6), we find for the power spectrum[8]

$$\Delta(k,z)^2 = \frac{2\alpha}{3\pi} f(z)^2 k^3 R^3 j_2(kR)^2 \left[1 - 12\alpha \frac{j_1(2kR)}{kR}\right]. \tag{3.81}$$

Here α is the void packing fraction, which is $\pi/6$ in our model, k is wavenumber, j_1 and j_2 are spherical Bessel functions of the first kind, and $f(z)$ is the fraction of the void mass in the shell, which can be computed as a function of redshift using the results of Sec. 3.2.1. We note that this power spectrum is not an exact representation of our void model, because in our procedure we first choose a direction to the source and then generate a density perturbation field that depends on this direction. Thus, our procedure does not correspond exactly to choosing a direction randomly in a pre-existing homogeneous, isotropic random process[9], i.e. $\langle \delta\rho(\mathbf{x})\delta\rho(\mathbf{y})\rangle$ is not just a function of $|\mathbf{x}-\mathbf{y}|$. Homogeneity is necessary in order to represent the two point function in terms of a power spectrum.

The power spectrum (3.81) is shown in Fig. 3.15, both with and without the correction factor in square brackets that arises from the correlation between void locations. For comparison, we also show in Fig. 3.15 an estimate of the nonlinear power spectrum[10] obtained from the Millennium simulation [78]. The figure

[8]This model is not completely consistent, since the power spectrum can become negative for large packing fractions. The inconsistency is presumably a signal that our assumed 2-void probability distribution cannot be obtained starting from any symmetric non-overlapping n-void probability distribution. We ignore this inconsistency here since the correlation effects that give rise to the correction factor in square brackets in Eq. (3.81) give only a small ($< 1\%$) correction to $\langle\kappa^2\rangle$ in any case.

[9]If the model were exactly homogeneous there would be a nonzero probability for the observer to be located inside a void.

[10]We use the following fit to the Millennium power spectrum, obtained from Fig. 9 of Ref. [78]: $\Delta(k,z)^2 = \alpha(k)(1+z)^{\beta(k)}$, where the functions α and β are chosen so that $\Delta(k)^2 = 1.40889 + 1.67105x - 0.11816x^2 - 0.0356049x^3 - 0.0367596x^4$ at $z = 0$ and $\Delta(k)^2 = 0.87558 + 1.56132x -$

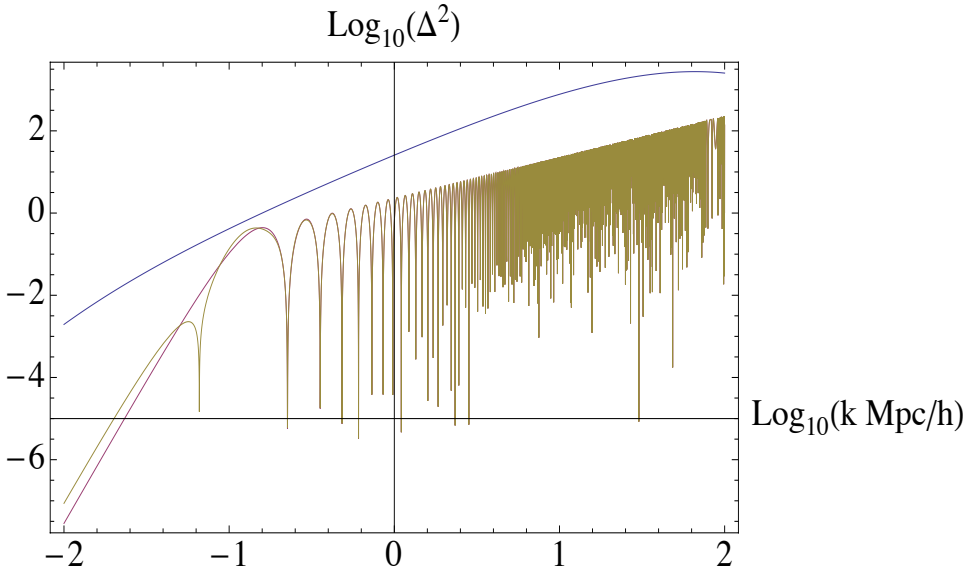

Figure 3.15: The estimate (3.81) of the matter power spectrum $\Delta(k,z)^2$ for our void distribution, as a function of comoving wavenumber k, evaluated today at $z = 0$. The lower curve includes the correlation correction factor in square brackets in Eq. (3.81), and the middle curve omits it. The upper curve is an approximate version of the nonlinear matter power spectrum at $z = 0$ obtained from the Millennium ΛCDM N-body simulation [78], shown for comparison. The parameter values chosen were $H_0 = 73\text{km s}^{-1}\,\text{Mpc}^{-1}$, $\Omega_M = 0.3$, $f_0 = f(0) = 0.9$, $R = 35\,\text{Mpc}$.

shows that our assumed void model is in rough agreement with the simulation: the two power spectra agree to within a factor $\sim 2-3$ at large scales, for $3\,\text{Mpc}k^{-1}30\,\text{Mpc}$, but disagree at small scales $k^{-1} \ll 1\text{Mpc}$, where the Millennium spectrum contains more power. This is as expected because our model does not attempt to model structure on these small scales.

We now turn to computing the effects of lensing using these power spectra. From the formula (3.34) for lensing convergence κ in weak lensing theory, it

$0.117482x^2 - 0.0299214x^3 - 0.0383988x^4$ at $z = 0.98$, where $x = \log_{10}(k\,\text{Mpc}/h)$. This fit is accurate to $\sim 30\%$.

follows that for subhorizon modes the variance in κ is [108, 77]

$$\left\langle \kappa^2 \right\rangle = \int d\ln k \left[\frac{9\pi}{4} H_0^2 \Omega_M^2 \int_0^{x_s} dx\, w(x, x_s)^2 \frac{\Delta(k,z)^2}{k} \right], \tag{3.82}$$

where x is comoving coordinate, x_s is the position of the source and $w = (1+z) H_0 x (x_s - x)/x_s$ is the lensing efficiency factor. The corresponding standard deviation in magnitude shift Δm is $\sigma_m = 5\sqrt{\langle\kappa^2\rangle}/\ln 10$, from Eq. (3.40). We compute the integrand of the $\ln k$ integral by numerically integrating over redshift, for a source redshift of $z_s = 1$. The result is shown in Fig. 3.16.

Consider first the result for our void distribution. Fig. 3.16 shows that the envelope of $d\left\langle\kappa^2\right\rangle/d\ln k$ asymptotes to a constant at large k, indicating a logarithmic divergence in the variance $\left\langle\kappa^2\right\rangle$. As discussed in the body of the chapter, this divergence is an artifact of our use of distributional density profile for each void, with a δ-function on the void's surface. The divergence can be regulated by endowing each shell with some small finite thickness Δr, which is approximately equivalent to truncating the integral over k in Eq. (3.82) at $k \sim 1/\Delta r$. Integrating Eq. (3.82) between $10^{-2}\mathrm{Mpc}^{-1}$ and $10^{2}\mathrm{Mpc}^{-1}$ gives the result $\sigma_m = 0.011$, which is substantially smaller than the result $\sigma_m = 0.031$ obtained from our nonlinear method in Sec. 3.4 above. The agreement is improved if we integrate up to $10^{5}\mathrm{Mpc}^{-1}$, corresponding the effective cutoff lengthscale in our simulations estimated in Sec. 3.3 (even though this shell thickness lengthscale is unrealistic). In this case $\sigma_m = 0.016$, a factor of ~ 2 smaller than our simulations. The factor ~ 2 disagreement is not too surprising, since as mentioned above the derivation of Eq. (3.82) requires the assumption that the density perturbation is a homogeneous isotropic random process, which is violated to some extent by our void model.

It is also of interest to compute the standard deviation σ_m for the Millennium

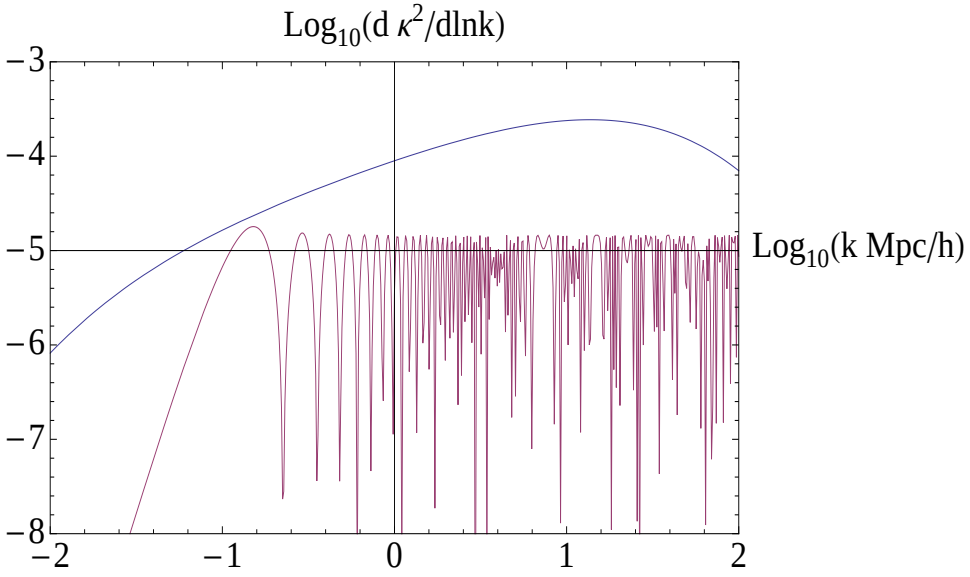

Figure 3.16: The variance of the lensing convergence per unit logarithmic wavenumber, $d\left\langle\kappa^2\right\rangle/d\ln k$, for a source at redshift $z_s = 1$, computed from the spectra shown in Fig. 3.15. The upper curve is the Millennium simulation, the lower curve is our void model.

simulation spectrum. Figure 3.16 shows that the variance of the lensing convergence per unit logarithmic wavenumber $d\left\langle\kappa^2\right\rangle/d\ln k$ peaks at $k \sim 100\,\mathrm{kpc}$ (in agreement with Sec. 10.5 of Ref. [68]). This indicates that lensing is dominated by galactic scale structures, as claimed by Holz & Wald [65]. The total standard deviation[11] from all scales $10^{-2}\mathrm{Mpc} \leq k^{-1} \leq 10^{3}\mathrm{Mpc}$ is $\sigma_m = 0.044$. The standard deviation from integrating only over the scales of voids $3\mathrm{Mpc} \leq k^{-1} \leq 10^{3}\mathrm{Mpc}$ is $\sigma_m = 0.010$, a factor ~ 4 smaller; this standard deviation agrees well with our estimate (3.2) for the thick-wall void model.

[11] This total standard deviation due to lensing computed using weak lensing theory and the Millennium simulation agrees well with that computed using other methods. For example, the corresponding standard deviation for $z_s = 1.5$ is $\sigma_m = 0.066$, which agrees within $\sim 20\%$ with the standard deviation of the distribution shown in Fig. 1 of Ref. [67].

3.8 Appendix B: Derivation of procedure for computing magnification distribution

In this appendix we describe in more detail the derivation of our prescription for computing magnifications along a ray given by Eqs. (3.14) – (3.18).

Consider an observer $\mathcal{O}$ and a source $\mathcal{S}$. The angular diameter distance $D_A(\mathcal{O}, \mathcal{S})$ is defined by

$$D_A^2 = \delta A / \delta\Omega \tag{3.83}$$

where δA is the proper area of the source, orthogonal to the direction to the observer, and $\delta\Omega$ is the observed solid angle at the observer subtended by the source. Under a conformal transformation of the metric, $\delta\Omega$ is invariant while δA transforms by a factor of the conformal factor evaluated at the source. It follows that if we define $\bar{D}_A$ to be the angular diameter distance computed in the conformally transformed spacetime (3.15), then we have $D_A = a(\mathcal{S})\bar{D}_A$, where a is the scale factor. We now define the magnification relative to FRW to be[12]

$$\mu = \frac{D_{A,0}^2}{D_A^2}, \tag{3.84}$$

where $D_{A,0}$ is the angular diameter distance computed in the unperturbed FRW model. Expressing the two angular diameter distances in Eq. (3.84) in terms of the conformally transformed versions, the factors of $a(\mathcal{S})$ cancel[13], and we obtain that

$$\mu = \bar{D}_{A,0}^2 / \bar{D}_A^2 = x_s^2 / \bar{D}_A^2, \tag{3.85}$$

where x_s is the comoving coordinate of the source.

[12]This definition could equivalently be expressed in terms of luminosity distances D_L, since $D_L = (1+z)^2 D_A$ for any spacetime.

[13]We neglect the contribution to μ caused by the perturbation in the observed redshift of the source, which enters when we express the magnification in terms of the observed redshift. This effect gives a subdominant contribution to μ for subhorizon modes [109, 110].

To compute the angular diameter distance $\bar{D}_A(\mathcal{O},\mathcal{S})$ in the conformally transformed spacetime (3.15), we use the same method that Holz & Wald [65] used in the physical spacetime, whose derivation we now outline in the context of an arbitrary spacetime. Let $\vec{k} = d/dx$ be the past-directed tangent vector to the null geodesic joining $\mathcal{O}$ and $\mathcal{S}$, where x is affine parameter with $x = 0$ at $\mathcal{O}$. We choose vectors $\vec{l}, \vec{e}_1, \vec{e}_2$ at $\mathcal{O}$ so that $\vec{e}_{\hat{\alpha}} = (\vec{k}, \vec{l}, \vec{e}_A)$, $A = 1, 2$ form an orthonormal basis, i.e., satisfy $\vec{k}^2 = \vec{l}^2 = \vec{k}\cdot\vec{e}_A = \vec{l}\cdot\vec{e}_A = 0$, $\vec{k}\cdot\vec{l} = -1$, $\vec{e}_A\cdot\vec{e}_B = \delta_{AB}$. This orthonormal basis is extended along the geodesic by parallel transport.

Now let $\vec{\eta}(x)$ be an infinitesimal connecting vector that joins the geodesic to some nearby geodesic. The components of $\vec{\eta}$ on the orthonormal basis satisfy the geodesic deviation equation $d^2\eta^{\hat{\alpha}}/dx^2 = -R^{\hat{\alpha}\hat{\beta}\hat{\gamma}\hat{\delta}}k_{\hat{\beta}}k_{\hat{\delta}}\eta_{\hat{\gamma}}$. More explicitly, expanding $\vec{\eta} = \mu\vec{k} + \nu\vec{l} + \eta^A\vec{e}_A$, the geodesic deviation equation becomes

$$\ddot{\nu} = 0, \tag{3.86}$$

$$\ddot{\mu} = \nu\mathcal{R} - \eta_C\mathcal{R}^C, \tag{3.87}$$

$$\ddot{\eta}^A = \nu\mathcal{R}^A - \eta_C\mathcal{R}^{AC}. \tag{3.88}$$

Here dots denote derivatives with respect to x, $\mathcal{R} = R_{abcd}k^a l^b k^c l^d$, $\mathcal{R}_A = -R_{abcd}k^a l^b k^c e^d_A$, and $\mathcal{R}_{AB} = R_{abcd}k^a e^b_A k^c e^d_B$.

We are interested in a set $\mathcal{B}$ of rays all of which pass through $\mathcal{O}$ and which define an element of solid angle $\delta\Omega$ at $\mathcal{O}$. The corresponding deviation vectors $\vec{\eta}(0)$ must vanish at $\mathcal{O}$, and the initial derivatives $d\vec{\eta}/dx(0)$ are orthogonal both to $\vec{k}$ and to the four velocity of the observer, $\vec{u}_{\mathcal{O}}$. If we specialize the choice of orthonormal basis so that $\vec{u}_{\mathcal{O}}\cdot\vec{e}_A = 0$, then it follows that $\nu = \dot{\nu} = 0$ at $\mathcal{O}$, and from Eq. (3.86) we obtain that $\nu(x) = 0$ everywhere. By the linearity of the geodesic deviation equation it now follows that

$$\eta^A(x) = \mathcal{A}^A{}_B(x)\dot{\eta}^B(0) \tag{3.89}$$

for some 2×2 matrix $\mathcal{A}^A{}_B$. This matrix satisfies the differential equation (3.16) and initial conditions (3.17) given in Sec. 3.2.3 above, from Eq. (3.88) with $\nu = 0$. We define the quantity

$$\Delta(\mathcal{O}, \mathcal{S}) = \frac{x_s^2}{\det \mathcal{A}(x_s)}, \tag{3.90}$$

which is the so-called van Vleck determinant [111]. One can show that this is invariant under rescaling of affine parameter, under changes of the orthonormal basis that preserve $\vec{k}$, and under interchange of $\mathcal{O}$ and $\mathcal{S}$.

We now define a set of angular coordinates $\theta = \theta^A$ that parameterize the solid angle measured by the observer, by $\theta^A = \theta_0^A + \dot{\eta}^A(0)/(\vec{k} \cdot \vec{u}_O)$, where θ_0 is the direction to the source. The element of solid angle is then

$$\begin{aligned} \delta\Omega &= \int_{\mathcal{B}} d^2\theta = \frac{1}{(\vec{k} \cdot \vec{u}_O)^2} \int_{\mathcal{B}} d^2\dot{\eta}^A(0) \\ &= \frac{1}{(\vec{k} \cdot \vec{u}_O)^2 \, |\det \mathcal{A}(x_s)|} \int_{\mathcal{B}} d^2\eta^A(x_s), \end{aligned} \tag{3.91}$$

where we have rewritten the integral using the Jacobian of the transformation (3.89).

Now consider the element of area δA measured at the source $\mathcal{S}$. This is defined to be the area in the rest frame of the source, orthogonal to the direction to the observer. We choose an orthonormal basis $\vec{k}, \vec{l}', \vec{e}'_A$ at $\mathcal{S}$ so that the four velocity is $(\vec{k} + \vec{l}')/2$, and decompose the connecting vector as $\vec{\eta} = \mu' \vec{k} + \nu' \vec{l}' + \eta'^A \vec{e}'_A$. Then the area is just $\delta A = \int_{\mathcal{B}} d^2\eta'^A$. Now the two orthonormal bases $(\vec{k}, \vec{l}, \vec{e}_A)$ and $(\vec{k}, \vec{l}', \vec{e}'_A)$ at $\mathcal{S}$ are related by some fixed Lorentz transformation, so we obtain

$$\begin{aligned} \nu &= \nu', \\ \mu &= \mu' + \frac{1}{2}\nu' \mathbf{D}^2 + H_{AB}\eta'^A D^B, \\ \eta^B &= H_A{}^B \eta'^A + \nu' D^B, \end{aligned} \tag{3.92}$$

for some $SO(2)$ matrix H_{AB} and vector D^A. Since $\nu = 0$ everywhere it follows that η^A and η'^A are related by an $SO(2)$ transformation, which preserves area, and so $\delta A = \int_{\mathcal{B}} d^2\eta^A(x_s)$. Combining this with Eqs. (3.83), (3.90) and (3.91) now gives for the angular diameter distance

$$D_A(\mathcal{O},\mathcal{S})^2 = \frac{x_s^2(\vec{k}\cdot\vec{u}_O)^2}{|\Delta(\mathcal{O},\mathcal{S})|}. \tag{3.93}$$

This is independent of the normalization of the affine parameter and of the four-velocity of the source, but does depend on the four-velocity of the observer.

We now apply the formula (3.93) to a stationary observer in the perturbed Minkowski spacetime (3.15), to obtain the angular diameter distance $\bar{D}_A$ of Eq. (3.85) above. Specializing the affine parameter x to be the comoving coordinate gives $\vec{k}\cdot\vec{u}_O = 1$, and then combining Eqs. (3.85), (3.90) and (3.93) gives the magnification formula (3.18).

Finally, we note that in computing the matrix $\mathcal{A}(x_s)$, we follow Holz & Wald [65] in neglecting the influence of the metric perturbation on the background geodesic, and on the parallel transport of the orthonormal basis. The corresponding corrections to the angular diameter distance have been computed in the weak lensing limit in Refs. [109, 110] and are subdominant for subhorizon modes.

3.9 Appendix C: Comparison with other studies of lensing due to voids

Luminosity distance in the context of Swiss Cheese cosmology has been studied by Clifton & Zuntz [91], Brouzakis, Tetradis & Tzavara [86, 92], Szybka [93] and

Biswas & Notari [94]. Other studies in perturbed FRW cosmologies have been done by Holz & Wald [65] and Hui & Greene [112]. In this appendix we summarize the relevant results from this literature and compare with our results.

In Clifton & Zuntz [91], the mean and standard deviation of apparent magnitude shifts are studied for redshifts up to $z_s \sim 1$ in ΛCDM cosmology. One difference between their study and ours is that they model voids using a fully relativistic Lemaitre-Tolman-Bondi model with a smooth choice of density profile, whereas we use a simpler Newtonian model where each void consists of a central uniformly underdense region surrounded by a zero thickness shell. Fractional corrections to the Newtonian approximation scale as $(H_0 R)^2 \sim 0.0001$ for 35 Mpc voids, so a fully relativistic void model is not really necessary; our model is substantially simpler than theirs. A second difference between the two studies is that they choose a configuration of voids where the void centers lie along the line of sight. Due to this choice, the lensing contributions from successive voids add coherently instead of random walking, which significantly changes the magnification probability distribution. Specifically, for $z_s = 1$ and deep voids, Clifton & Zuntz obtain a standard deviation in modulus shift of $\sigma_m \sim 0.01$ (their Fig. 16), similar to our value, but they obtain a mean shift of $\langle \delta m \rangle \sim 0.02$, a factor ~ 10 larger than ours. This difference arises from their lack of randomization of impact parameters.

Other similar studies are those of Brouzakis, Tetradis & Tzavara [92] and Biswas & Notari [94]. Brouzakis *et al.* also use a fully relativistic Lemaitre-Tolman-Bondi void model with a smooth choice of density profile. They find values of standard deviation σ_m which agree to within $\sim 30\%$ with our model; see their Fig. 5 which applies to $R = 40$ Mpc voids at $z_s = 1$. Brouzakis *et al.*

[92] and also Biswas & Notari [94] studied the dependence of the magnification distribution on void sizes, source redshift, and fractional underdensity in the void interior, and found results which agree qualitatively with ours. The effects of randomizing void impact parameters was also studied by Szybka [93], who found as did we that the dimming effect due to voids is not enough to mimic the effect of dark energy. The effect of shear is also studied by Szybka, who found its effects to be very small, in agreement with our results discussed in Sec. 3.4.2 above. The main advantage of our model compared to these studies is simplicity: our model allows us to explore and understand the effects of a wide range of parameter values.

Kainulainen & Marra [81, 82] introduce a different technique to study lensing. While we compute the probability distribution of magnifications by doing Monte Carlo simulations of ray tracing, Kainulainen & Marra [81] develop a method that allows them to rapidly compute an approximate form of the entire probability distribution through a combination of numerical and analytical techniques. However, their application of this method focus on the lensing due to galaxies and halos, not on the larger-scale structures of sheets and voids, so our study is not directly comparable to theirs. We note however that it should be possible to apply their techniques to compute the lensing due to voids.

Finally, a recent paper by Lavallaz & Fairbairn [113] performs a similar study modeling voids as 30 Mpc Lemaitre-Tolman-Bondi spheres with Kostov parameterization [114]. They assume that the supernovae number density is proportional to the mass density inside voids and they study the redshift range $0.01 < z < 2.0$. They find that if there is essentially no cut off in the lower range of z, the scatter in the inferred equation of state parameter w is about 10%, while

imposing a cut off in the lower range of z decreases the scatter.

CHAPTER 4

LUMINOSITY DISTANCE IN SWISS CHEESE COSMOLOGY WITH RANDOMIZED VOIDS AND GALAXY HALOS

4.1 Introduction

A number of surveys are being planned to determine luminosity distances to various different astronomical sources, and to use them to constrain properties of the dark energy or modification to gravity that drives the cosmic acceleration. Perturbations to luminosity distances due to gravitational lensing by large scale and galaxy scale structures are a source of error for these studies, see, e.g., Refs [115, 116, 117, 118, 119, 120].

In this chapter we use the computational method developed in Ref. [115] to study the effect of density inhomogeneities on luminosity distances in two idealized "Swiss cheese" models [117, 121, 122, 123, 124] of large scale ($\sim$ 30 Mpc) and galaxy scale structures. Our models seek to capture the property that most of the matter is concentrated in galaxy halos on the outer edges of voids while the void interiors are relatively sparse. Our first model is an extension of our previous work [115] where we idealize the interior of a spherical void as a uniform underdense region and the surface of the sphere contains a randomized distribution of galaxy halos with Navarro–Frenk–White (NFW) profiles [127]. Our second model retains the randomly distributed galaxy halos on the surface of the voids, and replaces the interior uniform density with randomly distributed galaxy halos with NFW profiles. In both models we keep fixed the parameters of the voids and halos. Even though neither of these models represent realistic matter distributions within a void, they should capture the main

qualitative features of lensing.

4.1.1 Summary of Computation and Results

In Section 4.2, we give a detailed description of the NFW halo density profile that we adopt which is motivated by observations. We also describe our two models of the entire distribution of matter, including both large scale void structures and smaller scale halo structures.

In Section 4.3, we review the method we use to compute the distribution of lensing magnifications. We then describe how to compute the lensing convergence for a single halo. We compare our numerical results for the distribution of magnifications with analytic expressions. We also estimate the number of realizations required to get a reasonable accuracy in the computed distribution of magnifications (e.g, obtain the mean of the distribution to an accuracy of $< 1\%$). The accuracy of the numerical results scales as $N^{-1/2}$ as expected, where N is the number of realizations.

In Section 4.4, we study our first Swiss cheese model. We start by describing the model, and study the propagation of light rays through just a single void. Then, we derive analytic results for the magnification and use these to check our numerical results. We study the expected number of halo intersections, the redshift dependence of the magnification distribution, and determine the contribution of shear to our results. We note that the standard deviation is ~ 3 times larger than that due to voids with no halos, specifically the model of [115] consisting of voids of radius 35 Mpc with smooth underdense interiors and a smooth overdensity concentrated on the surface of the sphere with a thickness

of 1 Mpc. We show that the redshift dependence of the mean and standard deviation agrees with analytic results to $< 10\%$. We also note that the standard deviation changes by less than 3% if shear is neglected (see Section IV C below).

One effect which our models do not include is the clustering of halos, that is, the correlations between the locations of different halos. While it would be more realistic to include the effects of clustering, our simplified models should capture the essence of the effects of large scale inhomogeneities.

In Section 4.5, we study the second Swiss cheese model. Again, we first describe the model and study just a single void. We derive analytic results for the lensing convergences and use these to check our numerical results. There is a higher probability of demagnification; this shift is expected because the density contrast inside the void is now sharper because it is empty (with a smattering of a small number of halos) whereas the first model has a smooth interior matter distribution. The redshift dependence of the mean and standard deviation of the second model are similar to those of the first model. In the two models we consider, the standard deviations of this distribution are 0.065 and 0.072 magnitudes and the means are -0.0010 and -0.0013 magnitudes, for voids of radius 35 Mpc, sources at redshift 1.5, with the voids chosen so that 90% of the mass is on the shell today. We compare the distributions for configurations with and without voids for a source at $z_s = 1.5$. We find that the voids do not significantly change the variance but do significantly change the demagnification tail and the mode.

We find that since the distribution is skewed, the mode is positive, while the variance is determined primarily by rays that intersect halos. The scale of the voids does not significantly influence our results. The main parameters that

determine the mode and variance of the distribution is the mean column depth and concentration of halos and the fraction of the mass density that is in the form of halos (as opposed to smoothly distributed). The distribution of halos in space (i.e., in the interior versus the surface) is unimportant. Hence, our models bracket the range of possibilities of magnifications. Our analysis is generally consistent with other analytic and computational results [128, 129, 130, 131, 132, 133, 134, 135, 136]. We also compare our results to those of Kainulainen & Marra [125, 126] who use a similar but slightly different simplified model of large scale structure.

4.2 Model of Lensing Due to Galaxy halos and Voids

4.2.1 Galaxy halo profile

We model the galaxy halos with an NFW profile [127], with a density distribution

$$\rho_{\rm halo}\left(r\right) = \begin{cases} 0 & r \geqslant CR_s \\ \frac{\rho_0 R_{\rm s}^3}{r(r+R_{\rm s})^2} & r \leqslant CR_s \end{cases} . \tag{4.1}$$

Here r is the proper spherical radial coordinate, R_s is the physical radius which defines the core of the halo where most of the mass is concentrated, C the ratio of the radius of the halo to the core radius R_s, and the parameter ρ_0 is determined by the total mass of the halo. The corresponding total halo mass is

$$M_{\rm halo} = 4\pi\rho_0 R_{\rm s}^3 \left(\log\left(1+C\right) - \frac{C}{1+C}\right). \tag{4.2}$$

Quantity	Value
$M_{\rm halo}$	$1.25 \times 10^{12} M_{\odot}$
$R_{\rm s}$	0.03 Mpc
C	10

Table 4.1: Parameters of halo with NFW profile

For all our simulations we use $M_{\rm halo} = 1.25 \times 10^{12} M_{\odot}$, $R_s = 30$ kpc and $C = 10$ [**?**, **?**, **?**]. These values determine the halo density parameter ρ_0. This completely defines our NFW halo model and we list our parameters in Table I. In this chapter we keep the halo parameters fixed, but it would be straightforward to explore other values.

4.2.2 Our void models

In Swiss cheese models, the Universe contains a network of spherical, non-overlapping, mass-compensated voids. The voids are chosen to be mass compensated so that the potential perturbation vanishes outside each void. Mass flows outward from the evacuated interior and is then trapped on the shell wall. In our previous work, [115], we considered a uniformly underdense interior with a δ-function shell on the surface. This model is determined by a fixed comoving radius R and by the fraction, f, of the total void mass on the shell today. These parameters determine the evolution with time of the interior mass density and the surface mass density.

In this chapter we generalize the models of [115] to include the halo substructure of the voids. We consider two different idealized models. In the first, each void consists of a central, uniformly underdense region surrounded by a shell

consisting of randomly distributed halos, and in the second, halos are placed randomly both in the interior and on the surface. The zero thickness shell is thus replaced by halos randomly distributed on the surface of the sphere, with the number of halos chosen to match the mass of the shell. The number of halos thus evolves with time. We call our first model the Swiss Raisin Nougat (SRN) model, with "raisins" denoting halos and "nougat" the smooth void interior. We call the second model the Swiss Raisin Raisin (SRR) model.

For a given void, we denote by $\mathbf{r}$ the physical displacement from the center of the void at $\mathbf{r} = 0$, and we denote by $\mathbf{s} = \mathbf{r}a_{\rm ex}(z)$ the comoving displacement, where $a_{\rm ex}(z)$ is the scale factor of the background ΛCDM Friedman-Robertson-Walker (FRW) cosmology. The quantity that determines the lensing magnification is the density perturbation

$$\Delta\rho(\mathbf{r},\ z) = \rho(\mathbf{r},\ z) - \rho_{\rm FRW}(z), \tag{4.3}$$

where $\rho_{\rm FRW}(z) = 3H_0^2\Omega_{\rm M}/\left(8\pi G a_{\rm ex}^3(z)\right)$ is the background FRW density and z is redshift. For the SRN model the density perturbation is

$$\begin{aligned}\Delta\rho_{\rm SRN}(\mathbf{r}) = &-f(z)\,\rho_{\rm FRW}(z)\,\Theta(a_{\rm ex}Y_{\rm void} - r)\\ &+\sum_{i=1}^{N_{\rm shell}(z)}\rho_{\rm halo}(|\mathbf{r} - a_{\rm ex}Y_{\rm void}\hat{\mathbf{n}}_i|),\end{aligned} \tag{4.4}$$

where the first term is the smoothly distributed interior underdensity and the second term is due to halos on the surface. Here $f(z)$ is the fraction of the mass of the sphere on the surface [115], $Y_{\rm void}$ is the (constant) comoving void radius, Θ is the step function, $N_{\rm shell}$ is the number of halos on the surface, and $\hat{\mathbf{n}}_i$ is a randomly chosen unit vector giving the location of the i-th halo on the surface of the sphere. The number of surface halos is

$$N_{\rm shell}(z) = f(z)\,\frac{M_{\rm void}}{M_{\rm halo}}, \tag{4.5}$$

where

$$M_{\text{void}} = \frac{4}{3}\pi Y_{\text{void}}^3 a_{\text{ex}}^3 \rho_{\text{FRW}} \tag{4.6}$$

is the conserved total void mass.

For the SRR model, the density perturbation is

$$\begin{aligned}\Delta\rho_{\text{SRR}}(\mathbf{r}) = &-\rho_{\text{FRW}}(z)\,\Theta\left(a_{\text{ex}} Y_{\text{void}} - r\right) \\ &+ \sum_{i=1}^{N_{\text{shell}}(z)} \rho_{\text{halo}}\left(|\mathbf{r} - a_{\text{ex}} Y_{\text{void}} \hat{\mathbf{n}}_i|\right) \\ &+ \sum_{i=1}^{N_{\text{core}}(z)} \rho_{\text{halo}}\left(|\mathbf{r} - a_{\text{ex}} Y_{\text{void}} \mathbf{m}_i|\right),\end{aligned} \tag{4.7}$$

where the last term represents the halos in the interior. Here $N_{\text{core}}(z) = (1 - f(z))\, M_{\text{void}}/M_{\text{halo}}$ is the number of interior halos and the vectors $\mathbf{m}_j$ are randomly chosen in the interior of the unit sphere.

Now consider a light ray that intersects the void. A key role in our computations will be played by the impact parameters of the ray with respect to the center of the void, and with respect to the centers of the halos. These impact parameters will be two dimensional vectors in the plane perpendicular to the unperturbed ray. Specifically, we introduce a basis of three orthonormal spatial vectors $\mathbf{e}_1$, $\mathbf{e}_2$ and $\mathbf{e}_3$ with $\mathbf{e}_3$ along the direction of the ray. We denote by

$$\mathbf{p} = \sum_{A=1,\,2} p^A \mathbf{e}_A \tag{4.8}$$

the comoving impact parameter of the ray with respect to the center of the void. We denote by

$$\mathbf{b}_i = \sum_A b_i^A \mathbf{e}_A = \sum_A a_{\text{ex}} \left[p^A - Y_{\text{void}} \hat{n}_i^A\right] \mathbf{e}_A \tag{4.9}$$

the physical impact parameter of the ray with respect to the center of the i-th halo on the surface, where we have decomposed the unit vectors $\hat{\mathbf{n}}_i$ as $\hat{\mathbf{n}}_i =$

$\sum_A \hat{n}_i^A \mathbf{e}_A + \hat{n}_i^3 \mathbf{e}_3$. Similar formulae are obtained for the impact parameters of the interior halos.

Even though the SRN and SRR models are highly idealized, they are more realistic than the void models in our previous work [115]. A key feature of our idealized models is that they can be evolved in time continuously and very simply. Within the context of this highly idealized class of models, we study the distribution of magnitude shifts relative to what would be found in a smooth cold dark matter (CDM) model of the Universe with a cosmological constant, L, for different source redshifts.

It is important to note that our models are not spherically symmetric, as we break up the shell to form halos. We assume that nevertheless the large scale evolution of a void is the same as it would be in spherical symmetry. We also neglect gravitational clustering of halos on void surfaces. Our main aim is to investigate the role of small scale clumps in producing magnitude shifts.

To compute the effects of rays passing through our cosmology, we follow the steps described in Section 4.2.3 of [115], with the added halo contributions. Specifically, we compute a 4×4 matrix for each void, multiply all the matrices together, and compute the total magnification from the final 4×4 matrix. The explicit expressions for the 4×4 matrices in term of line integrals of derivatives of the gravitational potential are given in Eqs. (2.18) - (2.20) of [115]. We drop all of the integrals over the projected Riemann tensor in Eqs. (2.19) of [115] except the one in the formula for L_C^A. We then repeat the computation $N >> 1$ times to build up the distribution of magnifications.

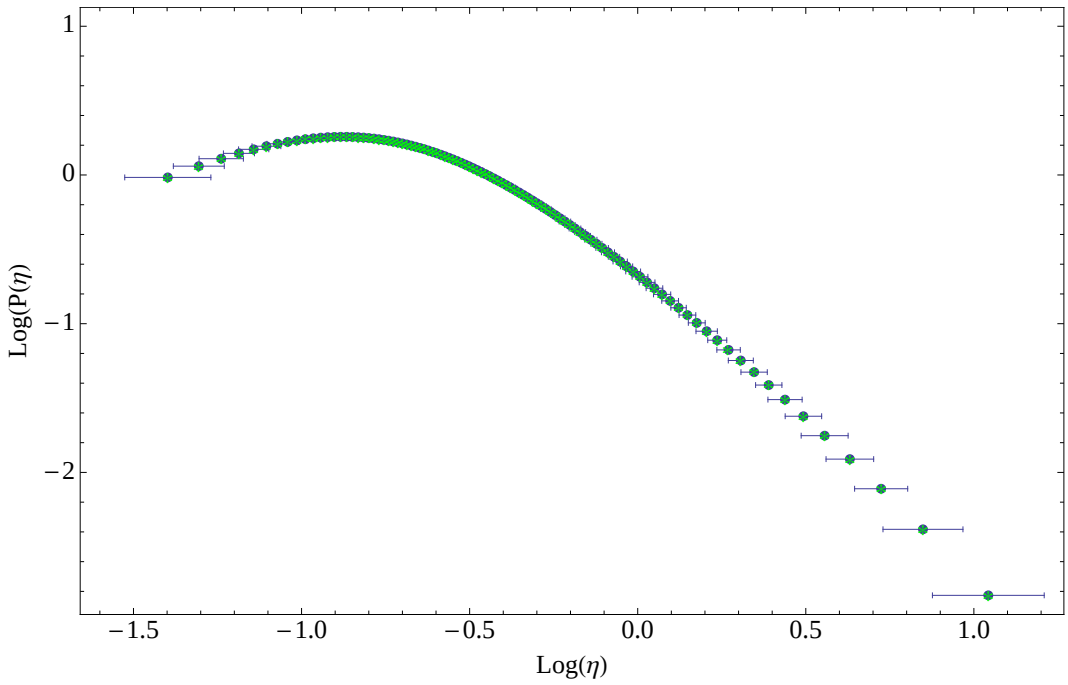

Figure 4.1: Comparison between numerical (points with ranges) and analytic results (starred points) for the distribution of integrated column depths.

4.3 Results for a Single Halo

We now discuss the distribution of magnifications due to a single halo. The halo has two distinct regions, the core $x < R_s$ and the external region $R_s < x < CR_s$. Here x is the physical distance. To compute the magnification, we first compute the lensing convergence, κ, analytically. For a general density contrast $\delta(\mathbf{s}) = \Delta\rho(\mathbf{s})/\rho_{\rm FRW}$ this is given by

$$\kappa = \frac{3}{2}\frac{H_0^2}{c^2}\Omega_{\rm M}\int_0^{y_S} dy \frac{y(y_S - y)}{y_S a_{\rm ex}(z)}\delta(y,\ z)\,, \tag{4.10}$$

where y is comoving distance along the ray, y_S is the comoving distance to the source, $a_{\rm ex}(z) = (1+z)^{-1}$, H_0 is the Hubble constant, c is the velocity of light, $\Omega_{\rm M}$ is the matter fraction and $z = z(y)$ is redshift. Combining the halo profile (4.1) and the second term in Eq. (4.4) with Eq. (4.10) gives for the lensing convergence

due to the halo

$$\kappa(b) = \frac{8\pi G a_{\rm ex}(z)}{c^2}(\rho_0 R_s)\frac{y(y_{\rm S}-y)}{y_{\rm S}}$$
$$[\kappa_{\rm core}\Theta(R_s-b) + \kappa_{\rm out}\Theta(b-R_s)\Theta(CR_s-b)]. \tag{4.11}$$

Here $b = |\mathbf{b}|$ is the physical impact parameter

$$\kappa_{\rm core} = \left(-\frac{\sqrt{C^2-\alpha}}{(1-\alpha)(1+C)} + \frac{2}{(1-\alpha)^{3/2}}\right.$$
$$\left.\left[\tanh^{-1}\left(\frac{\sqrt{1-\sqrt{\alpha}}}{\sqrt{1+\sqrt{\alpha}}}\right) - \tanh^{-1}\left(\frac{\sqrt{1-\alpha}}{C+\sqrt{C^2-\alpha}+1}\right)\right]\right) \tag{4.12}$$

and

$$\kappa_{\rm out} = \left(\frac{\sqrt{C^2-\alpha}}{(\alpha-1)(1+C)} - \frac{2}{(\alpha-1)^{3/2}}\right.$$

$$\left.\left[\tan^{-1}\left(\frac{\sqrt{\sqrt{\alpha}-1}}{\sqrt{\sqrt{\alpha}+1}}\right) - \tan^{-1}\left(\frac{\sqrt{\alpha-1}}{C+\sqrt{C^2-\alpha}+1}\right)\right]\right). \tag{4.13}$$

Here Θ is the step function and $\alpha = b^2/R_{\rm s}^2$. Note that $\alpha < 1$ for $b < R_{\rm s}$, $\alpha > 1$ for $R_{\rm s} < b < CR_{\rm s}$ and $\kappa = 0$ for $b > CR_{\rm s}$.

Finally, the mean of the lensing convergence for a single halo is obtained by averaging over the impact parameter

$$\hat{\kappa} = \frac{2}{(CR_{\rm s})^2}\int_0^{CR_{\rm s}} \kappa(b)\, b db \tag{4.14}$$

$$\hat{\kappa} = \frac{8\pi G a_{\rm ex}(z)}{c^2}(\rho_0 R_s)\frac{y(y_{\rm S}-y)}{y_{\rm S}}\frac{M_{\rm halo}}{(CR_{\rm s})^2}. \tag{4.15}$$

We define $\eta = \int \rho(z)\, dz$ to be the integrated column density which is proportional to the convergence κ. Figure 4.1 is a comparison of $\log_{10}(P(\eta))$, the logarithm of the probability distribution of η, computed analytically (starred

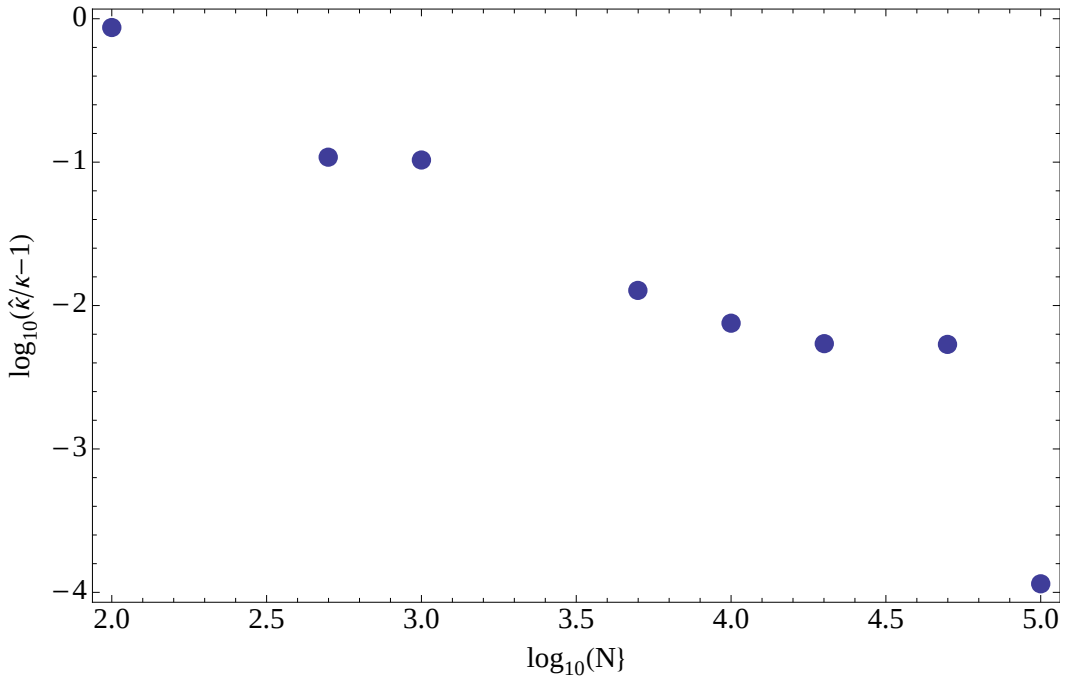

Figure 4.2: The difference between numerically (κ) and analytically computed mean convergences ($\hat{\kappa}$) as a function of number of runs N, for one void, comoving void radius $R = 35$ Mpc, and fraction of void mass on the shell today 0.9. Our numerical simulations agree with the analytic result to $< 1\%$ for $N = 10^4$.

points, Eq. (4.45) from Appendix A) and the results from our code (points associated with the η bins). Within each η bin, the mean of the bins agree well with analytic results. The width of the bins represents the sampling accuracy within those bins, the centers of halos are sampled less than the rest of the halos.

To further assess the accuracy of our numerical results, we compute the mean of the distribution for a single halo for different numbers of runs (N), and compare this with the analytic expression (4.15). We find that the results from our numerics agree with the theoretical prediction with an accuracy $\sim N^{-1/2}$ as expected. In Figure 4.2, we plot the estimator of the mean as a function of N. We see that the accuracy is ¡1% for $N = 10^4$. For the rest of the simulations in this chapter, we will use $N = 10^4$.

Quantity	Value
Ω_M	0.3
Ω_Λ	0.7
H_0	70 $\text{kms}^{-1}\text{Mpc}^{-1}$
Y_{void}	35 Mpc
Halo profile	NFW
Present fraction of void mass on shell	0.9
Fraction of shell mass in halos	1.0
Fraction of interior mass in halos	0.0

Table 4.2: Parameters of SRN model

4.4 Results for the Swiss Raisin Nougat Model

The Swiss Raisin Nougat (SRN) model is an idealized Swiss Cheese model containing spherical voids with comoving radius $Y_{\text{void}} = 35$ Mpc. As explained earlier, the matter in the interior moves towards the outer edges of the void with the evolution of the Universe. For a particular void at some redshift, we break up the mass on the shell of the void into halos with NFW profiles and randomly distribute them on the shell. The mass in the interior is smeared smoothly inside the sphere with a uniform mass density. The parameters of this model are listed in Table II.

A key change from our void models in [115] is that there is no longer a zero thickness shell. One of the issues encountered in that model was the logarithmic divergence in the variance of the lensing convergence distribution due to the zero thickness assumption. Here, however, we break up the void surface into halos and the effective thickness of the shell is set by the size of these halos which acts as a natural cutoff. Hence, the divergence is avoided which makes for a more realistic and robust model.

4.4.1 Probability of intersecting a halo

The expected number of times a light ray hits a halo is given by the ratio of the total projected area of all the halos in a void to the projected area of the void. The expected number of intersections at comoving impact parameter $p = |\mathbf{p}|$ (comoving distance from the center of the void) through the shell at redshift z is

$$N_{\rm int}\left(p,\ z\right) = \frac{f\left(z\right) M_{\rm void}\left(z\right)}{4\pi Y_{\rm void}^2 a_{\rm ex}^3\left(z\right) M_{\rm halo}} \pi R_{\rm halo}^2 a_{\rm ex}^3\left(z\right) \times$$

$$\int_0^{\sqrt{Y_{\rm void}^2 - p^2}} ds \delta\left(\sqrt{s^2 + p^2} - Y_{\rm void}\right) \tag{4.16}$$

$$= \frac{f\left(z\right) M_{\rm void}\left(z\right) R_{\rm halo}^2}{2 Y_{\rm void} \sqrt{Y_{\rm void}^2 - p^2 a_{\rm ex}^2\left(z\right) M_{\rm halo}}}. \tag{4.17}$$

Here s is the comoving distance from the center of a void and $R_{\rm halo} = CR_{\rm s}$ is the physical radius of the halo. Averaging over the impact parameter, p, gives

$$N_{\rm int}\left(z\right) = \frac{f\left(z\right) M_{\rm void}\left(z\right) R_{\rm halo}^2}{Y_{\rm void}^2 a_{\rm ex}^2\left(z\right) M_{\rm halo}}. \tag{4.18}$$

Note that the void radius $Y_{\rm void}$ is comoving while the halo radius $R_{\rm halo}$ is physical. Both these parameters are fixed and do not evolve with time. For example, for a void placed at redshift 0, $N_{\rm shell}\left(0\right) \simeq 0.4$.

4.4.2 One void

In this section we will focus on a single void at redshift 0.45 and a source at redshift 1. We calculate the expected number of halo intersections for a light ray from Eq. (4.18). For a 35 Mpc void, using the halo parameters from Section 4.2, we get $N_{\rm shell}\left(0.45\right) \simeq 0.8$. For $N = 10^4$ runs, we keep track of the number of

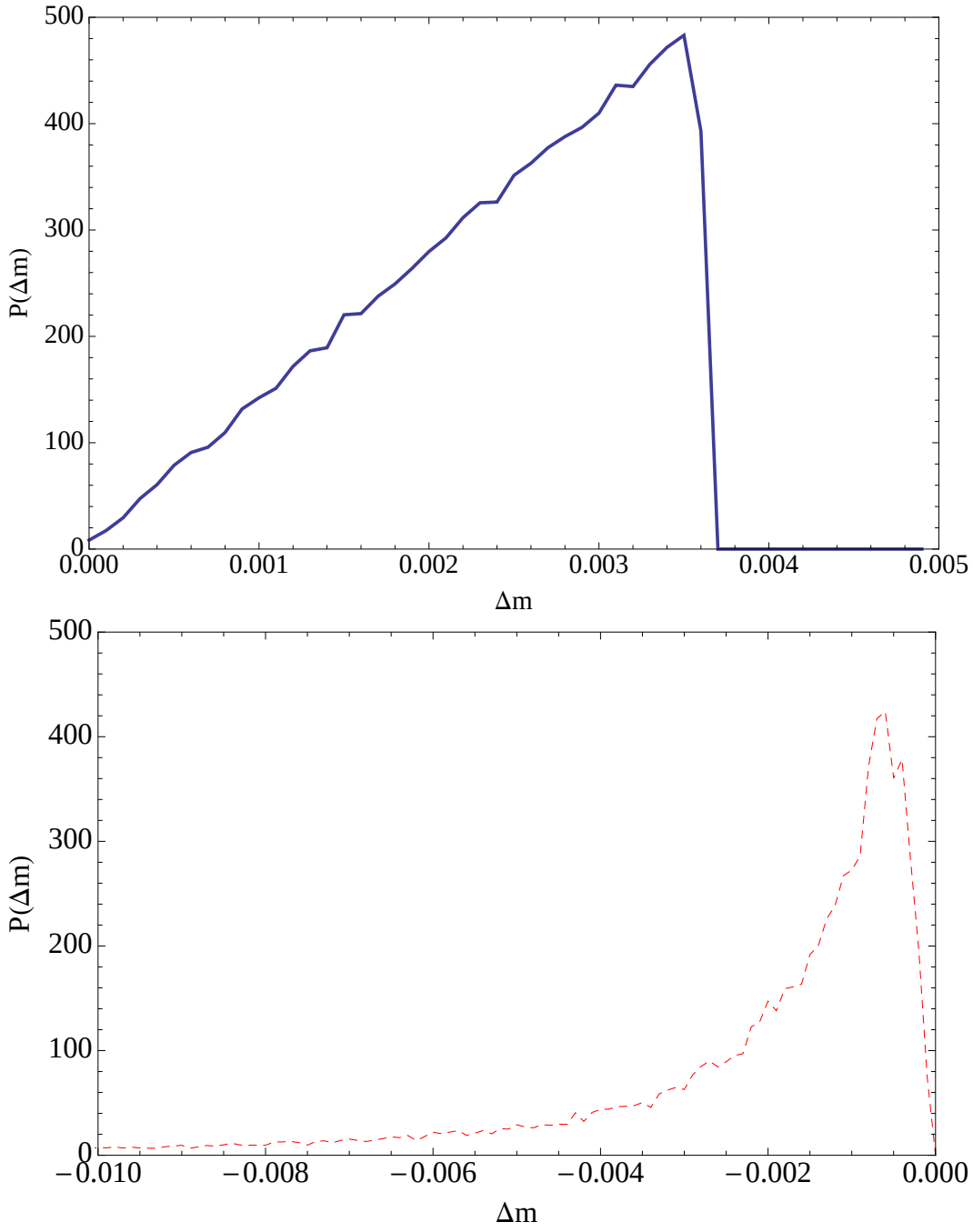

Figure 4.3: The probability distribution of magnitude shifts Δm for a simulation in the SRN model with $\Omega_M = 0.3$, with one void of radius 35 Mpc at $z = 0.45$ and sources placed at $z_s = 1$, and fraction of void mass on the shell today $f = 0.9$. Top: The probability distribution of magnitude shifts Δm for a single void for Δm positive. Bottom: The probability distribution for magnitude shifts Δm for a single void for Δm negative. The total probability for $\Delta m < 0$ is $\simeq 0.8$.

times that light rays hit halos and we obtain 8064 instances, which agrees well with our prediction. We use the density perturbation (4.4) for the SRN model and compute the lensing convergence κ by summing the result (4.11) over all intersected halos.

For the rest of the chapter, we will concentrate on the distribution of the magnitude shift Δm, which is a function of lensing convergence κ

$$\Delta m = \frac{2.5}{\ln 10} \ln \left| (1-\kappa)^2 - \gamma^2 \right| . \tag{4.19}$$

Here γ is the shear, which we will discuss in the next section. Figure 4.3 shows the probability distribution $P(\Delta m)$ of magnitude shifts Δm we obtain for a single void placed at $z = 0.45$ (without shear).

A notable feature of this distribution is that it is bimodal, with peaks at both positive and negative Δm (We plot separately the distribution for positive Δm and for negative Δm, since the relevant scales for these two regions of the probability distribution are very different). The peak at positive Δm is predominantly due to rays that do not intersect any halos, and are demagnified by their passage through the underdense void interior. The peak at negative Δm is predominantly due to rays which intersect one or more halos and are consequently magnified.

We can also compute the mean of each of these distributions and compare them with analytical expressions. The means for $\Delta m > 0$, $\langle \Delta m \rangle_+$ and for $\Delta m < 0$, $\langle \Delta m \rangle_-$ are defined to be

$$\langle \Delta m \rangle_+ = \int_0^\infty \Delta m P(\Delta m)\, d(\Delta m) , \tag{4.20}$$

$$\langle \Delta m \rangle_- = \int_{-\infty}^0 \Delta m P(\Delta m)\, d(\Delta m) . \tag{4.21}$$

We decompose the full distribution of magnification as a sum

$$P(\Delta m) = \sum_{n=0}^{\infty} \mathcal{P}_n P_n(\Delta m), \tag{4.22}$$

where $\mathcal{P}_n$ is the probability of n halo intersections and $P_n(\Delta m)\, d(\Delta m)$ is the probability of having a magnitude shift between Δm and $\Delta m + d(\Delta m)$ given that there are n intersections.

The analytic expression for the magnitude shift for zero halo intersections is [115]

$$\Delta m = 2.5 \log_{10} \left| (1 - \kappa_{\text{interior}})^2 \right|, \tag{4.23}$$

where

$$\kappa_{\text{interior}}(p) = -3 \frac{H_0^2}{c^2} \Omega_{\text{M}} f(z) \frac{y(y_S - y)}{y_{\text{S}} a_{\text{ex}}(z)} \sqrt{Y_{\text{void}}^2 - p^2}. \tag{4.24}$$

Here $f(z)$ is the fraction of the mass of the void on the shell, y is the comoving distance to the void, y_S is comoving distance to the source, $a_{ex}(z)$ is the scale factor and p is the comoving impact parameter. Note that for this one void case, essentially all the negative Δm contributions are due to intersections with one halo and the positive Δm contributions are due to the void interior (i.e., no halo intersections). In this approximation, Eqs. (4.20) and (4.21) reduce to

$$\langle \Delta m \rangle_+ \simeq \mathcal{P}_0 \int_{-\infty}^{\infty} \Delta m P_0(\Delta m)\, d(\Delta m) \tag{4.25}$$

and

$$\langle \Delta m \rangle_- \simeq \mathcal{P}_1 \int_{-\infty}^{\infty} \Delta m P_1(\Delta m)\, d(\Delta m). \tag{4.26}$$

We can compute $\mathcal{P}_0$ and $\mathcal{P}_1$ from Eq. (4.18) assuming $\mathcal{P}_0 + \mathcal{P}_1 = 1$ for the one void case, obtaining $\mathcal{P}_1 = 0.8$ and $\mathcal{P}_0 = 0.2$ which matches with our simulations. The numerically computed means (4.5) and (4.6) of the magnified and demagnified distributions agrees with their corresponding halo and void interior theoretical values [computed from Eqs. (4.12) - (4.13), (4.19) & (4.24)] to

$\sim 0.5\%$. We also numerically compute the mean lensing convergence obtaining -5×10^{-4} magnitudes with standard deviation 2×10^{-3} magnitudes. Thus the mean is consistent with zero as we would expect from a general theorem.

4.4.3 Shear

So far in our analysis we have not included shear. We can include it as follows. The matrix L^A_C for the j-th void defined in Eq. (2.15c) of [115] is

$$L_{AB} = -2 \int dy \left[\nabla_A \nabla_B \delta\Phi + \frac{1}{2} \left(\delta\Phi\right)_{,yy} \delta_{AB} \right]. \tag{4.27}$$

where $\delta\Phi$ is the potential perturbation, y is comoving distance, the derivatives are with respect to comoving coordinates, and the integral is taken over just the j-th void. We decompose L_{AC} into a trace part and a trace free part to obtain

$$L_{AB} = \frac{1}{w_j} \left[\kappa_j \delta_{AB} + \gamma_{jAB} \right], \tag{4.28}$$

where $w_j = y_j \left(y_S - y_j\right) / y_S$, y_j is the comoving distance to the j-th void, κ_j is the lensing convergence we computed previously [Eqs. (4.11) - (4.13) and (4.24)], and the matrix γ_j is traceless. We compute the potential perturbation from the density perturbations (4.3) and (4.4), and insert into Eqs. (4.27) and (4.28) to obtain the shear term γ_{jAB} which will be of the form $\gamma_j \epsilon_{AB}$ on a suitable choice of basis. For a single NFW halo the potential perturbation is

$$\delta\Phi\left(r\right) = -4\pi G \rho_0 R_s^2 \left[\frac{R_s}{r} \ln\left(1 + \frac{r}{R_s}\right) - \frac{1}{1+C} \right]. \tag{4.29}$$

The shear due to the void interior and the halos on the shell is

$$\gamma^A_B = \left(\gamma_{\text{void}}\right)^A_B + \sum_{i=1}^{N_{\text{shell}}} \left(\gamma^i_{\text{halo}}\right)^A_B, \tag{4.30}$$

where

$$(\gamma_{\rm void})^A_B = 3\frac{H_0^2}{c^2}\Omega_{\rm M} f(z)\,\frac{y(y_S-y)}{y_S a_{\rm ex}(z)}\,\frac{Y_{\rm void}}{\beta}\left(\delta^A_B - 2\hat{p}^A\hat{p}_B\right)$$
$$\left(\frac{2}{3} - \Theta(Y_{\rm void}-p)\left[\frac{2}{3}(1-\beta)^{3/2} + \beta(1-\beta)^{1/2}\right]\right), \tag{4.31}$$

and

$$\left(\gamma^i_{\rm halo}\right)^A_B = \frac{\delta^A_B - 2\hat{b}^A_i\hat{b}_{Bi}}{b_i^2}\Bigg[-4M_{\rm halo}$$
$$+16\pi\int_{b_i}^{CR_s} drr\rho_{\rm halo}(r)\,\sqrt{r^2-b_i^2} + 8\pi\int_{b_i}^{CR_s} drr\frac{\rho_{\rm halo}(r)}{\sqrt{r^2-b_i^2}}\Bigg]. \tag{4.32}$$

Here $\mathbf{p} = p\hat{p}^A\mathbf{e_A}$ is again the comoving impact parameter to the void, $\beta = p^2/Y^2_{\rm void}$ and $\mathbf{b}_i = b_i\hat{b}^A_i\mathbf{e_A}$ is the physical impact parameter of the light ray to the i-th halo. The first term in Eq. (4.32) is the point mass contribution of the halos. The second and third terms in Eq. (4.32) are non zero only for intersected halos. Evaluating the integrals using the NFW profile (4.1), we find that the intersected halo contribution $\left(\gamma^i_{\rm int}\right)^A_B$ is

$$\left(\gamma^i_{\rm int}\right)^A_B = \frac{16\pi G}{c^2}a_{\rm ex}(z)\rho_0 R_s\frac{y(y_S-y)}{y_S}\left(\delta^A_B - 2\hat{b}^A_i\hat{b}_{Bi}\right)\gamma_h. \tag{4.33}$$

Here for $\alpha < 1$

$$\gamma_h = \frac{1}{\alpha}\Bigg\{\frac{(2-\alpha)\sqrt{C^2-\alpha}}{2(\alpha-1)(C+1)} + \ln\left[\frac{C+\sqrt{C^2-\alpha}}{\sqrt{\alpha}}\right]$$
$$+\frac{(3\alpha-2)}{(1-\alpha)^{3/2}}\Bigg(\tanh^{-1}\left[\sqrt{\frac{1-\sqrt{\alpha}}{\sqrt{\alpha}+1}}\right]$$
$$-\tanh^{-1}\left[\frac{\sqrt{1-\alpha}}{C+1+\sqrt{C^2-\alpha}}\right]\Bigg)\Bigg\}, \tag{4.34}$$

and for $1 < \alpha < C^2$

$$\gamma_h = \frac{1}{\alpha}\Bigg\{\frac{(2-\alpha)\sqrt{C^2-\alpha}}{2(\alpha-1)(C+1)} + \ln\left[\frac{C+\sqrt{C^2-\alpha}}{\sqrt{\alpha}}\right]$$
$$-\frac{(3\alpha-2)}{(\alpha-1)^{3/2}}\Bigg(\tan^{-1}\left[\sqrt{\frac{\sqrt{\alpha}-1}{\sqrt{\alpha}+1}}\right]$$

$$- \tan^{-1}\left[\frac{\sqrt{\alpha - 1}}{C + 1 + \sqrt{C^2 - \alpha}}\right]\Bigg)\Bigg\}, \tag{4.35}$$

where $\alpha = b_i^2/R_s^2$.

From Eqs. (4.33) - (4.35), $\gamma^2 \sim 1/b^4$. Therefore contributions from shear are heavily suppressed. In our numerical analysis, the standard deviation changes by less than 3% if shear is neglected.

4.4.4 Qualitative features of magnification distributions

With the accuracy of our method tested, we now explore the magnification distributions in more general situations with many voids, distributed along the line of sight with random impact parameters according to the algorithm discussed in [115]. For example, for sources at redshift $z_s = 1$, there are 47 voids of comoving radius $Y_{\rm void} = 35$ Mpc along the line of sight. We follow steps 1 to 8 of Section IIC of our paper [115], but with the modification that the matrices **J**, **K**, **L** and **M** now incorporate the effects of the halo substructure of the shell.

In Figure 4.4, we plot the log of the magnification distribution for $z_s = 0.5$, 1.0 and 1.5. In our SRN model, we have voids with randomly distributed halos on their surface and a smooth interior. We denote by $\mathcal{P}_n$ the probability of having n halo intersections. The whole probability distribution can be decomposed into a sum of probability distribution for different numbers of halo intersections, like in Eq. (4.22). We plot the 25%, 50% and 75% quartiles of the distributions as horizontal lines (top, middle and bottom respectively). For high redshifts, most of the probability is concentrated in the demagnified areas where the rays hit only a few halos or simply pass through without hitting any.

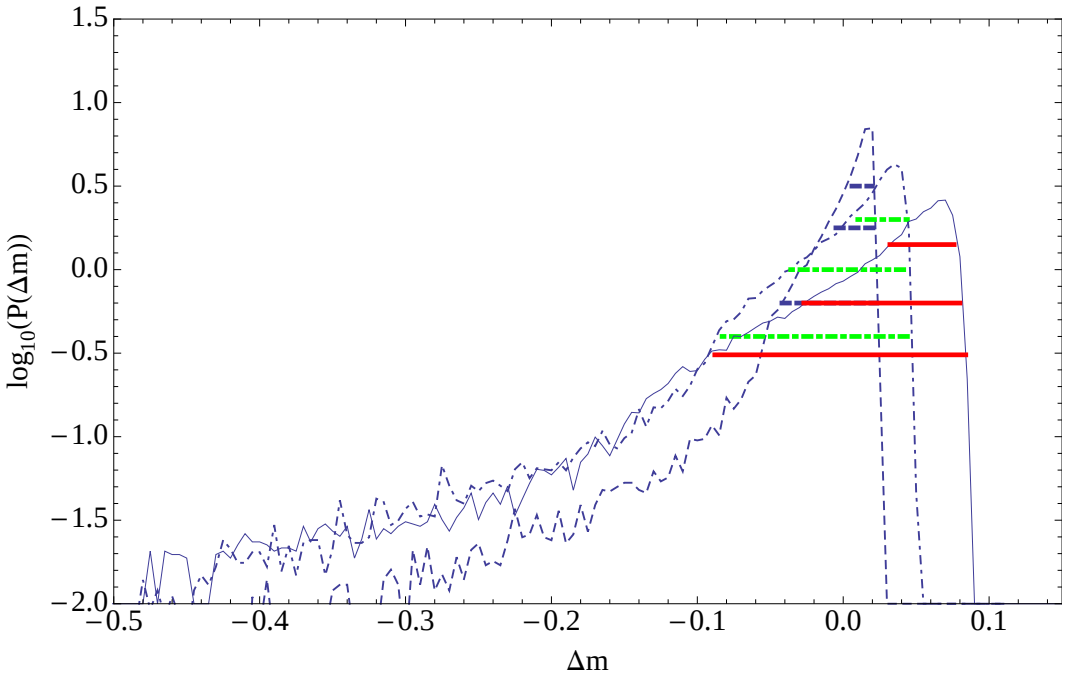

Figure 4.4: The probability distributions of magnitude shifts Δm for the SRN model with sources at redshifts of $z_s = 0.5$ (dashed), $z_s = 1.0$ (dot-dashed) and $z_s = 1.5$ (solid), for comoving voids of radius R = 35 Mpc with 90% of the void mass on the shell today. The horizontal lines are the 25% (top), 50% (middle) and 75% (bottom) quartiles about the peak of the distribution.

Note that the total probability in the tail on the magnification side ($\Delta m < 0$) increases with redshift, because of the increased probability of hitting halos at higher redshifts. For example, at $\Delta m = -0.2$, we would expect the probability density for $z_s = 1.5$ to be roughly 2-3 times as large as the probability density for $z_s = 0.5$ because the number of voids that rays have to pass through in the former case is 62 where as for the latter it is 27. In addition, rays at high redshifts have more close encounters with halos that generate shear.

Figure 4.5 shows the standard deviation of the distribution, σ_m, as a function of redshift of the source, z_s. This standard deviation for voids and halos is ~ 3 times larger at $z_s = 1$ than that for a model with mass compensated voids with a

shell thickness of 1 Mpc and no halos [1]. We note that most of the contribution to the standard deviation come from rays that intersect halos. Also, the standard deviation we compute agrees well with that computed using other methods. For example, our standard deviation for $z_s = 1.5$ is $\sigma_m = 0.072$, which agrees to within 20% with the standard deviation of the distribution shown in Figure 1 of Ref. [119]. We compare our results to those obtained using another method introduced in Refs. [125, 126] in the next subsection.

In Appendix B we derive the following approximate result for the standard deviation:

$$\sigma_m = \frac{5}{\log(10)} \left(\frac{\Omega_M}{2} \overline{g}_h \sum_j (H_0 Y_{\rm void} f_j) H_0^2 w_j^2 + \frac{\Omega_M^2}{2} \sum_j \frac{(H_0 Y_{\rm void} f_j)^2 H_0^2 w_j^2}{a_j^2} \right)^{\frac{1}{2}} . \tag{4.36}$$

Here $\overline{g}_h$ is a dimensionless parameter which represents the contribution from halos whose detailed form is given by Eq. (4.66), $Y_{\rm void}$ is the comoving radius of the voids, $f_j = f\left(z_j\right)$ is the fraction of the mass of j-th void on its surface and $a_j = a\left(z_j\right)$ is the scale factor. The result (4.36) assumes statistical independence of halos within voids and also of voids from one another and neglects lensing shear. There are two main qualitative features of the result (4.36). First, the contribution to the standard deviation due to the halos [the first term in Eq. (4.36)] depends primarily on their gravitational potential, and the contribution due to voids [the second term in Eq. (4.36)] depends primarily on the size of the underdense core. Second, the halo contribution is bigger than the interior contribution and hence the standard deviation is dominated by halos. For example, using the above expression, the ratio of the contribution due to the halos to the contribution due to the core is ~ 100 for $z_s = 1$ and for the void and halo parameters defined in Table II.

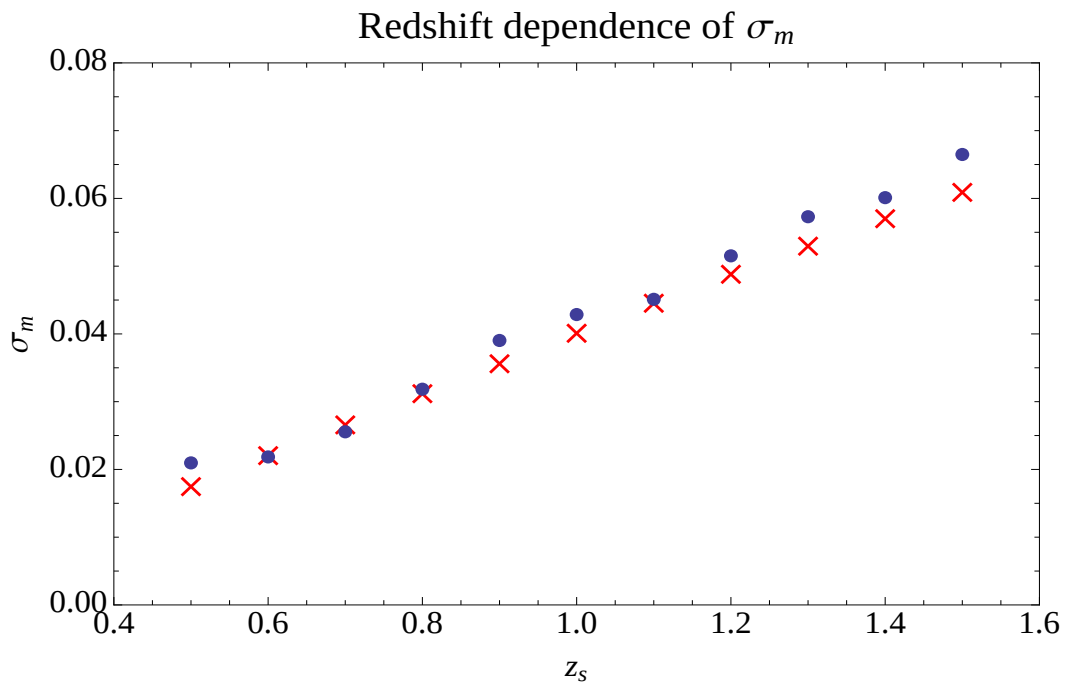

Figure 4.5: Redshift dependence of standard deviation of distribution of magnitude shifts, for comoving voids of radius R = 35 Mpc with 90% of the void mass on the shell today. The crosses are analytic results.

We discuss further the analytic calculation of standard deviation without shear in Appendix B. Our numerical results agree with these approximate analytic predictions to within ~ 20%.

4.4.5 Redshift dependence of mean and mode of magnitude shift

While the mean of lensing convergence vanishes, the mean magnitude shift does not, because magnitude shift is a nonlinear function of κ, defined in Eq. (4.19). Figure 4.6(top) shows the mean μ_m of the distribution of magnification shifts Δm, which increases with redshift as $\propto \sigma_m^2$. This is the expected theoreti-

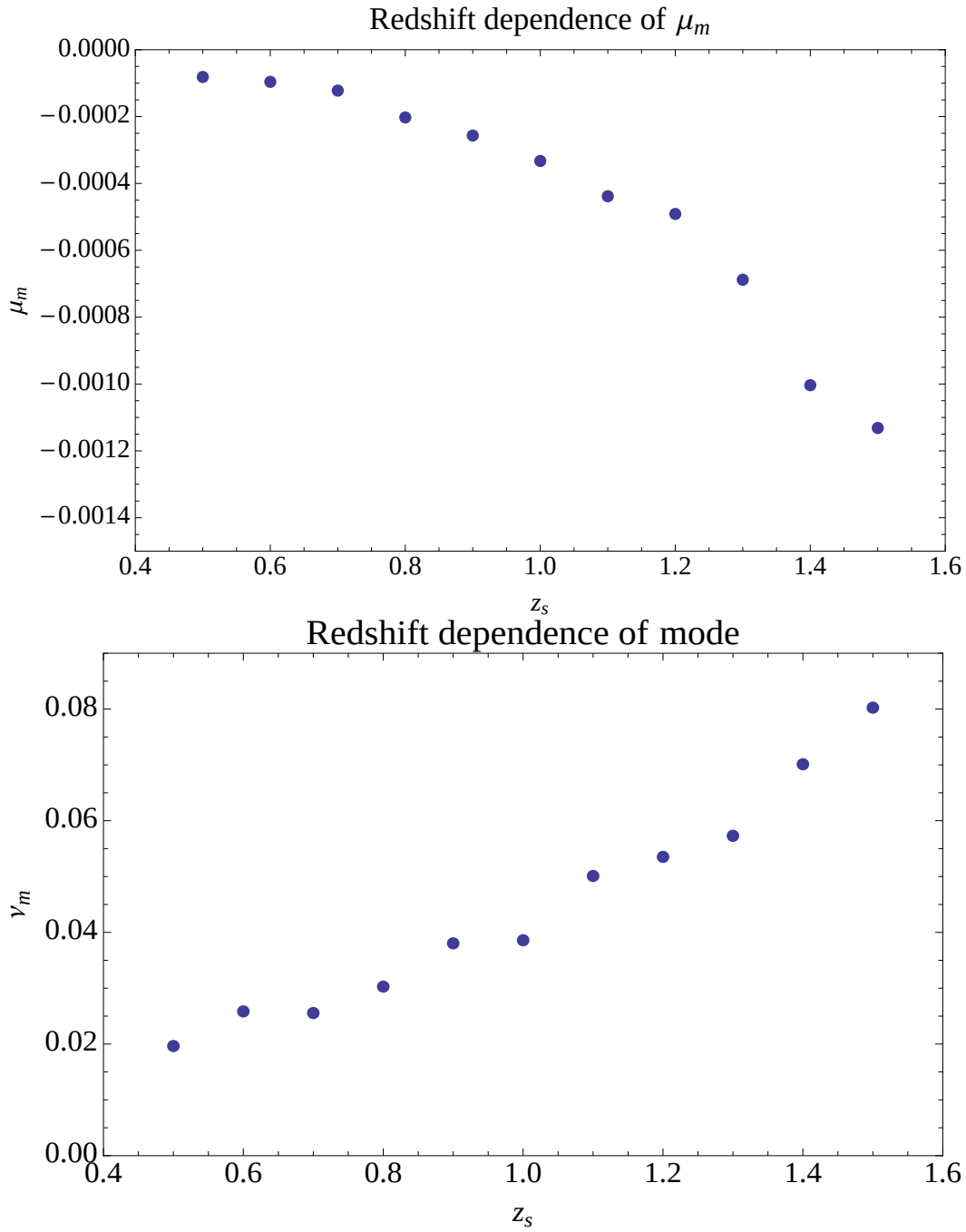

Figure 4.6: Plot of mean (top) and mode (bottom) of the distribution as a function of redshift in SRN. The mode takes on increasingly positive values with redshift and the mean is increasingly negative with redshift.

cal behavior: for small values of κ and ignoring shear, we can approximate Eq. (4.19) as

$$\Delta m \simeq \frac{5}{\ln 10} \ln|(1-\kappa)| \simeq \frac{5}{\ln 10}\left(-\kappa - \frac{1}{2}\kappa^2\right). \tag{4.37}$$

The mean magnitude shift is then proportional to the mean of the square of κ as the mean of κ is vanishing,

$$\mu_m \simeq -\frac{2.5}{\ln 10}\left\langle \kappa^2 \right\rangle. \tag{4.38}$$

The standard deviation, from Eq. (4.13) in [115] simplifies to

$$\sigma_m = \frac{5}{\ln 10}\sqrt{\langle \kappa^2 \rangle}, \tag{4.39}$$

and so $\mu_m \simeq -0.23\sigma_m^2$ which agrees with our numerical results to within $\sim 10\%$.

On average there is a small overall magnification of light beams. Figure 4.6 (bottom) shows the mode ν_m, the location of the maximum of the PDF, which also increases with redshift. The modes of the magnification to redshift 1.5 are positive because an overall demagnification occurs for most of the light rays as they pass through the interior of the voids while hitting halos. Note that the modes are larger than the corresponding means.

In realistic surveys, one can expect to find only a few standard candle sources for every redshift or every redshift bin. This severely constrains the accuracy of the cosmological parameters we can infer from such observations. To illustrate the extent of lensing degradation in measuring cosmological parameters, we pick 200 sets of randomly placed 10 or 100 sources at $z_s = 1.5$. We find the mean of each of these samples in the set and plot the resulting distribution of means in Figure 4.7 (top). The mean of the means for the 10 sources case is 0.011 magnitudes and the standard deviation of the means is 0.028 magnitudes. The respective numbers for the 100 sources case are 0.0004 and 0.011 magnitudes.

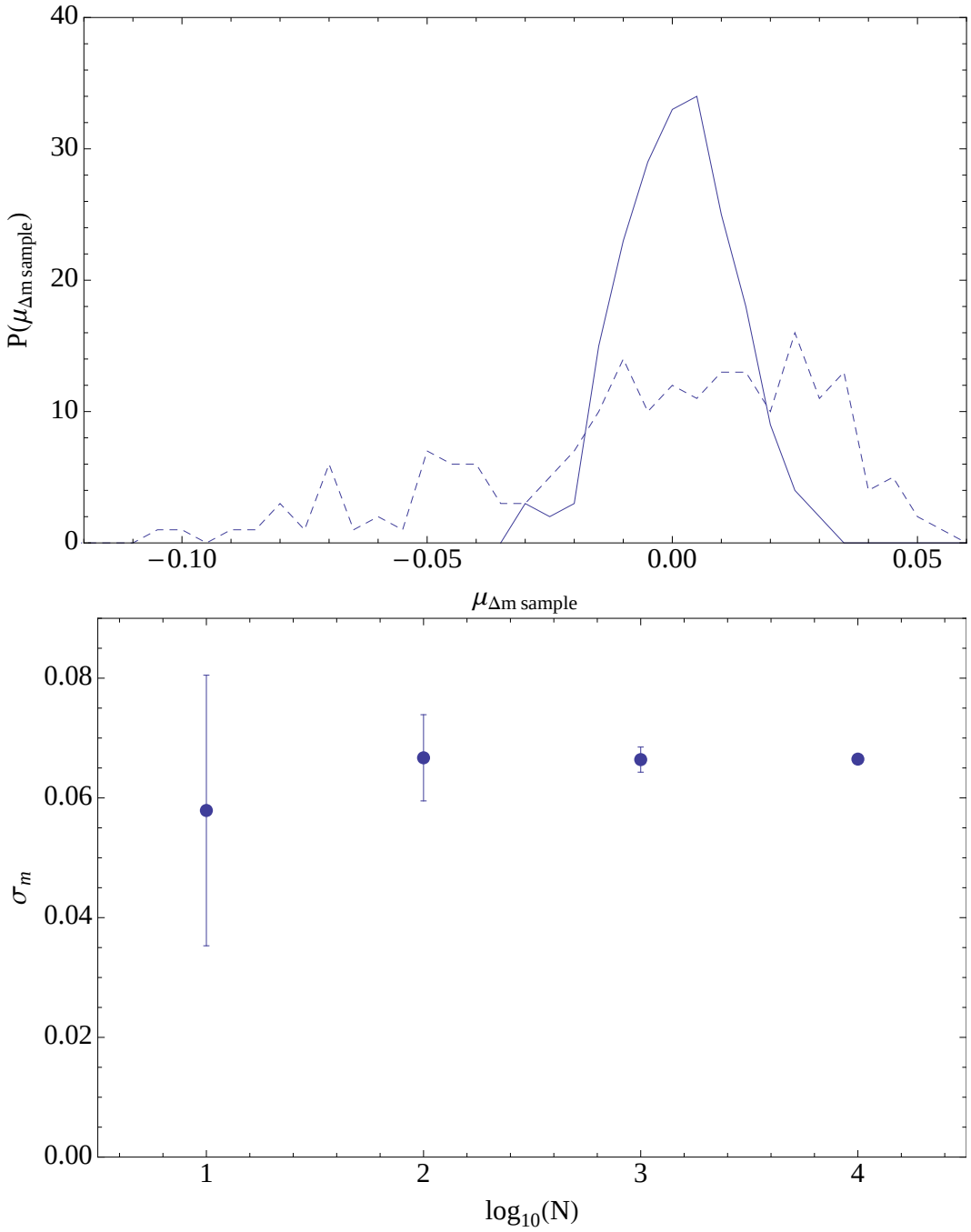

Figure 4.7: Top: Plot of distribution of means of 200 samples of 10 (dashed) and 100 (solid) sources each at redshift $z_s = 1.5$. The mean of the distribution of means is 0.011 magnitudes and the standard deviation is 0.028 magnitudes for the sample of 10. The respective numbers for the sample of 100 sources is 0.0004 and 0.011, showing that more sources reduces demagnification bias. Bottom: Plot of the range of standard deviation for samples of different sizes showing convergence as $N \to 10^4$.

A change in cosmological parameters by 1% implies a change in Δm of 0.015 magnitudes. Thus for data acquired from surveys, the lensing degradation is quite a significant effect, although it can be mitigated by increasing the number of sources. This is also seen in Figure 4.7 (bottom) where we plot the range of standard deviation for samples of different sizes. For a large enough sample, the bias in magnification can be accurately taken into account. This effect is studied in [119] which shows that lensing degradation effectively decreases the number of useful supernovae by a factor of 3 at source redshift 1.5.

Our work is broadly consistent with other work, [125, 126, 128, 129, 130, 131, 132, 133, 134, 135, 136] in this area. A similar computational method has been developed by Kainulainen & Marra, Refs. [125, 126]. Their model consists of filaments and halos of various sizes, where the mass fraction in filaments is 0.5 and the rest is distributed in halos. To compare with their results, we use the SRN model and choose parameters to match their cosmology, i.e., $\Omega_{\rm M} = 0.25$, $z_s = 1.5$, $H_0 = 73$ kms^{-1}Mpc^{-1} and $f = 0.5$. We do not include shear for this comparison as it is neglected in their analysis. Our magnification PDF qualitatively agrees with that of Kainulainen & Marra as shown in Figure 4.8.

4.5 Results for Swiss Raisin Raisin model

In our Swiss Raisin Raisin (SRR) model, in addition to replacing the smooth surface density on the shell with a collection of halos, the mass in the interior is also broken up into NFW halos with the same parameters as before. The parameters of the SRR model are listed in Table III.

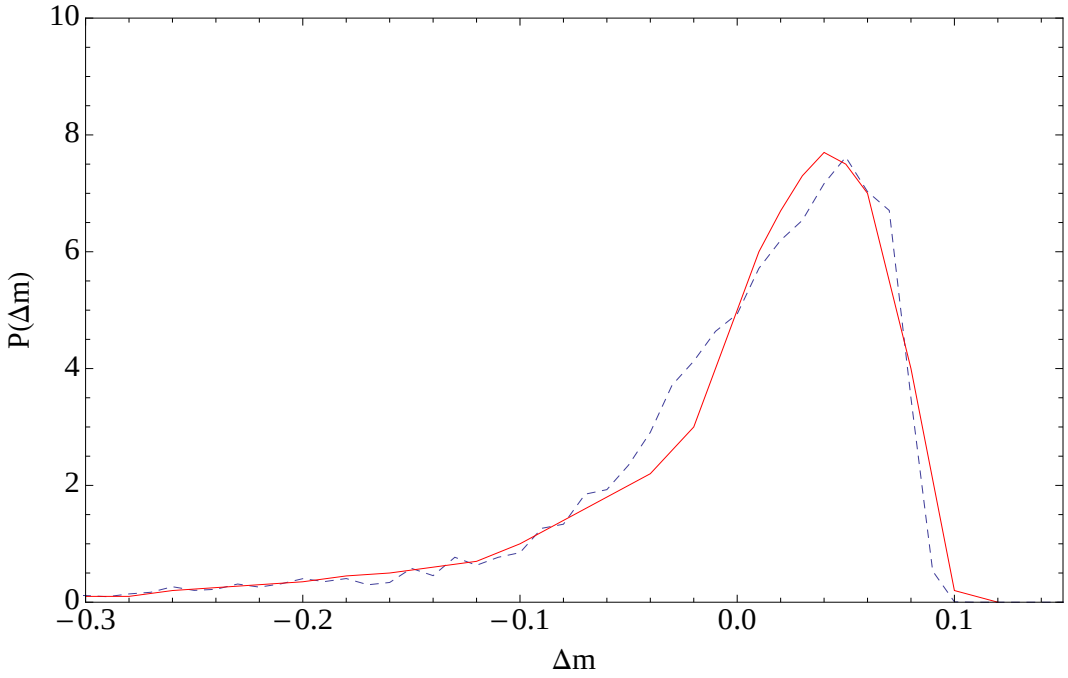

Figure 4.8: The probability distributions of magnitude shifts Δm for an SRN model (dashed lines) with sources at redshift $z_s = 1.5$, comoving voids of radius 35 Mpc, with 50% of the void mass in halos today, $\Omega_M = 0.25$, $\Omega_\Lambda = 0.75$, $H_0 = 73\,\mathrm{kms}^{-1}\mathrm{Mpc}^{-1}$ and with no shear, compared to the results in Figure 5 (we reproduced the plot by picking points from their figure) of the model in Kainulainen and Marra [126] where they have 50% of mass in halos and all other parameters same as ours. The two distributions are qualitatively similar.

Quantity	Value
Ω_M	0.3
Ω_Λ	0.7
H_0	$70\,\mathrm{kms}^{-1}\mathrm{Mpc}^{-1}$
Y_{void}	35 Mpc
Halo profile	NFW
Present fraction of void mass on shell	0.9
Fraction of shell mass in halos	1.0
Fraction of interior mass in halos	1.0

Table 4.3: Parameters of SRR model

4.5.1 A single void

In this section we focus on a single void with no shear. Again, we use Eqs. (4.4), (4.12) - (4.13) and (4.23) to compute the magnifications. For a 35 Mpc void and using the same halo parameters as in Section 4.2, the intersection probability remains about the same as in the previous model. The change due to the addition of a few halos in the vast interior region is negligible. The expected number of halo intersections $N_{\rm int}(z)$ is given by Eq. (4.18) with the shell mass replaced by the total void mass $M_{\rm void}$

$$N_{\rm int}(z) = \frac{M_{\rm void} R_{\rm halo}^2}{Y_{\rm void}^2 a_{\rm ex}^2(z)\, M_{\rm halo}} \tag{4.40}$$

Using the same parameters as in the one void case in the SRN model we obtain $N_{\rm int}(0.45) \simeq 0.88$. We find that light rays hit halos 8720 times for $N = 10^4$ runs which translates to an intersection probability of $\sim 88\%$ and agrees well with Eq. (4.40).

Again we find a bimodal distribution of magnitude shifts. In Figure 4.9, this bimodal distribution is superimposed on the SRN plots from Figure 4.3. Since the density contrast in the interior is increased by $\sim 10\%$ (if halos are not hit) compared to our SRN model, the demagnified distribution shifts towards the right. Figure 4.9 (top) shows this shift in underdense part of the distribution. Figure 4.9 (bottom) is the $\Delta m < 0$ part of the distribution. This accounts for roughly 88% of the total distribution and it is similar to the distribution in Figure 4.3 (bottom).

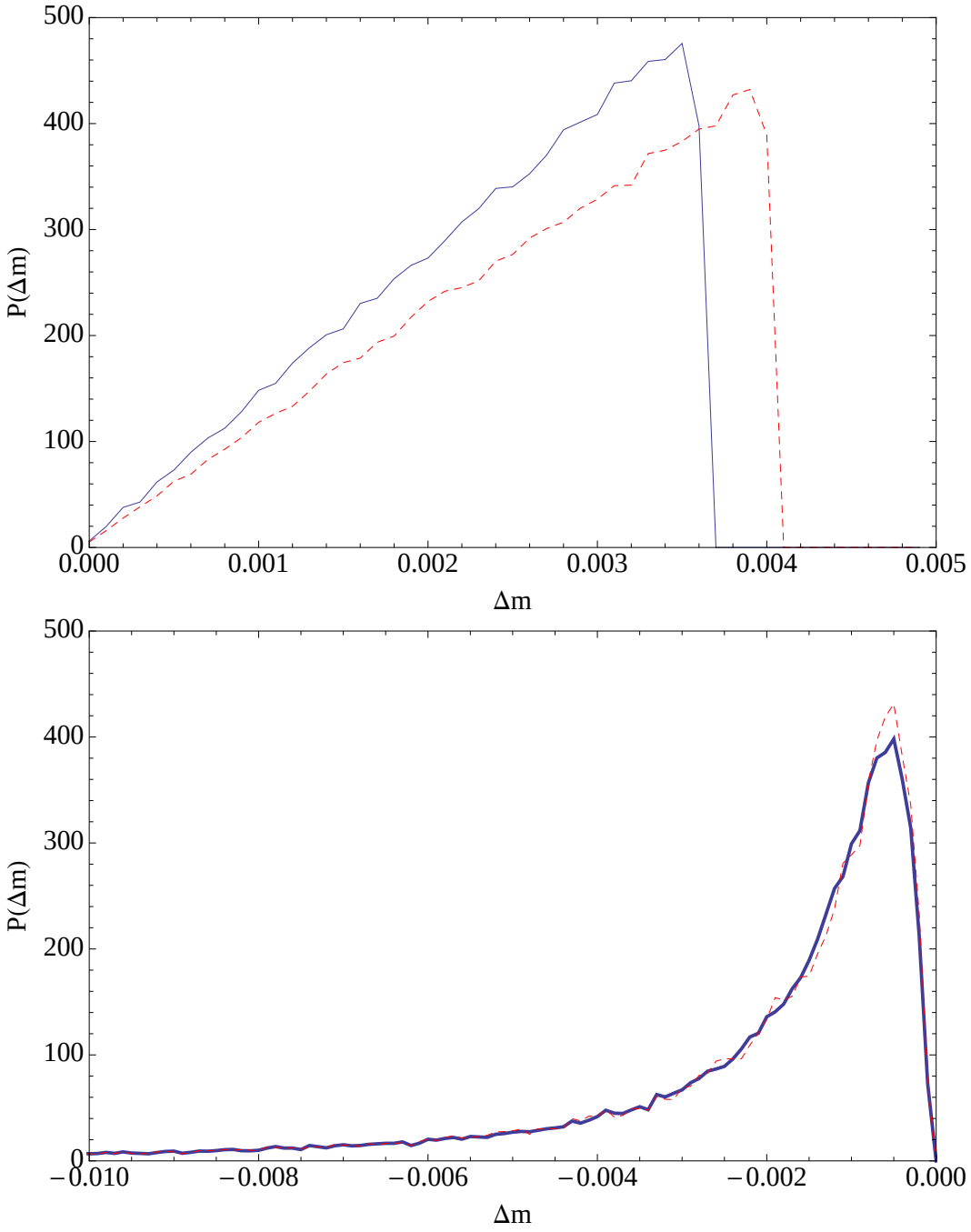

Figure 4.9: The probability distribution of magnitude shifts Δm for a simulation in the SRR model (dashed line) superimposed on the corresponding probability distribution in the SRN model (solid line) with $\Omega_M = 0.3$, with one void of radius 35 Mpc and fraction of void mass on the shell today $f = 0.9$. Note that the demagnified part, (top), is shifted because there is an increase in the density contrast in the interior of voids, while the magnified part, (bottom), is mostly unchanged.

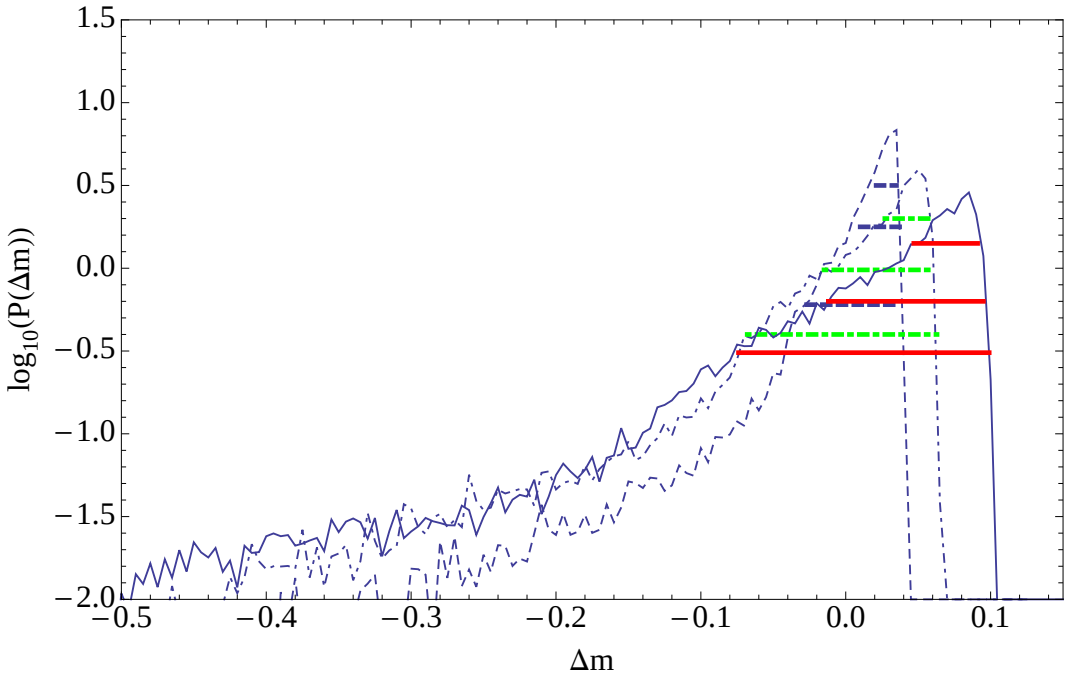

Figure 4.10: The probability distributions of magnitude shifts Δm for the SRR model with sources at redshifts of $z = 0.5$ (dashed), $z = 1.0$ (dot dashed) and $z = 1.5$ (solid), for voids of comoving radius R = 35 Mpc, with 90% of the void mass on the shell today. We see the same qualitative features as in SRN for the corresponding redshift but all the distributions are shifted towards demagnification. The horizontal lines are the 25% (top), 50% (middle) and 75% (bottom) quartiles of the distribution from the peaks.

4.5.2 Redshift dependence of distributions

Next we explore the bias (i.e., the mean of the distribution) due to halos and voids for sources at various redshifts, namely, for $z_s = 0.5,\ 1.0$ and 1.5. To compute the shear in this case, for the void contribution we use Eq. (4.24) but with $f(z) = 1$, and in Eqs. (4.33) - (4.35), we sum over both the surface and interior halos. The magnifications shown in Figure 4.10 are predominantly due to halos while the mostly empty interior has a demagnifying effect. Due to the increased underdensity inside the void, the magnitudes shift towards demagnification.

The standard deviation for $z_s = 1.5$ is $\sigma_m = 0.072$. Again we note that the modes are larger than the means and also shift towards the demagnification end of the plot with increasing redshift. The tails of these distributions are similar to the ones obtained in the SRN model in Figure 4.4.

Next we consider the mean magnitude shift, μ_m, and its mode, ν_m, in the two models. The key feature here is that the underdense interior is more prominent in the SRR model. We expect that the mean magnitude shift and its mode should shift and the difference in the means should increase with redshift. In Figure 4.11, we plot the means and modes for the two models and we show that μ_m for SRR is $\sim 10 - 20\%$ greater than that for SRN at $z_s = 1$.

These two models are interesting because they represent the two possible extremes of the matter distribution in voids - one where the matter is smoothly distributed with no structure and another with only chunky NFW halos. In reality, the underdense region will be composed of both halos and an ambient intergalactic medium. By studying the completely smooth interior case (SRN) and the completely granular interior case (SRR), we expect to bracket the true distribution.

4.5.3 Effect of large scale structure

Previous studies in the literature have modeled the magnification effects of only voids [115, 121, 124] or only halos [117, 119, 125], while other studies have considered very specific models with a particular distribution of filaments and halos [126]. In our work, we present two models that incorporate the effects of both halos and voids. We have considered cosmological models where at large

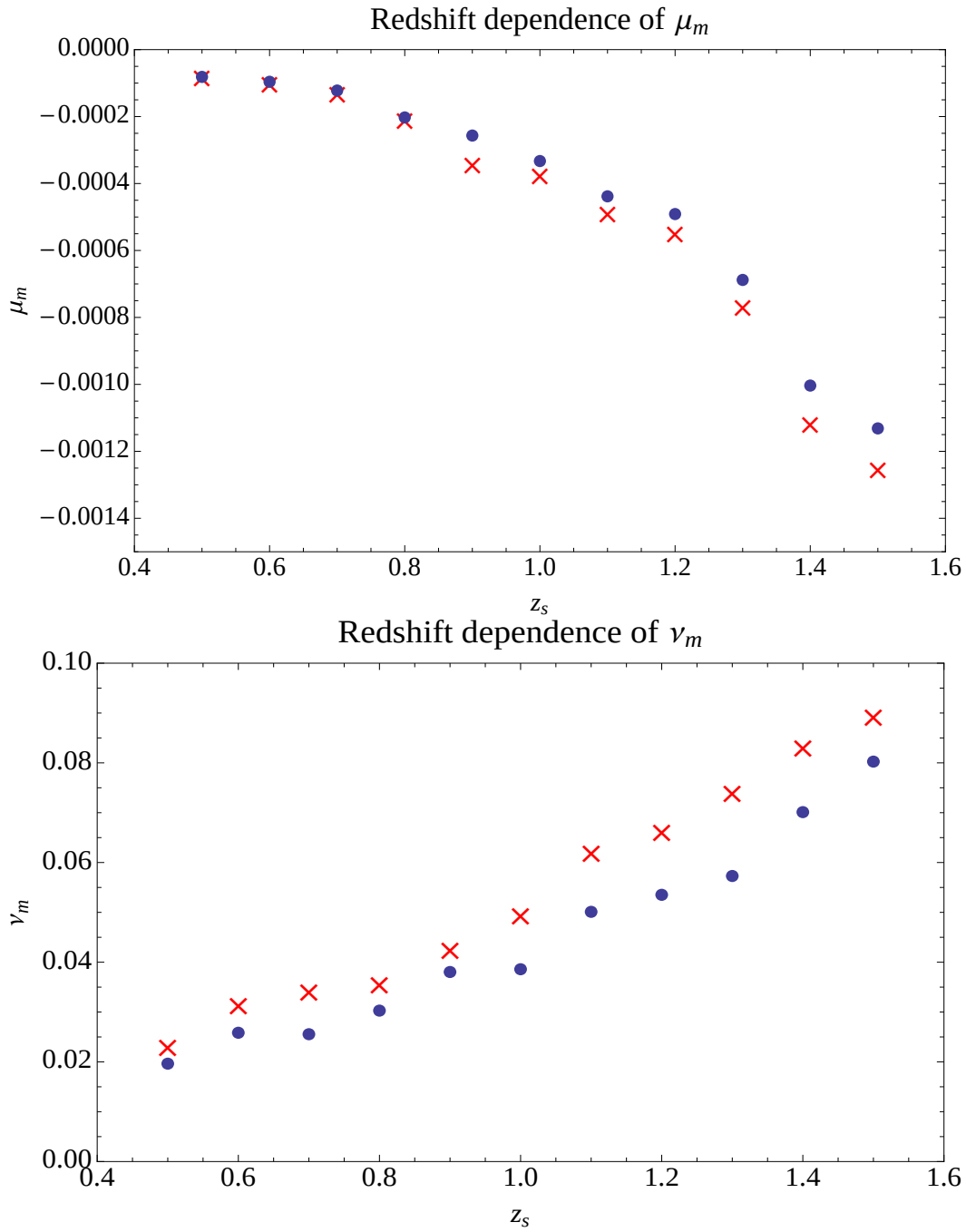

Figure 4.11: The mean and mode of magnification shift for the two models - Points: SRN; Crossed points: SRR. Top: The mean of magnification shift, μ_m, for the two models. We see that the difference in the means increases with redshift and at $z = 1$ and it is $\sim 10\%$. Bottom: The mode of magnification shift, ν_m, for the two models. We see that the difference in the means increases with redshift and at $z = 1$ and it is $\sim 20\%$.

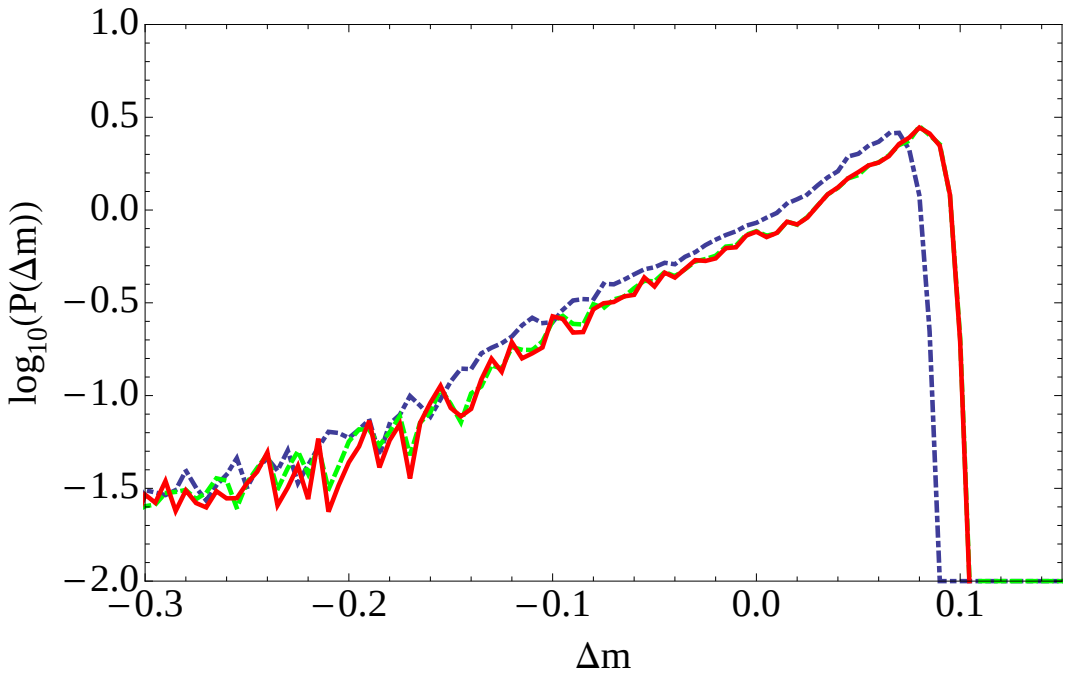

Figure 4.12: The probability distributions of magnitude shifts Δm for simulations in SRR (solid), the SRN model (dot dashed), for comoving voids of radius R = 35 Mpc with $f = 0.9$ today. Also shown is the model with uniformly distributed halos everywhere and with no voids (dashed - this is the $f = 0$ limit of the SRR model) with source at redshifts of $z = 1.5$. The distributions are similar in the SRR models because the expected number of halos intersected is independent of of the radial distribution of halos, where as the distribution in the SRN model is qualitatively similar but is shifted towards negative magnifications.

scales matter evolves to cluster on the edges of spherical voids.

One limit of our model is the case where there are no halos on the surface and the interior is composed entirely of halos. This corresponds to the $f = 0$ limit of the SRR model, a "no void limit". In Figure 4.12, we compare the magnification distribution we obtain for this configuration for $z_s = 1.5$ to the corresponding distribution in the SRR and SRN models, for comoving voids of radius R = 35 Mpc with 90% of the void mass on the shell today. From Eq. (4.40),

the expected number of halo intersections in the SRR model is independent of the radial distribution of the halos and hence the SRR and no void distributions should be similar, as observed. However, in the SRN model the number of halo intersections is lower due to the smaller number of halos. Hence the distribution is shifted towards negative magnification shifts.

4.6 Conclusions

In this chapter, we presented two simple models to study the effects of both voids and halos on distance modulus shifts due to gravitational lensing. Our results may be useful for future surveys that gather data on luminosity distances to various astronomical sources to constrain properties of the source of cosmic acceleration. The core of our model is constructed by considering a ΛCDM Swiss cheese cosmology with mass compensated, randomly located voids, while our small scale halo structures are non-evolving and chosen to be all the same size and with an NFW matter profile.

We used an algorithm, described in [115], to compute the probability distributions of distance modulus shifts. The mean dispersion of the magnitude shift due to gravitational lensing due to voids and halos is ~ 3 times larger than due to voids alone with a shell thickness, [115]; the dispersion σ_m due to 35 Mpc voids and halos for sources at $z_s = 1.5$ is $\sigma_m = 0.065 - 0.072$ (depending on the model). The mean magnitude shift due to voids and halos is of order $\delta m = -0.0010$ to -0.0013 (depending on the model). These values of σ_m imply that large scale structure must be accounted for in using luminosity distance determinations for estimating precise values of cosmological parameters, such as

those characterizing the dark energy equation of state.

We studied the distribution of magnitude shifts for three different source redshifts in each of our models. The qualitative dependence on redshift is similar to that of the previous void-only models [115]. We find that the voids do not significantly change the variance but do significantly change the demagnification tail and the mode. The mode lies on the demagnification side and the variance is largely due to halo intersections. The scale of voids is unimportant and the only discernable effect in the mode is seen when the void interior is smoothly distributed matter. As a result, our models bracket the range of possibilities of magnifications.

Our simple and easily tunable model for void and galaxy halo lensing can be used as a starting point to study more complicated effects. For example, one can use various algorithms to generate realizations of distributions of non-overlapping spheres in three dimensional space. Given such a realization one could use the algorithm of this chapter to study correlations between magnifications along rays with small angular separations, which would be relevant to future small beam surveys [137]. Finally, our model is in general agreement with other simplified lensing models in the literature that focus on lensing due to both halos and larger scale structures, [126, 128, 129, 130, 131, 132, 133, 134, 135, 136].

Our results for σ_m in the SRN void model are represented within about 20% by an analytic model presented in detail in Appendix B. This model ascribes the magnitude shift entirely to the fluctuations in light beam convergence that results from passage through underdense cores and overdense halos; thus it ignores the contribution from shear, which we have found to be relatively small

empirically. The final result for σ_m^2 is a sum of these two contributions. [See Eqs. (4.65) and (4.67)]. Although our simulations assumed a single halo mass M_h, radius R_h and concentration C, and a single void radius, the analytic model allows distributions for these key quantities. The contribution from halos is proportional to a suitably weighted mean of $M_h \Psi_2(C_h)/R_h^2$, where $\Psi_2(C_h)$ is defined in Eq. (4.61) and is displayed in Fig. 13. The contribution from the underdense void cores is proportional to the mean void radius. Typically, the contribution to σ_m^2 from halos is much larger than the contribution from void cores so σ_m^2 is larger for more massive or more compact halos.

We have seen that the results of our simulations depend on whether the underdense core consists of smoothly distributed dark matter (SRN) or is itself clumped into halos (SRR). In the extreme case in which the underdense core is entirely made of halos, the results do not depend on the core density, and is equivalent to the SR model that consists of halos distributed randomly within a void.

Although the analytic model was only developed for the SRN model, it could also be applied to the SRR model with any prescription for the fraction of the mass of the underdense core that is clumped into halos. For example, in the extreme case of total clumping we can use the analytic models in Appendix B with the substitution $f = 1$ for all z in all expressions derived there. For intermediate cases, a prescription for the fraction of the underdense core that remains smooth rather than clumped would be needed.

This research was supported at Cornell by NSF grants PHY-0968820 and PHY-1068541 and by NASA grant NNX11AI95G.

4.7 Appendix A: Column Depth

In this appendix, we describe how we calculate the column density encountered by rays passing through halos in the SRN model. In our model for the voids, we break up the bounding shell of mass into halos with mass $M_{\rm halo}$. As a light ray passes through one of these halos, the beam will acquire some integrated column depth, $\eta = \int \rho(z)\, dz$, where the random variable η depends on the impact parameter of the beam with respect to the halo center, $\rho(z)$ is the density profile of the halo and y is the physical coordinate. The maximum value is for a beam going right through the center, and diverges for our NFW profile 4.1.

We use an NFW profile 4.1, for the matter distribution in halos, and the column depth is

$$\eta(b) = (2\rho_0 R_{\rm s}^3) \int_0^{\sqrt{(CR_{\rm s})^2 - b^2}} \frac{dz}{\sqrt{z^2+b^2}\left(\sqrt{z^2+b^2}+R_{\rm s}\right)^2} \tag{4.41}$$

where we have changed from radial (in Eq. (4.1)) to Cartesian coordinates. Here the physical impact parameter is b and C is the ratio of the radius of the halo to its core radius. This reduces to the sum of two contributions

$$\eta_{\rm halo}(b) = \eta_{\rm core}\Theta(R_{\rm s}-b) + \eta_{\rm out}\Theta(b-R_{\rm s})\,\Theta(CR_{\rm s}-b) \tag{4.42}$$

where the relationship between the column depth $\eta(b)$ and the corresponding lensing convergence, $\kappa(b)$, is, from Eq. (3.1),

$$\eta(b) = \left(\frac{4\pi G a_{\rm ex}(z)}{c^2}\frac{y(y_{\rm S}-y)}{y_{\rm S}}\right)^{-1}\kappa(b)\,. \tag{4.43}$$

The lensing convergences is listed in Eqs. (4.12) and (4.13). Again, the contribution from outside a radius of $CR_{\rm s}$ is zero. The mean column density of halos is defined as

$$\eta_{\rm halo} = \frac{M_{\rm halo}}{\pi(CR_{\rm s})^2}. \tag{4.44}$$

For the halos, even more important that η is $d\eta/d\alpha$, where $\alpha = b^2/R_s^2$; this is because the probability distribution for α is $d\alpha/C^2$, and therefore the probability distribution for η for a single halo is

$$P_{\rm halo}(\eta) = \frac{1}{C^2 \left| d\eta_{\rm halo}/d\alpha \right|}. \tag{4.45}$$

This is the quantity plotted in Figure 4.1.

4.8 Appendix B: Analytic Estimate of Standard Deviation

In this appendix, we derive analytic results for the standard deviation of magnifications. Consider the mean of the contribution to the convergence (3.1) from the underdense core of the j-th void, which we will denote by $\kappa_{c,j}$. We find

$$\kappa_{c,j} = -\frac{3H_0^2\Omega_M}{2} \times \frac{f_j y_j (y_S - y_j)}{a_j y_S} \times 2\sqrt{Y_j^2 - p_j^2} \tag{4.46}$$

where Y_j is the comoving radius of the void, a_j is the scale factor and f_j is the fraction of the total void mass on the surface at redshift z_j. After averaging over impact paramters we obtain

$$\langle \kappa_{c,j} \rangle = -2\Omega_M H_0 Y_j \frac{f_j H_0 y_j (y_S - y_j)}{a_j y_S}, \tag{4.47}$$

and therefore the net expected convergence from voids is

$$\langle \kappa_c \rangle = \sum_j \langle \kappa_{c,j} \rangle = -2\Omega_M H_0 \sum_j \frac{f_j Y_j H_0 y_j (y_S - y_j)}{a_j y_S}\ . \tag{4.48}$$

Assuming a typical radius $Y_j \sim Y_{\rm void}$, there are about $(H_0 Y_{\rm void})^{-1}$ terms in the sum, and consequently the overall average is $\sim \Omega_M$. In the limit that there are many voids along a given line of sight, we can replace the sum by an integral. The

number of voids per interval dy of comoving distance is $dy/2R$, and therefore if we define $\xi = H_0 y$ we find

$$\langle \kappa_c \rangle = -2\Omega_M H_0 \sum_j \frac{f_j R_i H_0 y_j (y_S - y_j)}{a_j y_S}$$

$$\rightarrow -\Omega_M \int_0^{\xi_S} \frac{d\xi f(\xi)\xi(\xi_S - \xi)}{a(\xi)\xi_S} \,, \tag{4.49}$$

where $\xi_S = H_0 y_S$. Equation (B4) does not depend on any void properties (apart from the value of f today) and remains valid if there is a distribution of void sizes, for example.

On average, the contribution κ_h from halos to the lensing convergence must cancel the contribution (B4) from voids, i.e., $\langle \kappa_h \rangle = -\langle \kappa_c \rangle$.

We assume statistical independence of halos within voids from the core (i.e., true if halo radii are small) and also of voids from one another. The overall variance is a sum of individual halo and core variances. As in our simulations, we neglect clustering of halos, which would introduce correlations among them, and assume that dark matter is confined to the halos and underdense core. These assumptions could be relaxed in a more sophisticated model. We see that

$$\langle \kappa_c^2 \rangle - \langle \kappa_c \rangle^2 = \sum_j \langle \kappa_{c,j}^2 \rangle - \langle \kappa_{c,j} \rangle^2$$

$$= \frac{1}{2}\Omega_M^2 H_0^2 \sum_j \frac{Y_j^2 f_j^2 H_0^2 y_j^2 (y_S - y_j)^2}{a_j^2 y_S^2} \tag{4.50}$$

since the averages for $i \neq j$ vanish. The sum is $\lesssim (H_0 Y)^{-1}$ and therefore $\langle \kappa_c^2 \rangle \lesssim \Omega_M^2 H_0 Y$.

Let us now consider halos residing in void j. We include the possibility that there are different types of halo with different properties, and label the types by

α. For a given halo i of type α passed through by the line of sight at physical impact parameter $b_{\alpha,i}$ relative to its center, the contribution to κ_h is

$$\kappa_{(\alpha,i),j} = \frac{8\pi G a_j y_j (y_S - y_j)}{y_S} \int_{b_{\alpha,i}}^{R_{h,\alpha}} \frac{dr\, r\, \rho_\alpha(r)}{\sqrt{r^2 - b_{\alpha,i}^2}} \tag{4.51}$$

where $R_{h,\alpha}$ is the physical halo radius, and $\rho_\alpha(r)$ is the physical density within the halo. The average over impact parameters $b_{\alpha,i}$ is

$$\begin{aligned} &\frac{2}{R_{h,\alpha}^2} \int_0^{R_{h,\alpha}} db_{\alpha,i} b_{\alpha,i} \int_{b_{\alpha,i}}^{R_{h,\alpha}} \frac{dr\, r\, \rho_\alpha(r)}{\sqrt{r^2 - b_{\alpha,i}^2}} \\ &\qquad = \frac{M_{h,\alpha}}{2\pi R_{h,\alpha}^2} \,, \end{aligned} \tag{4.52}$$

where $M_{h,\alpha}$ is the total halo mass. Therefore the average over impact parameters through a given halo is

$$\langle \kappa_{(\alpha,i),j} \rangle = \frac{4G M_{h,\alpha} a_j y_j (y_S - y_j)}{R_{h,\alpha}^2 y_S} \,. \tag{4.53}$$

If all of the halos reside in the voids (i.e., none in the FRW exterior), then the expected number of intersections of the light path with a halo is $N_{\alpha,j} R_{h,\alpha}^2 / a_j^2 Y_j^2$, where $N_{\alpha,j}$ is the expected number of halos of "type α" in the void, and we take account of the fact that $R_{h,\alpha}$ is a physical radius. Then we get a total contribution from halos per mass-compensated void equal to

$$\sum_\alpha \frac{N_{\alpha,j} R_{h,\alpha}^2 \langle \kappa_{(\alpha,i),j} \rangle}{a_j^2 Y_j^2} = \frac{4G y_j (y_S - y_j)}{a_j Y_j^2} \sum_\alpha N_{\alpha,j} M_{h,\alpha} \,; \tag{4.54}$$

the sum is the total mass in halos, which must compensate the underdensity, so

$$\sum_\alpha N_{\alpha,j} M_{h,\alpha} = \frac{f_j H_0^2 \Omega_M Y_j^3}{2G} \tag{4.55}$$

and therefore

$$\sum_\alpha \frac{N_{\alpha,j} R_{h,\alpha}^2 \langle \kappa_{h,\alpha} \rangle}{a_j^2 Y_j^2} = \frac{2 f_j H_0^2 \Omega_M Y_j y_j (y_S - y_j)}{a_j y_S} = -\langle \kappa_{c,j} \rangle \,. \tag{4.56}$$

Therefore the average per mass-compensated void cancels as expected. This cancellation is actually independent of the distribution of halos within the void but depends on the assumption that all halos are associated with voids.

Let us suppose that

$$\kappa_{(\alpha,i),j} = \frac{4GM_{h,\alpha}a_\alpha y_j(y_S - y_j)}{R_{h,\alpha}^2 y_S} F_\alpha\left(\frac{b_{\alpha,i}^2 C_{h,\alpha}^2}{R_{h,\alpha}^2}\right) \tag{4.57}$$

where $C_{h,\alpha}$ is dimensionless. This form assumes that the density profile for halo type α has one scale parameter, $R_{h,\alpha}/C_{h,\alpha}$, although it does not necessarily assume that the density profiles are the same for all halos either in form or in the parameter $C_{h,\alpha}$. We do assume that

$$\int_0^1 dx\, F_\alpha(xC_{h,\alpha}^2) = 1 = \frac{1}{C_{h,\alpha}^2}\int_0^{C_{h,\alpha}^2} dq\, F_\alpha(q), \tag{4.58}$$

independent of the value of $C_{h,\alpha}$. With this normalization, if we let $\rho_\alpha(r) = \rho_{0,\alpha}\hat{\rho}_\alpha(rC_{h,\alpha}/R_{h,\alpha})$ we find

$$\begin{aligned} &F_\alpha\left(\frac{b_{\alpha,i}^2 C_{h,\alpha}^2}{R_{h,\alpha}^2}\right) \\ &= \frac{2\pi\rho_{0,\alpha}R_{h,\alpha}^3}{M_{h,\alpha}C_{h,\alpha}} \int_{b_{\alpha,i}C_{h,\alpha}/R_{h,\alpha}}^{C_{h,\alpha}} \frac{du\, u\,\hat{\rho}_\alpha(u)}{\sqrt{u^2 - b_{\alpha,i}^2 C_{h,\alpha}^2/R_{h,\alpha}^2}}\,. \end{aligned} \tag{4.59}$$

Equation (4.57) with the normalization (4.58) leads to Eq. (4.56) as expected, but it also implies contributions from each halo to the variance given by

$$\begin{aligned} \kappa_{(\alpha,i),j}^2 - \langle\kappa_{(\alpha,i),j}\rangle^2 &= \left[\frac{4GM_{h,\alpha}a_\alpha y_j(y_S - y_\alpha)}{R_{h,\alpha}^2 y_S}\right]^2 \\ &\times\left\{\left[F_\alpha\left(\frac{b_{\alpha,i}^2 C_{h,\alpha}^2}{R_{h,\alpha}^2}\right)\right]^2 - 1\right\}\,. \end{aligned} \tag{4.60}$$

Averaging over impact parameters implies

$$\langle\kappa_{(\alpha,i),j}^2\rangle - \langle\kappa_{(\alpha,i),j}\rangle^2$$

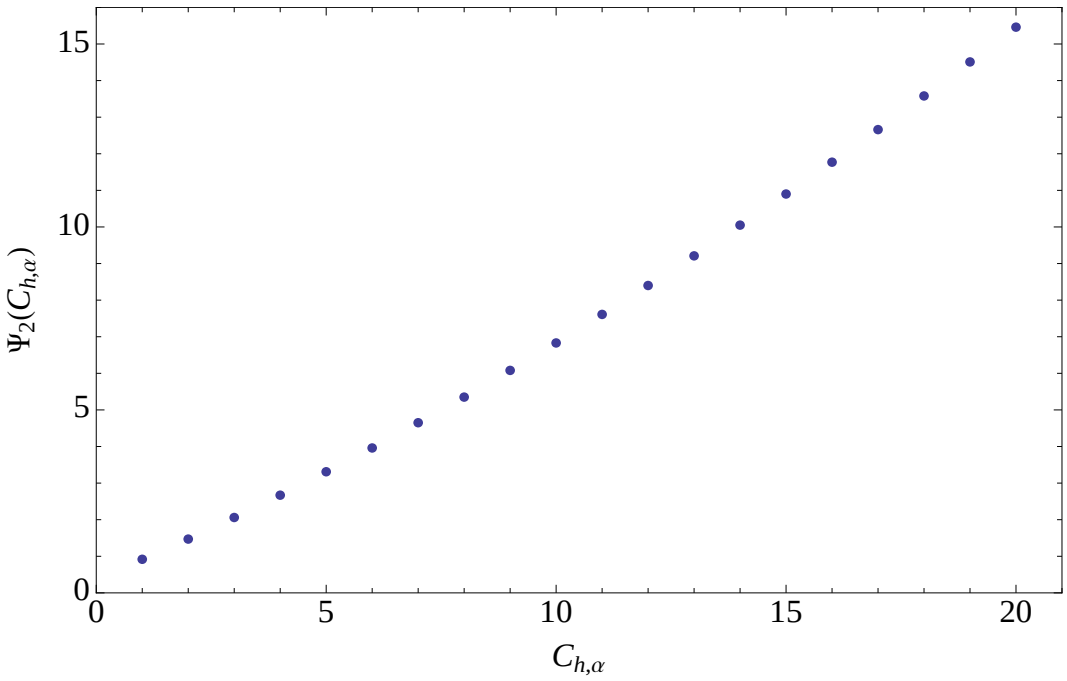

Figure 4.13: Plot of the behavior of $\Psi_2(C_{h,\alpha})$ as a function of the concentration parameter $C_{h,\alpha}$ of NFW halos.

$$= \left[\frac{4GM_{h,\alpha}a_\alpha y_j(y_S - y_\alpha)}{R_{h,\alpha}^2 y_S}\right]^2 \left[\int_0^1 dx\, F^2(xC_{h,\alpha}^2) - 1\right]$$

$$= \left[\frac{4GM_{h,\alpha}a_\alpha y_j(y_S - y_\alpha)}{R_{h,\alpha}^2 y_S}\right]^2 \Psi_2(C_{h,\alpha})\,. \tag{4.61}$$

where the function $\Psi_2(C_{h,\alpha})$ for NFW profiles is plotted in Figure 4.13.

We can use these results to determine the expected contribution of halos in a given mass-compensated void to the variance. Since total mass in halos in void j is $f_j\Omega_M H_0^2 R_j^3/2G$, if the fraction of this total in halos of type α is $\eta_{\alpha,i}$, then expected number of type α is

$$N_{\alpha,j} = \frac{\eta_{\alpha,i} f_j \Omega_M H_0^2 Y_j^3}{2GM_{h,\alpha}}.B17 \tag{4.62}$$

The expected number of intersections with type α is

$$\nu_{\alpha,j} = \frac{\eta_{\alpha,i} f_j \Omega_M H_0^2 Y_j R_{h,\alpha}^2}{2a_j^2 GM_{h,\alpha}}. \tag{4.63}$$

The contribution from halos in mass-compensated void j to the total variance is therefore

$$\frac{8 f_j G \Omega_M H_0^2 Y_j y_j^2 (y_S - y_j)^2}{y_S^2} \sum_\alpha \frac{\eta_{\alpha,i} M_{h,\alpha} \Psi_2(C_{h,\alpha})}{R_{h,\alpha}^2} \,. \tag{4.64}$$

Summing over all mass-compensated voids out to the source we get

$$\sigma_\kappa^2 = \Omega_M \sum_j \left[8 \sum_\alpha \frac{\eta_{\alpha,i} G M_{h,\alpha} \Psi_2(C_{h,\alpha})}{R_{h,\alpha}^2} + \frac{f_j \Omega_M H_0^2 R_i}{2 a_j^2} \right] \times \frac{H_0^2 Y_j f_j y_j^2 (y_S - y_j)^2}{y_S^2} \,. \tag{4.65}$$

Equation (4.65) shows that the overall variance depends on halo properties primarily via the typical value of $GM_{h,\alpha}/R_{h,\alpha}^2$, the gravitational acceleration characteristic of the outer regions of the halo. When this is large compared with the mean gravitational acceleration of the void as a whole, $f_j \Omega_M H_0^2 R_i / a_j^2$, the halos dominate the dispersion. There is also a hefty numerical factor $8\Psi_2(C_{h,\alpha}) \sim 50$ favoring the contribution from halos.

If $\eta_{\alpha,i} = \eta_\alpha$ is actually independent of i then we can factor out the sum over α in the first term of Eq. (4.65): define a dimensionless parameter

$$\begin{aligned} \overline{g}_h &\equiv \frac{16}{H_0} \sum_\alpha \frac{\eta_\alpha G M_{h,\alpha} \Psi_2(C_{h,\alpha})}{R_{h,\alpha}^2} \\ &= \frac{0.175 \langle M_{h,\alpha} \Psi_2(C_{h,\alpha}) / R_{h,\alpha}^2 \rangle}{h \times 10^{12} M_\odot / (300\,\mathrm{kpc})^2 \times 6.84.} \end{aligned} \tag{4.66}$$

We rewrite Eq. (4.65) as

$$\sigma_\kappa^2 = \frac{\Omega_M}{2} \overline{g}_h \sum_j \frac{(H_0 Y_j f_j) H_0^2 y_j^2 (y_S - y_j)^2}{y_S^2} + \frac{\Omega_M^2}{2} \sum_j \frac{(H_0 Y_j f_j)^2 H_0^2 y_j^2 (y_S - y_j)^2}{a_j^2 y_S^2}. \tag{4.67}$$

The first term in Eq.(4.67) is $\sim \overline{g}_h$ and the second is $\sim \Omega_M H_0 \langle Y_j \rangle \approx 3.5 \times 10^{-3} h \langle Y_j \rangle / 35\,\mathrm{Mpc}$. Eq. (4.66) suggests that halos dominate.

Now all of the parameters in Eq. (4.67) can be varied over distributions. To keep things as simple as possible, let us assume that f_j is simply a function of redshift; that is, neglect the possible dependence of f on the size of mass compensated voids. As a further simplification, we turn the sums into integrals. If we had a single void radius R the sums would turn into integrals by noting that there are $dy/2R$ voids per range dy; for a distribution of void sizes we can use this substitution with $R_i \to \langle R \rangle$ in the second sum. If we also define $\xi = H_0 y$ then with these simplifications

$$\sigma_\kappa^2(\xi_S) = \frac{\Omega_M}{4}\overline{g}_h \int_0^{\xi_S} \frac{d\xi\, f(\xi)\xi^2(\xi_S - \xi)^2}{\xi_S^2} + \frac{\Omega_M^2}{4} H_0 \langle R \rangle \int_0^{\xi_S} \frac{d\xi\, f^2(\xi)\xi^2(\xi_S - \xi)^2}{a^2(\xi)\xi_S^2} \tag{4.68}$$

The relationship between the variance of κ and the variance of magnifications σ_m, for small deviations, is approximated by

$$\sigma_m^2 = \left(\frac{5}{\log(10)}\right)^2 \sigma_\kappa^2. \tag{4.69}$$

CHAPTER 5

CONCLUSION

Ours is an exciting time for experiments in cosmology. A number of present and future surveys will play a major part in pinning down characteristics of the two major mysteries in cosmology - dark energy and dark matter.

Using optical data, radio data, weak gravitational lensing effects and the CMB power spectrum, we have been able to indirectly detect the presence of dark matter and we have been able to infer their distribution in the Universe. We now know the amount of dark matter is roughly 10 times the amount of baryonic matter in galaxies and it is distributed in halos around them. We also know that all the matter in the Universe is distributed in large scale voids which contain most of this matter in galaxy halos and dust on their edges while their interior is sparsely populated. Furthermore, particle experiments like the Large Hadron Collider are working on the direct detection of dark matter. This will further reveal its properties.

The second cosmological puzzle is the presence of the antigravitating dark energy which is accelerating the rate of expansion of the Universe. Compared to dark matter, we know relatively little about dark energy. However, future surveys which use Type 1a supernovae as standard candles to measure distance accuratley will be able to measure cosmological parameters to less than 1 % accuracy. This will be useful in determining the amount of dark energy more precisely and perhaps how it evolves with time.

The light coming from standard candles are subject to systematic uncertainties due to gravitational lensing from distribution of matter. To study this, our

work assumes two simplified analytical models for matter distributions in voids and galaxy halos, the SRN and SRR models. This allows for rapid computation of the full probability distribution of magnifications which is useful in studying these uncertainties so that they can be accounted for in inferring measured cosmological parameters.

BIBLIOGRAPHY

[1] M33 Image: NOAO, AURA, NSF, T. A. Rector.

[2] Credit: X-ray: NASA/CXC/CfA/M.Markevitch et al.

[3] Credit: NASA/WMAP Science Team

[4] Credit: NASA/WMAP Science Team

[5] S. Perlmutter, Physics Today; Vol. **56** Issue 4, 53 (2003)

[6] Xiang-Ping Wu, T. Chiueh, Li-Zhi Fang, Yan-Jie Xue, arXiv:astro-ph/9808179v1

[7] Credit: ESA/Hubble NASA

[8] W. Hu, http://background.uchicago.edu/ whu/intermediate/driving.html

[9] D. Baumann, A. Nicolis, L. Senatore, M. Zaldarriaga, arXiv:1004.2488v1 [astro-ph.CO]

[10] S. R. Green, R. M. Wald, Phys. Rev. D **83**, 084020 (2011).

[11] E. J. Copeland, M. Sami and S. Tsujikawa, Int. J. Mod. Phys. D **15**, 1753-1936 (2006).

[12] B. Ratra and P.J.E. Peebles, Phys. Rev. D **37**, 3406 (1988).

[13] S. Nojiri and S. D. Odintsov, arXiv:hep-th/0601213v3.

[14] S. Capozziello, V. F. Cardone and A. Troisi, Phys. Rev. D **71**, 043503 (2005).

[15] S. Nojiri and S. D. Odintsov, Phys Rev. D **74**, 086009 (2006).

[16] S. Nojiri and S. D. Odintsov, arXiv:hep-th/0610164v1.

[17] R. P. Woodard, arXiv:astro-ph/0601672v2.

[18] G. R. Dvali, G. Gabadadze and M. Porrati, Phys. Lett. B **485**, 208-214 (2000).

[19] K. Nozari, JCAP **09**, 003 (2007).

[20] R. Gregory, N. Kaloper, R. C. Myers and A. Padilla, arXiv: 0707.2666 [hep-th].

[21] A. Cardoso, arXiv:0805.2596 [astro-ph].

[22] Z. Zhu and M. Sereno, arXiv:0804.2917v1 [astro-ph].

[23] S. Yin, B. Wang, E. Abdalla and C. Lin, Phys. Rev. D **76** ,124026 (2007).

[24] A. Lue, Phys. Rept. **423**, 1-48 (2006).

[25] M. Kamionkowski, arXiv:0706.2986 [astro-ph].

[26] E. W. Kolb, S. Matarrese, A. Notari and A. Riotto, Phys. Rev. D **71**, 023524 (2005).

[27] E. W. Kolb, S. Matarrese, A. Notari and A. Riotto, arXiv:hep-th/0503117v1.

[28] E. W. Kolb, S. Matarrese and A. Riotto, New J. Phys. **8**, 322 (2006).

[29] S. Rasanen, JCAP **0611**, 003 (2006).

[30] Marie-Noëlle Célérier, New Advances in Physics **1**, 29 (2007).

[31] D. L. Wiltshire, arXiv: 0712.3984v1 [astro-ph].

[32] T. Buchert, arXiv: 0707.2153v3 [gr-qc].

[33] S. Rasanen, JCAP **0402** 003 (2004).

[34] E. Barausse, S. Matarrese and A. Riotto, Phys. Rev. D **71** 063537 (2005).

[35] T. Buchert, Gen. Rel. Grav. **32**, 105 (2000).

[36] T. Buchert, Gen. Rel. Grav. **9**, 306-321 (2000).

[37] T. Buchert, Gen Rel. Grav. **33**, 1381 (2001).

[38] T. Buchert, Class. Quant. Grav. **22**, L113 (2005).

[39] T. Buchert and J. Ehlers, Astron. Astrophys. **320**, 1 (1997).

[40] Marie-Noëlle Célérier, arXiv:astro-ph/0612222v2.

[41] E. E. Flanagan, Phys. Rev. D **71**, 103521 (2005).

[42] C. M. Hirata and U. Seljak, Phys. Rev. D **72**, 083501 (2005).

[43] G. Geshnizjani, D. H. J. Chung and N. Afshordi, Phys. Rev. D **72**, 023517 (2005).

[44] A. Ishibashi and R. M. Wald, Class. Quant. Grav. **23**, 235-250 (2006).

[45] H. Alnes, M. Amarzguioui and O. Gron, JCAP **0701**, 007 (2007).

[46] H. Alnes, M. Amarzguioui and O. Gron. Phys. Rev. D **73**, 083519 (2006).

[47] T. Kai, H. Kozaki, K. Nakao, Y. Nambu and C. Yoo, Prog. Theor. Phys. **117**, 229-240 (2007).

[48] V. Marra, E. W. Kolb and S. Matarrese, Phys. Rev. D **77**, 023003 (2008).

[49] B. Losic and W. B. Unruh, Phys. Rev. D **72**, 123510 (2005) and references within.

[50] R. H. Brandenberger, K. Dasgupta and A. Davis, arXiv:0801.3674v3 [hep-th].

[51] G. Marozzi, arXiv:gr-qc/0612148v3.

[52] M. S. Sloth, Nucl. Phys. B **748**, 149-169 (2006).

[53] D. Seery, JCAP **11**, 025 (2007).

[54] V. Mukhanov, L. R. W. Abramo, R. H. Brandenberger, Phys. Rev. Lett. **78**, 1624-1627 (1997).

[55] L. R. Abramo, R. H. Brandenberger, V. M. Mukhanov, Phys. Rev. D **56**, 3248-3257 (1997).

[56] W. Unruh, arXiv:astro-ph/9802323.

[57] G. Geshnizjani, R. H. Brandenberger, Phys. Rev. D **66**, 123507 (2002).

[58] G. Geshnizjani, R. H. Brandenberger, JCAP **0504**, 006 (2005).

[59] R. H. Brandenberger, arXiv:hep-th/0210165.

[60] P. Martineau, R. H. Brandenberger, arXiv:astro-ph/0510523.

[61] E. Barausse, S. Matarrese and A. Riotto, Phys. Rev. D **71**, 063537 (2005).

[62] B. S. DeWitt and R. W. Brehme, Ann. Phys. (N.Y.) **9**, 220 (1960). For a recent review see E. Poisson, arXiv:gr-qc/0306052.

[63] J. Behrend, I. A. Brown and G. Robbers, JCAP **01**, 013 (2008) and references within.

[64] J. Wambsganss, R. Cen, G. Xu, and J. P. Ostriker, Astron. J. Lett. **475**, L81+ (1997).

[65] D. E. Holz and R. M. Wald, Phys. Rev. D **58**, 063501 (1998).

[66] P. Valageas, Astron. Astrophys. **354**, 767 (2000).

[67] D.E. Holz and E. V. Linder, Ap.J. **631** 678 (2005).

[68] D. Munshi et al., Phys. Rep. **462**, 67 (2008).

[69] D. Sarkar, A. Amblard, D. E. Holz, A. Cooray, Ap. J. **678**, 1 (2008).

[70] D. E. Holz, S. A. Hughes. ApJ **629**, 15 (2005).

[71] G. Ghirlanda et al. New J Phys **8**, 123 (2006).

[72] L. Amendola et al., Phys. Rev. Lett. **105**, 121302 (2010).

[73] C. M. Hirata, D. E. Holz and C. Cutler, Phys. Rev. D **124046** (2010); C. Shang, Z. Haiman, Mon. Not. R. Astron. Soc. **411**, 9 (2011).

[74] A. Cooray, D. E. Holz, D. Huterer, Ap. J. **637**, L77 (2006); E. Linder, JCAP **0803**, 019 (2008); J. Jonsson et al., A.&A. **487**, 467 (2008); A.R. Zentner, S. Bhattacharya, Astrophys. J. **693**, 1543 (2009).

[75] J. Jonsson, T. Dahlen, A. Goobar, E. Mortsell, A. Reiss, J. Cosmo. Astropart. Phys. **6**, 002 (2007).

[76] M. Bartelmann, P. Schneider. Phys Rept **340**, 291-472 (2001).

[77] Y. Wang, D. E. Holz, D. Munshi. Astrophys J **572**, L15-L18 (2002).

[78] V. Springel, S. D. M. White, A. Jenkins, C. S. Frenk, N. Yoshida, L. Gao, J. Navarro, R. Thacker, D. Croton, J. Helly, J. A. Peacock, S. Cole, P. Thomas, H. Couchman, A. Evrard, J. Colberg, F. Pearce. Nature **435**, 629-636 (2005).

[79] E. Lawrence et al., Ap. J. **713**, 1322 (2010).

[80] B. Li et al., arXiv:1012.1625 (astro-ph).

[81] K. Kainulainen and V. Marra, Phys. Rev. D **80**, 123020 (2009).

[82] K. Kainulainen, V. Marra. Phys Rev D **83**, 023009 (2011).

[83] R. A. Vanderveld, E. E. Flanagan, I. Wasserman. Phys Rev D **78**, 083511 (2008).

[84] N. Sugiura, K. Nakao, D. Ida, N. Sakai, and H. Ishihara, Prog. Theor. Phys. **103**, 73 (2000).

[85] T. Kai, H. Kozaki, K. Nakao, Y. Nambu, and C.-M. Yoo, Prog. Theor. Phys. **117**, 229 (2007).

[86] N. Brouzakis, N. Tetradis, and E. Tzavara, JCAP **0702**, 013 (2007).

[87] B. Jain and U. Seljak, Ap.J. **484**, 560 (1997).

[88] B. Jain et al., Ap. J. **530**, 547 (2000).

[89] T. Hamana et al., Ap. J.**529**, 56 (2000).

[90] T. Hamana et al., Mon. Not. R. Astron. Soc. **330**, 365 (2002).

[91] T. Clifton, J. Zuntz. Mon. Not. R. Astron. Soc. **400**, 2185 (2009).

[92] N. Brouzakis, N. Tetradis, E. Tzavara, JCAP **0804**, 008 (2008).

[93] S. J. Szybka. arXiv:1012.5239v1 [astro-ph.CO].

[94] T. Biswas, A. Notari, JCAP **0806**, 021 (2008).

[95] V.Marra, E.W. Kolb, S.Matarrese, A. Riotto. Phys Rev D **76**, 123004 (2007).

[96] V. Marra, E. W. Kolb, S. Matarrese. Phys Rev D **77**, 023003 (2008).

[97] V. Marra. arXiv:0803.3152v3 [astro-ph] (2008).

[98] F. Hoyle, M. S. Vogeley. ApJ **607** 751 (2004).

[99] H. Mathis, S. D. M. White. Monthly Notices of the Royal Astronomical Society **337**, Issue 4, 1193–1206 (2002).

[100] S. Gottlber, E. L. Łokas, A. Klypin, Y. Hoffman. Monthly Notices of the Royal Astronomical Society **344**, Issue 3,715–724 (2003).

[101] M. Plionis, S. Basilakos. Monthly Notices of the Royal Astronomical Society **330**, Issue 2, 399–404 (2002).

[102] D. C. Pan, M. S. Vogeley, F. Hoyle, Y.-Y Choi, C. Park. arXiv:1103.4156v2 [astro-ph.CO]

[103] C. Adami, A. Mazure, M. Pierre, P.G. Sprimont, C. Libbrecht, F. Pacaud, N. Clerc, T. Sadibekova, J. Surdej, B. Altieri, P.A. Duc, G. Galaz, A. Gueguen, L. Guennou, G. Hertling, O. Ilbert, J.P. LeFvre, H. Quintana, I. Valtchanov, J.P. Willis, M. Akiyama, H. Aussel, L. Chiappetti, A. Detal, B. Garilli, V. LeBrun, O. LeFvre, D. Maccagni, J.B. Melin, T.J. Ponman, D. Ricci, L. Tresse. arXiv:1010.6195v1 [astro-ph.CO]

[104] K. Kreckel, E. Platen, M. A. Aragn-Calvo, J. H. van Gorkom, R. van de Weygaert, J. M. van der Hulst, K. Kovač, C.-W. Yip, P. J. E. Peebles. arXiv:1008.4616v1 [astro-ph.CO]

[105] Margaret J. Gellar, J. P. Huchra. Science **246**, 4932, 897 - 903, (1989).

[106] S. D. M. White, C. S. Frenk, M. Davis, G. Efstathiou. ApJ **313**, 505 - 516 (1987).

[107] A. Cooray, D. Huterer, D. E. Holz, Phys. Rev. Lett. **96**, 1301 (2006).

[108] P. Valageas. A & A **356**, 771 (2000).

[109] C. Bonvin, R. Durrer, M. A. Gasparini, Phys. Rev. D **73**, 023523 (2006).

[110] E. E. Flanagan, E. Rosenthal, I. Wasserman, Phys. Rev. D **79**, 044032 (2009).

[111] M. Visser, Phys. Rev. D **47**, 2395 (1993).

[112] L. Hui, P. B. Greene. Phys Rev **D**73, 123526 (2006).

[113] A. de Lavallaz, M. Fairbairn, arXiv:1106.1611v1 [astro-ph.CO]

[114] V. Kostov, arXiv:0910.2611.

[115] E. E. Flanagan, N. Kumar, I. Wasserman and R. A. Vanderveld. Phys. Rev. D **85**, 023510 (2012).

[116] J. Wambsganss, R. Cen, G. Xu, and J. P. Ostriker, Astron. J. Lett. **475**, L81+ (1997).

[117] D. E. Holz and R. M. Wald, Phys. Rev. D **58**, 063501 (1998).

[118] P. Valageas, Astron. Astrophys. **354**, 767 (2000).

[119] D.E. Holz and E. V. Linder, Ap.J. **631**, 678 (2005).

[120] D. Munshi et al., Phys. Rep. **462**, 67 (2008).

[121] R. A. Vanderveld, E. E. Flanagan, I. Wasserman. Phys Rev D **78**, 083511 (2008).

[122] N. Sugiura, K. Nakao, D. Ida, N. Sakai, and H. Ishihara, Prog. Theor. Phys. **103**, 73 (2000).

[123] T. Kai, H. Kozaki, K. Nakao, Y. Nambu, and C.-M. Yoo, Prog. Theor. Phys. **117**, 229 (2007).

[124] N. Brouzakis, N. Tetradis, and E. Tzavara, JCAP **0702**, 013 (2007).

[125] K. Kainulainen, V. Marra. Phys. Rev. D **80**, 123020 (2009).

[126] K. Kainulainen, V. Marra. Phys. Rev. D **83**, 023009 (2011).

[127] J. F . Navarro, C. S. Frenk, S. D. M. White. Astrophys. J. **462**, 563-575 (1996).

[128] A. Nishizawa, A. Taruya, S. Saito. Phys. Rev. D **83**, 084045 (2011).

[129] K. Bolejko. JCAP **02**, 025 (2011).

[130] S. Hilbert, J. Hartlap, P. Schneider. arXiv:1105.3980v2 [astro-ph.CO].

[131] R. Takahashi, M. Oguri, M. Sato, T. Hamana. arXiv:1106.3823v2 [astro-ph.CO].

[132] P. Valageas, M. Sato, T. Nishimichi. arXiv:1112.1495v1 [astro-ph.CO].

[133] T. Clifton, J. Zuntz. Mon. Not. R. Astron. Soc. **400**, 2185 (2009).

[134] N. Brouzakis, N. Tetradis, E. Tzavara, JCAP **0804**, 008 (2008).

[135] S. J. Szybka. arXiv:1012.5239v1 [astro-ph.CO].

[136] T. Biswas, A. Notari, JCAP **0806**, 021 (2008).

[137] K. Kreckel, E. Platen, M. A. Aragn-Calvo, J. H. van Gorkom, R. van de Weygaert, J. M. van der Hulst, K. Kovac, C.-W. Yip, P. J. E. Peebles. arXiv:1008.4616v1 [astro-ph.CO]